Fusion Engineering and Design 175 (2022) 113010

Contents lists available at ScienceDirect

Fusion Engineering and Design

journal homepage: www.elsevier.com/locate/fusengdes

Divertor of the European DEMO: Engineering and technologies for power exhaust

J.H. You [a,*], G. Mazzone [b], E. Visca [b], H. Greuner [a], M. Fursdon [c], Y. Addab [d], C. Bachmann [e], T. Barrett [c], U. Bonavolontà [f], B. Böswirth [a], F.M. Castrovinci [g], C. Carelli [c], D. Coccorese [f], R. Coppola [h], F. Crescenzi [b], G. Di Gironimo [f], P.A. Di Maio [g], G. Di Mambro [i], F. Domptail [c], D. Dongiovanni [b], G. Dose [j], D. Flammini [b], L. Forest [k], P. Frosi [b], F. Gallay [d], B.E. Ghidersa [l], C. Harrington [c], K. Hunger [a], V. Imbriani [f], M. Li [a], A. Lukenskas [c], A. Maffucci [i], N. Mantel [c], D. Marzullo [m], T. Minniti [c], A.V. Müller [a], S. Noce [j], M.T. Porfiri [b], A. Quartararo [g], M. Richou [d], S. Roccella [b], D. Terentyev [n], A. Tincani [o], E. Vallone [g], S. Ventre [i], R. Villari [b], F. Villone [p], C. Vorpahl [e], K. Zhang [a]

[a] Max Planck Institute for Plasma Physics, Boltzmannstr. 2, Garching 85748, Germany
[b] Department of Fusion and Technology for Nuclear Safety, ENEA Frascati, via E. Fermi 45, Frascati 00044, Italy
[c] CCFE, Culham Science Centre, Abingdon OX14 3DB, United Kingdom
[d] CEA, IRFM, Saint Paul Lez Durance F-13108, France
[e] Department of PPPT, EUROfusion PMU, Boltzmann Str. 2, Garching 85748, Germany
[f] Department of Industrial Engineering, CREATE/University of Naples, Piazzale Tecchio 80, Napoli 80125, Italy
[g] Department of Engineering, University of Palermo, Viale delle Scienze, Building 6, Palermo 90128, Italy
[h] Department of Fusion and Nuclear Safety, ENEA Casaccia, Via Anguillarese 301, Roma 00123, Italy
[i] CREATE/University of Cassino and Southern Lazio, Via G. Di Biasio 43, Cassino 03043, Italy
[j] Department of Industrial Engineering, University of Rom Tor Vergata, Via del Politecnico 1, Rom 00133, Italy
[k] CEA, DEN-SEMT, University of Paris-Saclay, Gif sur Yvette F-91191, France
[l] KIT, IAM, Hermann-von-Helmholtz-Platz 1, Eggenstein-Leopoldshafen 76344, Germany
[m] Department of Engineering, University of Trieste, Via Alfonso Valerio, 6/1, Trieste 34127, Italy
[n] SCK CEN, Institute for Nuclear Materials Science, Mol, 2400, Belgium
[o] ENEA Brasimone, Località Brasimone, Camugnano Bologna 40032, Italy
[p] Department of Electrical Engineering, University of Naples, Via Claudio 21, Naples 80125, Italy

ARTICLE INFO

Keywords:
DEMO
Fusion reactor
Divertor
Plasma-facing component
High-heat-flux
Power exhaust

ABSTRACT

In a power plant scale fusion reactor, a huge amount of thermal power produced by the fusion reaction and external heating must be exhausted through the narrow area of the divertor targets. The targets must withstand the intense bombardment of the diverted particles where high heat fluxes are generated and erosion takes place on the surface. A considerable amount of volumetric nuclear heating power must also be exhausted. To cope with such an unprecedented power exhaust challenge, a highly efficient cooling capacity is required. Furthermore, the divertor must fulfill other critical functions such as nuclear shielding and channeling (and compression) of exhaust gas for pumping. Assuring the structural integrity of the neutron-irradiated (thus embrittled) components is a crucial prerequisite for a reliable operation over the lifetime. Safety, maintainability, availability, waste and costs are another points of consideration.

In late 2020, the Pre-Conceptual Design activities to develop the divertor of the European demonstration fusion reactor were officially concluded. On this occasion, the baseline design and the key technology options were identified and verified by the project team (EUROfusion Work Package Divertor) based on seven years of R&D efforts and endorsed by Gate Review Panel.

In this paper, an overview of the load specifications, brief descriptions of the design and the highlights of the technology R&D work are presented together with the further work still needed.

* Corresponding author.
E-mail address: you@ipp.mpg.de (J.H. You).

https://doi.org/10.1016/j.fusengdes.2022.113010
Received 13 August 2021; Received in revised form 3 December 2021; Accepted 5 January 2022
Available online 13 January 2022

1. Introduction

In late 2020, the Pre-Concept Design (PCD) Phase of the European DEMO fusion reactor (that will be simply called DEMO in the rest of the paper) that were started in 2014 [1,2] were concluded. A dedicated work package (WPDIV) was installed to develop the divertor of the DEMO. The final design review and the gate review endorsed the baseline design and the key technology options. The aim of this paper is to present the outcome of the work conducted in the PCD Phase including the latest technology achievements. Further information on design options that were considered in the initial design phase can also be found in [3–6].

1.1. Functions, high-level requirements and configuration

The DEMO is based on a diverted magnetic configuration where plasma particles flowing in the scrape-off layer (SOL) are blocked by the divertor targets. The divertor is a key in-vessel component carrying out critical functions as follows [7–10]:

(1) To remove heat produced by particle bombardment, radiation and volumetric nuclear heating.
(2) To form gas streaming channels towards the pumping ports for exhausting helium 'ash' and unburnt deuterium-tritium (D-T) fuel.
(3) To shield the vacuum vessel (VV) and magnets against nuclear loads.
(4) To provide plasma-facing surface which is physically compatible with the plasma (low sputtering, low tritium retention, high melting point, etc.).

In the DEMO, the divertor shall be subjected to very harsh loading environment, but is supposed to operate reliably for the envisaged lifetime. Furthermore, there are several high-level requirements which should be considered as fundamental engineering constraints and design drivers, namely [11]:

(1) To minimize the nuclear waste from replaced divertor components (particularly, intermediate level[1]).
(2) To pursue reasonable manufacturing costs and maximal recycling potential.
(3) To minimize design complexity for reducing maintenance downtime.

Fig. 1 shows the CAD model of the DEMO (2020 version) illustrating the 3D architecture with the single null divertor configuration. The current baseline configuration adopted for the DEMO is the so-called 'single-null' divertor concept where the divertor is located at the bottom of the VV [1]. The SOL field lines intersect the targets.

The DEMO divertor currently consists of 48 separate cassette modules arrayed along the toroidal direction. The number of cassette modules was determined by the number of the toroidal field coils (and thus vessel sectors). In the DEMO baseline, 16 toroidal field coils are foreseen as the most optimal compromise between the intensity of magnetic field ripples and the spacing for the (breeding blanket) maintenance ports. Each cassette module shall be deployed or retracted via an associated lower port for installation and maintenance [13]. Each module comprises following components [14,15]:

(1) Two target plates on which the impinging SOL particles are stopped.
(2) Cassette body which holds the targets and other shielding components.
(3) Shielding components (shielding liner and reflector plates) which protects the VV and pipes.
(4) Pipework of the cooling circuits.

1.2. Particle exhaust and power exhaust

For a stable fusion operation, the concentration of the helium ash accumulating in the burning plasma must be controlled below the dilution threshold. This control is achieved by the diverted magnetic configuration (see Fig. 2). In this configuration, the plasma particles (fuel/ash mixture) drift outwards, enter into the SOL crossing the separatrix at the plasma edge and are guided along the SOL towards the divertor targets where they are eventually neutralized and pumped out together with impurities [16].

When impinging upon the target surface, the plasma particles transfer thermal power producing high heat fluxes. In this way, a substantial fraction of the fusion power (carried by alpha particles) and the auxiliary heating power (carried by the fuel plasma) is transported to the divertor targets via the SOL. This thermal power must be continuously exhausted at the targets by means of active cooling to enable a long-pulse operation. As the characteristic power decay length of the SOL is small, the thermal power density is concentrated on a narrow band (strike point) of the targets leading to a local peaking of heat flux density. The key plasma parameters of the DEMO related to power exhaust are summarized in Table 1 [17–19]. For comparison, the parameters of ITER are also given. The near-SOL (characteristic scrape-off decay length $\lambda_q \cong$ 1 mm) thermal power carried by the charged particles reaches 31MW at the SOL radiation fraction of 70%), which can produce exceedingly high heat fluxes (HHF) at the strike point on the targets (power density: $\geq$10MW/m^2). At a lower SOL radiation fraction, the particle power becomes accordingly higher (e.g. 69MW at 40%). This situation raises the critical issue of power handling, a serious physical and technological challenge commonly confronted in the designing of a large-scale (GW range) fusion reactor.

For mitigating the power density concentration to an acceptable level, two approaches are employed:

(1) Inclined targets at a shallow angle (2–3°) relative to the grazing magnetic field lines to expand the footprint of the magnetic field flux on the targets so that the wetted area is increased [7].
(2) Power dissipation by means of radiative cooling in the SOL and in the proximity of the targets using seeded inert gas (injected below the allowable concentration limit) so that a detached plasma state (characterized by cold plasma in the range 5–10 eV) can build up [20].

1.3. Operation and maintenance

While the targets are subjected to particle bombardment and HHF loads, the entire divertor is exposed to fast neutrons radiating from the plasma core. The intense neutron flux ($\sim 10^{16}$–10^{18}/m^2·s) generates strong volumetric nuclear heating via thermal moderation due to the elastic scattering by the coolant molecules and gamma ray emission due to nuclei excitation in the solid materials [21]. Fig. 3 shows the predicted distribution of nuclear heating power density plotted on the contour of the DEMO divertor cassette. In addition, X-rays due to Bremsstrahlung of electrons and the line emission of impurity atoms (near the separatrix X-point) produce radiation power [16,20]. The heat is removed by active cooling.

Currently, the baseline design is based on pressurized-water cooling operated at a relatively lower temperature range compared to a PWR ($\sim$280–320 °C). The baseline cooling scheme employs a separate dual cooling circuit system where each circuit is dedicated for either the targets or cassette body (CB). The cooling circuits are operated at

[1] The design rules of DEMO foresee no materials which can transmute to high level waste.

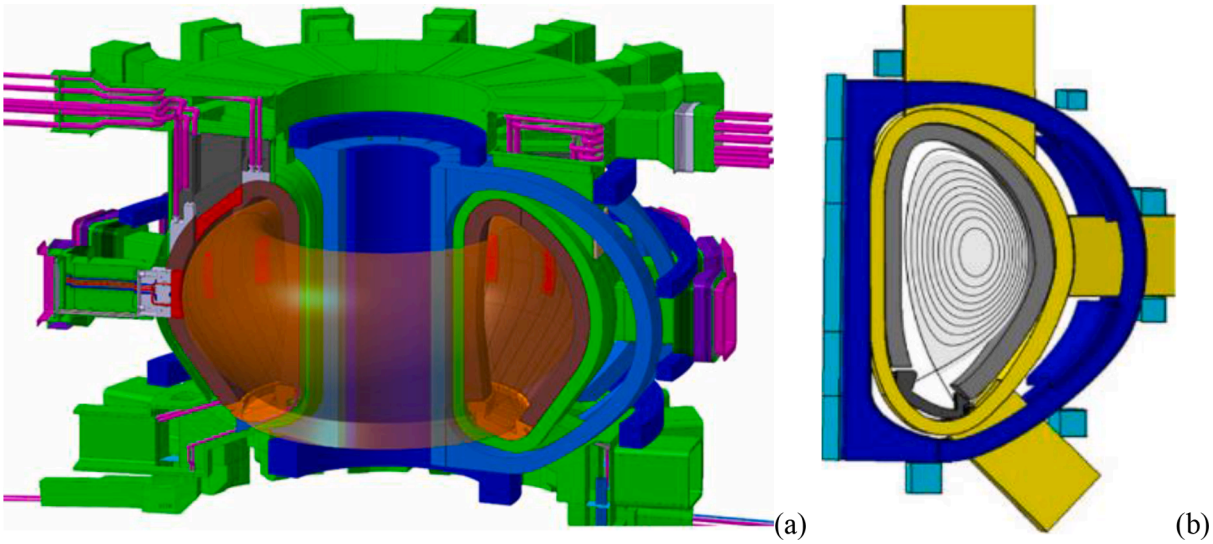

Fig. 1. CAD configuration model of the European DEMO showing the internal cut view (a) and the poloidal magnetic configuration adapted from [12] (b).

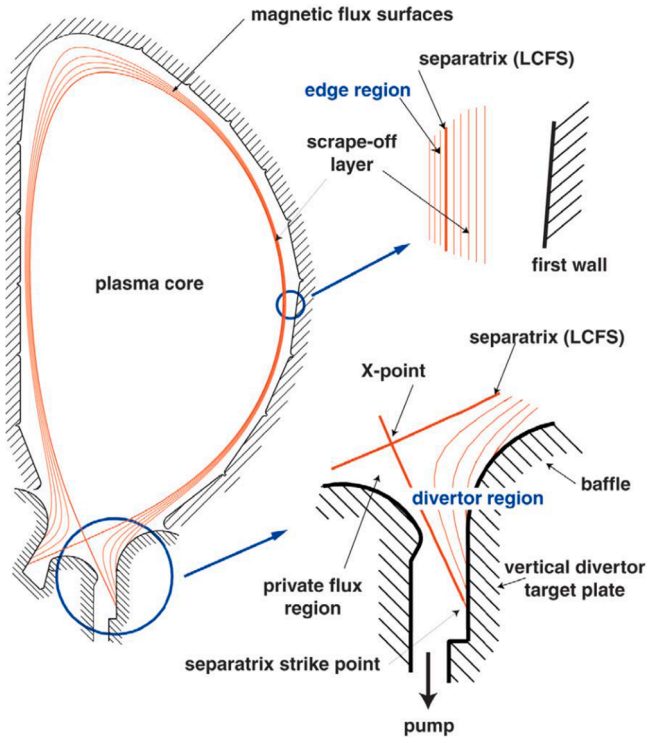

Fig. 2. Schematic illustration of the generic magnetic field profiles in the edge layer of a typical tokamak with the diverted magnetic configuration (poloidal cut section) [11]. (Courtesy from IoP/IAEA).

separate temperature and pressure levels. The rationale and details of this decoupled cooling scheme is elucidated later (chapter 4). The coolant feeding pipes and the outlet pipes are routed through the allocated lower port and connected to the primary heat transfer system (PHTS) of the plant where the exhaust heat can be used for preheating the fresh coolant [11].

A certain number of the lower ports will be reserved exclusively for pumping. A pump system (e.g. diffusion pump combined with a metal foil pump or multi-stage cryopump) is stationed in the rear casks connected to the lower port within the confinement barrier (see Fig. 4, readers are referred to [22] for details). As the space of the plasma core acts as a perfect sink for the neutral gas, a strong pumping capacity as well as high gas conductance are required to maintain a sufficient gas throughput rate. In this context, the gas streaming paths formed by the duct and the gaps in the cassette system play a decisive role in fostering gas exhaust and in hindering gas upstreaming and reflux [8]. Assuming eight pumping ports, the required pumping speed for D_2 is 100-130m^3/s per port (pumped by the combination of metal foil pumps and a linear diffusion pump), which is demanding. A few more pumping ports will be needed for recycling the unburnt fuel gas. On the contrary, for He, only 4m^3/s is sufficient per port (pumped by the 2nd diffusion pump) [22]. Remote maintenance of the divertor cassettes will probably be conducted via dedicated maintenance ports (~6) which are not occupied by stationed pumps to reduce maintenance downtime.

Table 1
Key plasma parameters of the European DEMO and ITER related to power exhaust [19].

Parameters	EU-DEMO	ITER
Pulse (s)	7200	400
R_p/a_p (m), A	9.0/2.9, 3.1	6.2/2.0, 3.1
q_{95}	3.5	3
β_N	2.6	1.8
f_{GW} (= n_e/n_{GW}) *GW (= ne/nGW)*	1.2	0.83
P_{fusion} (MW_{th})	2000	500
P_{el} (MW_e)	500	–
P_{aux} (MW)	50	73 (installed)
P_{heat} (= $P_\alpha + P_{aux}$) (MW)	457	173
Q	41	5/10
$c_{imp,\ core}$ (= n_{imp}/n_e)	0.039 (Xe) + Ar	N_2, Ne, Ar, ...
$P_{rad,\ core}$ (MW)	306	~50
$f_{rad,\ core}$ (= $P_{rad,\ core}/P_{heat}$)	0.67	~0.33
P_{sep} (MW)	154	~100
P_{sep}/R_p (MW/m)	17	~16
$P_{L\text{-}H\ th}$ (MW)	133MW	~84
$f_{L\text{-}H\ th}$ (= $P_{sep}/P_{L\text{-}H\ th}$)	1.2	~1.2

The plasma state in front of the divertor targets shall be monitored by *in-situ* diagnostic tools such as thermo-current measurement in order to detect a plasma reattachment event so that a detached state can be recovered by means of active controlling. To this end, full electrical insulation of the targets from the cassette body (except for a shunt) is necessary.

The sacrificial armor of the targets protects the water-cooled heat sink (pipes) from a direct contact with plasma. In normal and off-normal operation situations, the armor material is subjected to diverse surface erosion processes. The ratio of the front face armor thickness to the average erosion rate determines the erosion lifetime of the targets. Edge

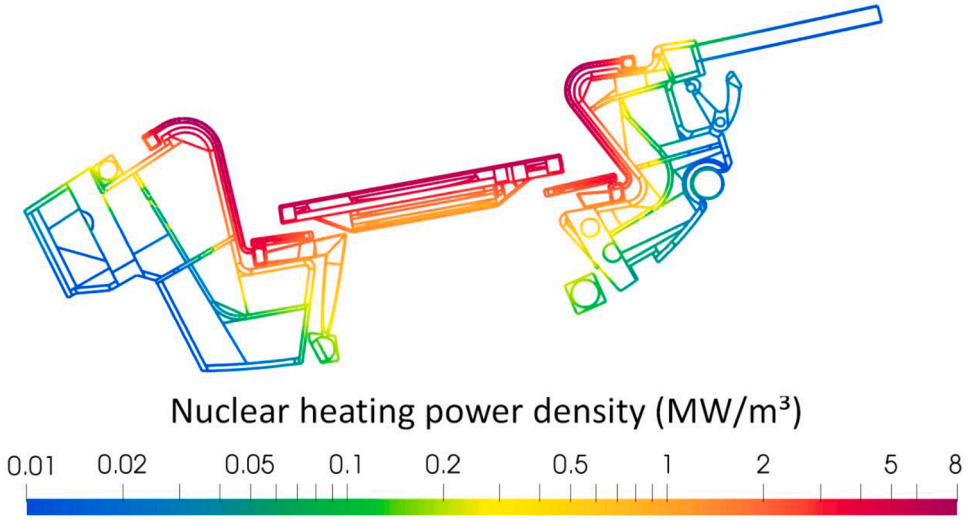

Fig. 3. Distribution of nuclear heating power density in the divertor cassette of the EU-DEMO.

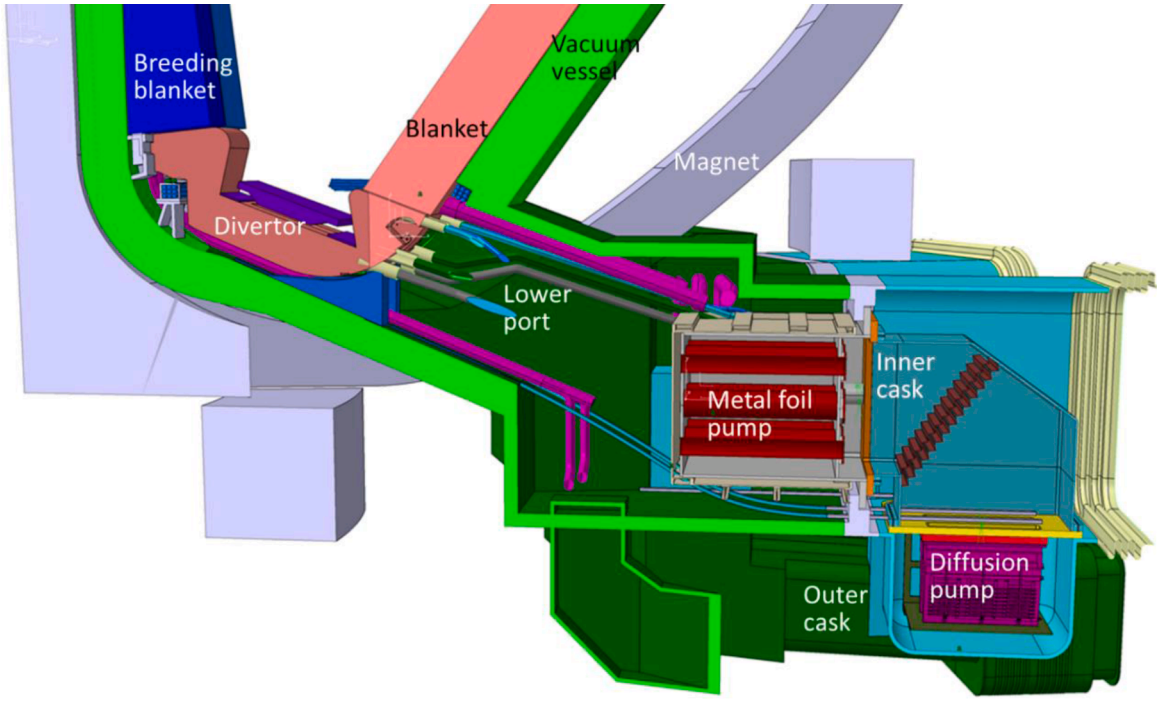

Fig. 4. Lower port region and the rear casks of the European DEMO design [23].

localized modes (ELMs) with the particle energy of a few keV will have a decisive impact on the erosion lifetime [8,20,24].

The lifetime of the structural materials (copper alloy, steel) is likely to be affected by neutron irradiation due to embrittlement and reduction of strength. The impact of irradiation on structural integrity depends on temperature and stress state during operation.

Once the end of design life has been reached (by erosion or irradiation), the divertor must be refurbished. The maintenance shall be performed by means of remote handling tools in a radioactive environment. The end effectors of a robot arm manipulator access the cassettes through the respective lower port. In case a cassette module needs to be replaced, the cassette is moved using the toroidal transport rail. The detailed remote installation sequence is explained in Section 3.8.

1.4. Alternative divertor configurations (ADCs)

Even though the current DEMO design is based on the single null divertor configuration as baseline, further selected ADCs are also under consideration for a possible down-selection at a later stage [25]. The down-selection will depend on the outcomes of the extensive physics as well as engineering studies. Fig. 5 shows four ADCs (as of 2018), namely, X divertor (XD), super X (SX) divertor, snowflake (SF) divertor and double null (DN) divertor (f.l.t.r.) [12]. These ADCs commonly feature widely expanded (and smeared) plasma footprints and longer outer connection lengths aiming at reduced heat flux peaking on the targets and thus more manageable power handling.

On the other hand, the ADCs can have a far-reaching impact on overall engineering design, in particular, with regard to vessel/port design, pumping, remote maintenance, T breeding ratio, magnets,

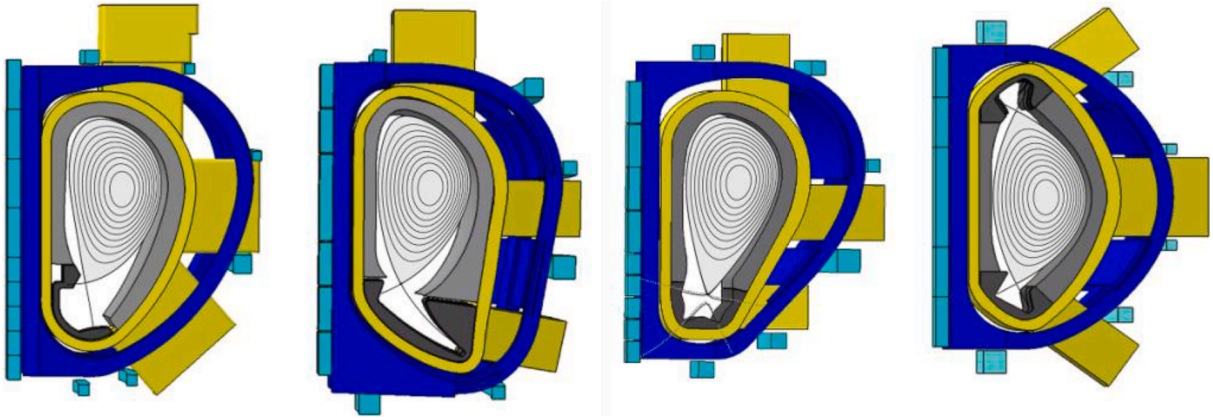

Fig. 5. Magnetic configurations of the alternative divertor concepts considered for the European DEMO (2018 version) [12]. (f.l.t.r.: X divertor, super X divertor, snowflake divertor, double null divertor). (Copyright 2019, Courtesy from IoP/IAEA).

diagnostics & control, and costs. The impact is mainly due to the extended dimensions and the complex geometry. Therefore, the trade-off between physical benefits and engineering difficulties needs to be thoroughly evaluated. Recently, a preliminary engineering study by Militello et al. was published where outstanding engineering issues of the individual ADCs are compared and discussed [26]. One of the common critical issues is the excessive magnetic forces exerting on the toroidal field magnets. The initial magnet design of all ADCs failed to pass structural failure criteria. Inter-coil stiffeners will be needed to ensure rigidity against out-of-plane deformation of the coils. Another critical issue is remote maintainability, which has not been verified yet for the ADCs. DN seems to need a drastic reconfiguration of maintenance concept (e.g. divided cassette, integration to the blanket segment) while SF, SX, XD still remain at an early stage of concept study owing to challenging remote handling maneuver. The control difficulty of strike point position and vertical stability under plasma displacement is deemed a serious issue for SF, SX, XD and even a potential show stopper for SF [12].

The preliminary assessment clearly showed that all ADCs are burdened with considerable engineering disadvantages revealing high criticality for SF, SX, XD. However, it seems presently premature to make any definitive judgement on the pros and cons.

1.5. Alternative target technology options

During the PCD phase, preliminary exploring studies were performed for a few alternative divertor target technologies other than the current baseline. The alternative technologies included liquid metal target (e.g. capillary porous armor system using a lithium bath) [27], helium-cooled target (tungsten monoblock design equipped with multi-jet injection dual pipes) [28] and water-cooled heat pipe target [29]. The R&D progress of these concepts is still at an early stage and thus they are regarded as long-term potential options (not necessarily to be pursued). Among these three alternative options, the helium-cooled target concept has reached a proof-of-principle stage where a local heat removal capacity up to 8–10MW/m^2 was demonstrated for a medium-scale mock-up [28].

2. Loads and requirements

In this Section, the plant-level loads and the high-level system requirements imposed on the DEMO divertor are described. Design strategy and engineering approaches are subordinate to these.

2.1. Extrinsic loads

In Table 2, the extrinsic loads specified as design values for the currently assumed operation scenarios are listed [30]. These load values can be regarded as working hypotheses at the present stage (as of 2020). The naming convention of the IDs is as follows:

- Load-1: Volumetric thermal load (nuclear);
- Load-2: Surface thermal load by particles;
- Load-3: Surface thermal load by radiation;

Table 2
Extrinsic loads specified for the European DEMO divertor (as of 2020) [30].

ID	Loads	Specifications
Load-1a	Volumetric thermal power Volumetric thermal power density	~139MW (by nuclear heating) ≤8MW/m^3
Load-1b	Baking temperature	~240 °C (uniform heating)
Load-2a	Surface thermal power on the targets	~45MW (by charged particles) ~108MW (by SOL radiation)
Load-2b	Peak heat flux density in normal operation (pulse length at flat top: 2 h, number of cycles: ≥ 6600 + overhead)	~10MW/m^2 (on the targets) ~1MW/m^2 (on the shielding liner) ~0.2MW/m^2 (on the reflector plates)
Load-2c	Peak heat flux density in slow transients (thermal equilibrium: ~10 s, frequency: tbd.)	~20MW/m^2 (on the targets)
Load-2d	Peak heat flux density in short transients (no thermal equilibrium: ≤1 s, frequency: tbd.)	≤70MW/m^2 (on the targets) with sweeping (e.g. 1 Hz, 0.2 m)
Load-2e	Energy deposition on targets upon fast transients (off-normal events, frequency: tbd.)	≤150 kJ/m^2
Load-2f	Energy deposition and peak heat flux density on targets upon major (centred) disruption	≤1GJ, 79-111GW/m^2 (without limiter) Thermal quench: 1-4ms
Load-2 g	Surface heat flux density due to neutral particles	~2 kW/m^2 (baffle region[1])
Load-3a	Surface thermal power due to core radiation	≤78MW
Load-3b	Surface heat flux density due to core radiation	~1MW/m^2
Load-4	Peak electromagnetic impact load (downward disruption)	~1.3MN (vertical) excl. dynamic amplification (tbd.)
Load-5	Particle flux density in front of the targets	~10^{24}/m^2•s (≤10 eV)
Load-6	Neutron flux density in the surface layer	~1.7 × 10^{18}·n/m^2·s
Load-7	Coolant pressure at the circuit inlet	~5 MPa (targets) ~3.5 MPa (cassette body)
Load-8	Coolant water chemistry (radiolysis control)	purified water with reducing agent (H)

Table 3
High-level system requirements imposed on the European DEMO divertor.

ID	Descriptions
SR-1	The divertor shall reliably perform the key functions over the entire lifetime withstanding the extrinsic loads and the induced effects of the loads (e.g. secondary stresses, armor surface erosion, material damage, corrosion, etc.).
SR-2	The specified minimum lifetime (interval between replacements) is 1.5fpy[1]. *Rationale*: Operational lifetime is specified considering a reasonable balance between the power plant availability and structural/functional reliability. This requirement is of tentative nature since materials data from relevant irradiation tests are very limited. The initial lifetime shall be redefined again once materials data and design criteria from dedicated irradiation tests are available, also taking into account the evolving maintenance scheme.
SR-3	Tungsten shall be used as plasma-facing armor of PFCs. EUROFER97 steel shall be used as structural material for the cassette body and fixation units. *Rationale*: The material options should comply with the high-level requirements such as physical compatibility with fusion plasma (for PFCs) and reduced activation to assure recyclability (for major structures).
SR-4	The design concept should be able to be realized by means of feasible technology options (≥TRL[2] 4 at the 3rd Gate review in 2027) within an acceptable cost frame and the DEMO project timeline (EDA[3] phase from 2028 on). Technology maturity shall be evaluated at the 2nd Gate review in terms of the technology readiness level (TRL).
SR-5	The divertor (incl. pipework) shall be compatible with the interfacing plant sub-systems.
SR-6	The divertor must protect adjacent Vacuum Vessel (VV) (AISI 316LN-IG) and magnets from neutron radiation keeping nuclear loads below the specified limits. - max. allowable irradiation damage dose limit in VV: 2.75dpa[4]/6fpy [31] - max. allowable nuclear heating limit in superconducting magnets: 50 W/m^3

[1] fpy: full-power-year (of operation).
[2] TRL: Technology Readiness Level.
[3] EDA: Engineering Design Activity.
[4] displacement per atom.

– Load-4: Dynamic impact load (electromagnetic);
– Load-5: Surface particle flux;
– Load-6: Volumetric neutron flux;
– Load-7: Static primary load (pressure);
– Load-7: Chemical load (radiolysis).

(1) The upper edge region of the Targets adjacent to the bottom edge of the breeding blanket.

2.2. Design requirements

In Table 3, the high-level system requirements are described with the underlying rationales.

3. Baseline design concept

In this Section, the baseline design (as of 2020) of the DEMO divertor is briefly described. In mid-2020, the final version was validated by the Design Review Panel.

3.1. Design approach and constraints

Functional performance (cooling, shielding, pumping), structural integrity and longevity are three key design aspects. Issues related to (industrial) manufacturability, costs, waste hazard and safety are further design concerns. The envisaged lifetime (specified for the baseline design) is 1.5 full power year (fpy). The refurbishment should take place *ex-situ* in a hot cell outside the tokamak building. It was assumed that the DEMO divertor would not need to be classified as a SIC (Safety Importance Classification) component because the divertor was not supposed to have the containment function [32]. As a non-SIC component, divertor design can be exempted from those licensing regulations that are mandatory for a nuclear pressure equipment (e.g. ESPN order). It is accepted to produce a limited amount of low/medium level wastes which have an acceptable decay time (reaching the hands-on level after a few centuries). Based on these considerations, the following approaches were adopted:

(1) Pursue maximum possible HHF technology limit to achieve a sufficient operational margin.
(2) Where reasonably applicable, use mature (and commercially available) materials or technologies.
(3) Where required, develop and apply advanced materials or technologies.

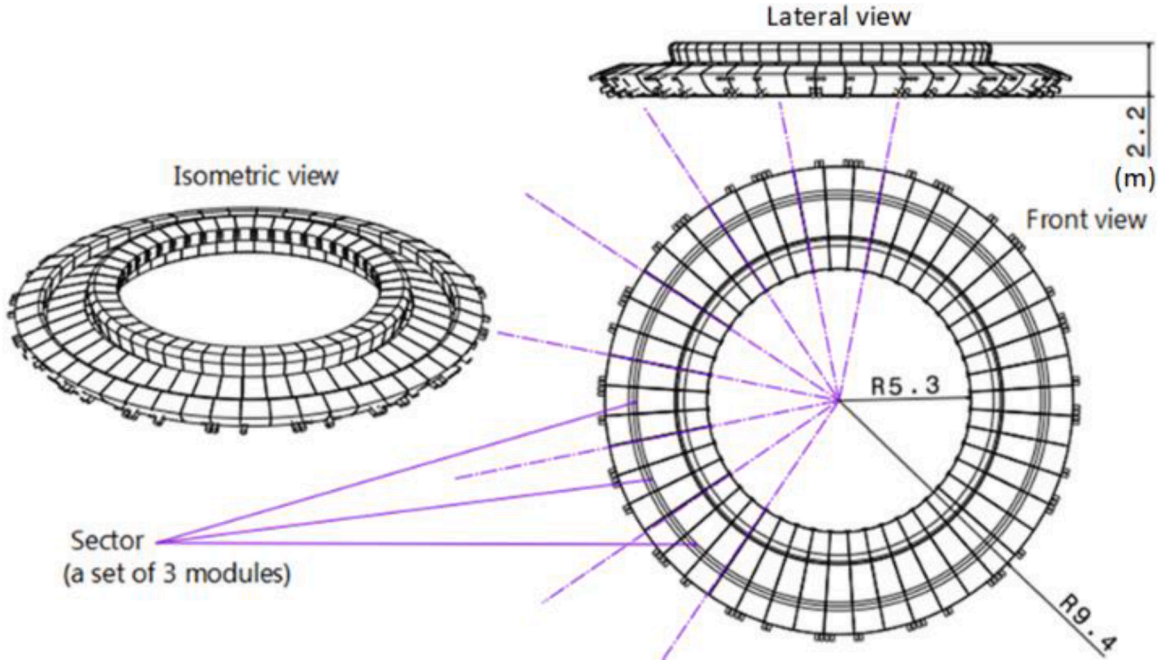

Fig. 6. Global CAD configuration model of the entire DEMO divertor (seen from 3 viewing angles).

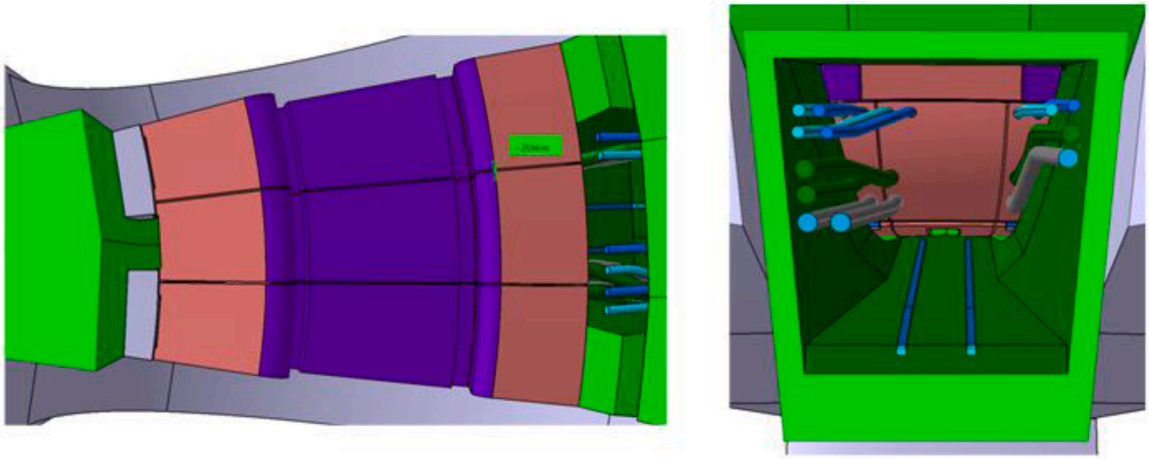

Fig. 7. A typical sector consisting of three cassette modules (left: front view, right: view through the port).

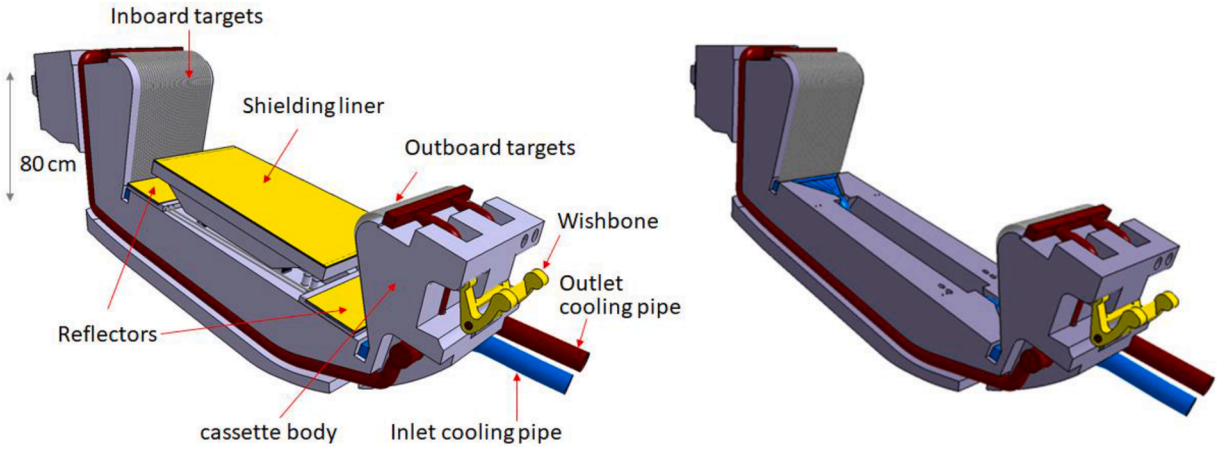

Fig. 8. A typical divertor cassette module (left: fully equipped, right: cassette body without shielding liner and reflector plates).

(4) Take evolutionary R&D paths to exploit the state-of-the-art ITER technology.
(5) Assure the design and technology against all expected operational anomalies.
(6) Apply both design-by-analysis and design-by-experiment (still non-nuclear) approaches.
(7) Find a pragmatic compromise between competing requirements (e.g. critical heat flux margin vs. low-temperature embrittlement).

It is worthy of mention that the HHF technology (namely, targets) of the DEMO was mostly inherited from the ITER technology (up to a slight difference in dimension) whereas the other parts of the cassette are based on a unique design. The major differences from the ITER divertor are explained below in the respective section.

3.2. Overall architecture

Fig. 6 shows the global CAD configuration model of the entire divertor (seen from three viewing angles). The divertor consists of 48 cassette modules arrayed symmetrically along the toroidal orientation. The divertor is divided into 16 sectors. Each sector comprises equally a set of 3 modules (1 central cassette and 2 side cassettes). Each sector is associated with a lower port through which the feeding pipework is routed. The toroidal angular range of a sector is 22.5° Each sector corresponds to a toroidal field (TF) coil (16 TF coils in total). It is noted that ITER has 54 cassettes (18 TF coils). The reduced number of TF coils of the DEMO allows a wider toroidal solid angle of the space available for remote maintenance of a breeding blanket segment through an upper port. On the other hand, the reduced number of cassettes has the impact that the thermal power to be deposited in each cassette becomes larger requiring a larger cooling capacity per cassette.

Fig. 7 shows the CAD configuration model of a typical sector consisting of three cassette modules (left: top view, right: view through the lower port). The cassettes in the sector are almost identical except for some minor differences. The spacing between two adjacent cassettes is 20 mm.

The CAD model of a typical divertor cassette module is illustrated in Fig. 8. A cassette module occupies the toroidal angular range of 7.5° In Table 4, the major design constituents are listed with a brief description of the functions.

For realizing system integration, numerous interface issues must be considered on the plant level:

- Compatibility of the CFS, CB and CCOR design with the remote handling scheme.
- Compatibility of the feeding and outlet pipes with the lower port configuration.
- Interface between the CB and the inboard in-vessel coils and toroidal transport rail.
- Gas conductance for pumping.
- Nuclear shielding for the VV and the magnets.

Table 4
Major constituents of a divertor cassette module and the functions.

Subcomponents/empty weight (kg)	Functions
Cassette Body (CB) /5650 /6918 (with coolant)	• holds all sub-components. • protects the VV from neutron flux and radiation. • provides flow channels to exhaust gas. • exhausts heat from nuclear heating.
Inner Vertical Target (IVT) /345	• intersects and neutralizes the SOL particle flux (inboard). • exhausts heat from SOL particles, radiation and nuclear heating.
Outer Vertical Target (OVT) /471	• intersects and neutralizes the SOL particle flux (outboard). • exhausts heat from SOL particles, radiation and nuclear heating.
Shielding Liner (SL) /1186	• shields the CB pumping duct to protect the VV from neutron flux and X-point radiation. • provides gas flow channels pressing the exhaust gas. • prevents upstreaming and reflux of gas into the plasma. • exhausts heat from nuclear heating and X-point radiation.
Reflector Plates (RP) /64 (inner), 91 (outer) /31 (supports)	• protect the cooling manifolds from neutron, particles and radiation. • enhance the particle exhaust • exhaust heat from nuclear heating and radiation.
Cooling pipes & manifolds /281	• transport coolant for feeding and circulation.
Cassette Fixation Supports (CFS), inboard/outboard /132 (wishbone)	• attach and fix the CB to the VV (inboard, outboard). • provide elastic compliance for preloading and for compensating the mismatch of differential thermal strains between CB and VV.
Central Cassette Outer Rail (CCOR)/installed in VV	• provides a supporting interface between the central CB and the VV for toroidal transport of a module.
Inboard Toroidal Transportation Rail (ITTR)/ installed in VV	• support CB against the gravity load during toroidal transportation. • accommodate in-vessel magnet coils for strike point sweeping.

• Connection of the cooling circuits to the PHTS, etc.

3.3. Cassette body [14,15,33,34]

The CB accommodates and holds all subcomponents of a cassette module (see Fig. 8). A square-shaped pumping duct is located in the central region penetrating through the CB. This duct is the main gas flow channel towards the pumping ports. The CB hosts many internal chambers separated by ribs. The CAD drawings in Fig. 9 show the typical interior cut views of the CB (together with the SL and RPs). The ribs are 20 mm thick, the outer wall is 30 mm thick. The ribs act as stiffeners for structural robustness and as partition walls (with holes) at the same time for guiding coolant streaming. The structural material of the CB is EUROFER97 steel. The key properties of EUROFER97 are found elsewhere [35]. One of the side walls has a trench to shield the cooling pipe.

3.4. Targets (inboard/outboard) [14,15,34,36,37]

Each cassette module is equipped with a pair of IVT and OVT. The targets are deemed to be the most important and technologically critical component. The so-called ITER-like target design was chosen as baseline [38]. This design is characterized by tungsten monoblock armor and copper alloy cooling pipe.

Fig. 10 shows the CAD model of the targets (a: IVT, b: OVT, c: coolant stream distributor manifold, d: technical drawing of the manifold). The support legs are omitted in the figure for brevity. The planar area has the poloidal length of 700 mm. The strike point is assumed to be located at the central region of the targets with a Gaussian distribution of power density (poloidal extension: ~100 mm). The strike point will be swept over a poloidal range of ±200 mm in an off-normal plasma reattachment event to mitigate the time-averaged heat flux. Each target plate consists of a parallel array of many target elements (IVT: 32, OVT: 44) in the toroidal orientation. The weight of the targets amounts to 345 kg (IVT) and 471 kg (OVT), respectively. The cooling pipes of each target are connected to the respective feeding pipe via a stream distributor manifold where 5 ribs act as baffle walls.

Each target element consists of a longitudinal array of rectangular tungsten armor blocks connected by a long cooling pipe (CuCrZr alloy) running through the center bore of the blocks. The pipe is joined to the blocks via a 1 mm thick interlayer (soft copper). Fig. 11 shows the CAD

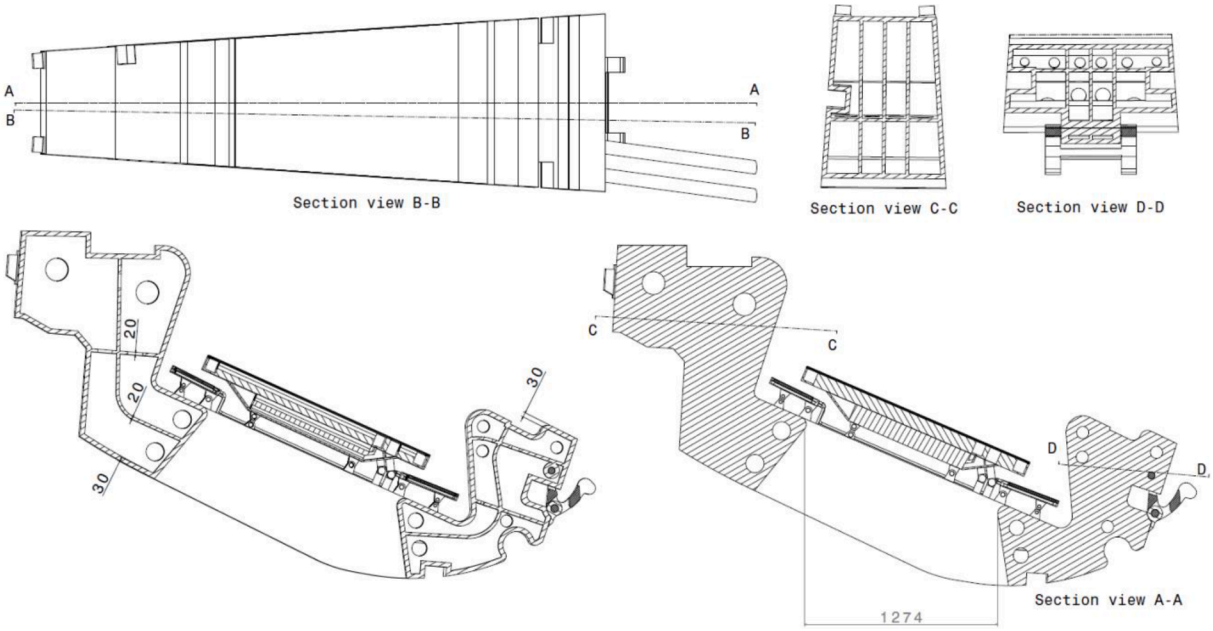

Fig. 9. Technical drawings showing the cut views of a cassette body with shielding liner and reflectors.

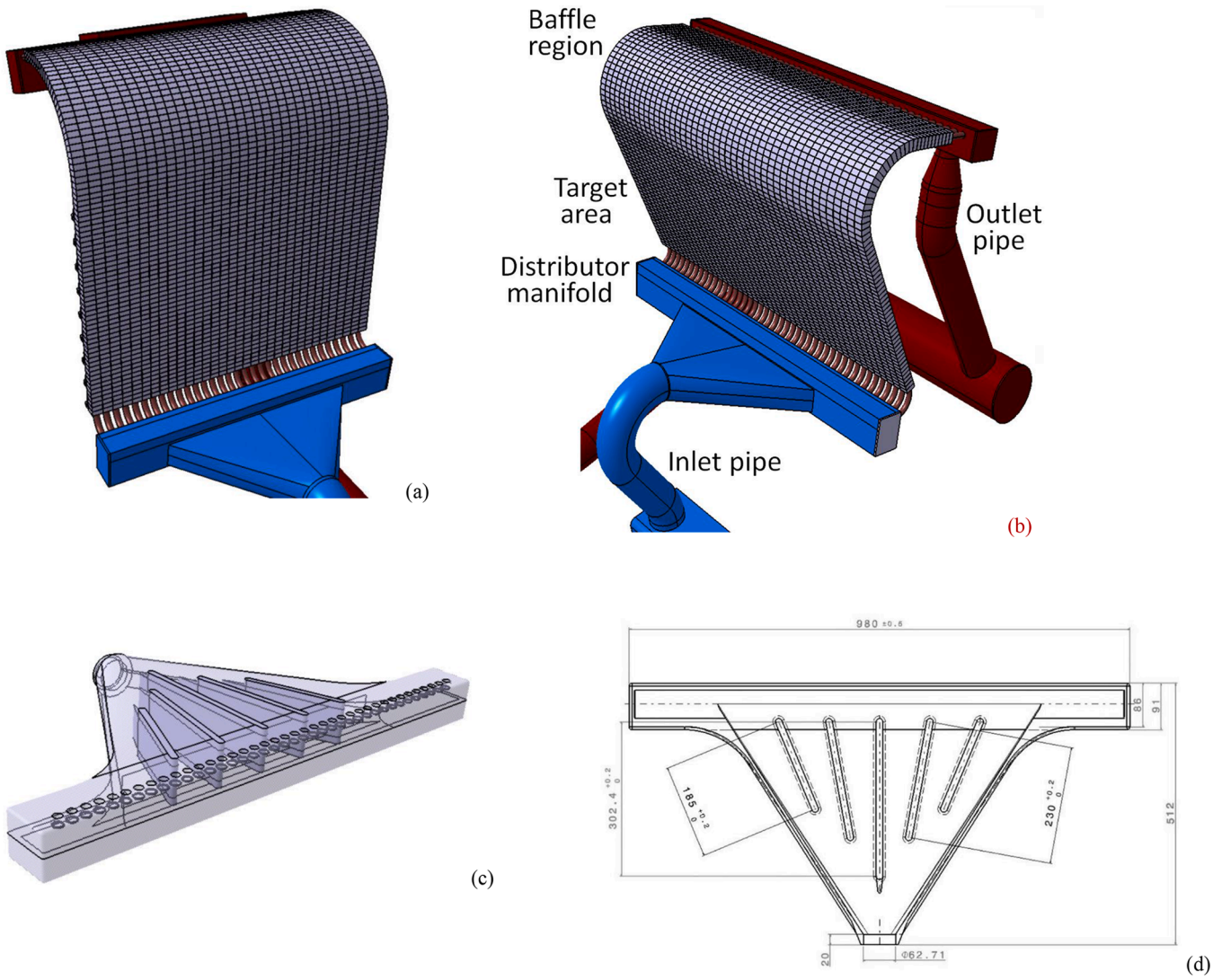

Fig. 10. Inboard (a) and outboard target (b) and coolant stream distributor manifold (c, d).

model of a typical target element segment (a) and the technical drawings (b: lateral view, c: longitudinal section, d: cross section). The gap clearance between tungsten monoblocks are 0.5 mm in both toroidal and poloidal direction. The gap clearance is kept constant over the entire target areas including the curved baffle region. In the upper baffle region, the axial section of the monoblocks are tapered (forming a trapezoidal shape) so that the gap clearance remains constant along the curvature. Given that the current design was produced in the framework of the PCD where detailed design was beyond the scope, design details such as chamfering of the armor front face were not dealt with but shall be elaborated in the later engineering design phase. The strategy of ITER to handle the leading edge issue (e.g. chamfering and alignment of monoblocks) will be considered as a reference also for the DEMO divertor.

Fig. 12 shows the CAD model of a typical single monoblock unit (a) and the components of the fixation unit (b). The design is de facto identical to the ITER monoblock target design except for the section width (23 mm instead of 28 mm) [38]. The reduced width dimension has a beneficial effect with regard to structural integrity when a fatigue crack is initiated at the armor front face. In this case, the crack tip stress intensity is substantially decreased [39–41].

The rather thick front side armor thickness (8 mm) was adopted to maximize erosion lifetime accepting higher surface temperature as trade-off. If the lifetime of the armor is not dictated by erosion, the initial armor thickness could be further reduced in favor of lower surface temperature. At 20MW/m^2, the front face temperature raises from 1300 °C to 2290 °C when the armor thickness increases from 4 mm to 8 mm [39]. Should the targets be subjected to slow transient events (~20MW/m^2) several hundred times, the cumulative heat exposure time will be long enough to induce substantial recrystallization in the tungsten armor resulting in a considerable reduction of yield stress, particularly in the upper region near the front face. This thermal softening promotes plastic deformation potentially leading to a fatigue crack initiation [39]. However, the mock-ups of this baseline design showed no crack formation at all even after 1000 loading cycles at 20MW/m^2 even though the upper half of the armor had been fully recrystallized. This finding will be revisited later (chapter 7). Under the normal operation condition (~10MW/m^2), the temperature at the front face of the 8 mm thick armor is not higher than 1110 °C. Thus, recrystallization will not be an issue for the normal operation case.

The dimension of the interlayer and the cooling pipe were inherited from the ITER target design. The effect of the interlayer thickness with respect to structural integrity was studied in terms of fracture mechanics and HHF fatigue resistance (thickness range: 0.1–1 mm) [42,43]. These studies manifested a beneficial stress relaxation effect of the soft interlayer leading to a superior performance.

The design of the target fixation unit was inherited from ITER. The unit is made of EUROFER97 steel. The attachment legs are brazed to the

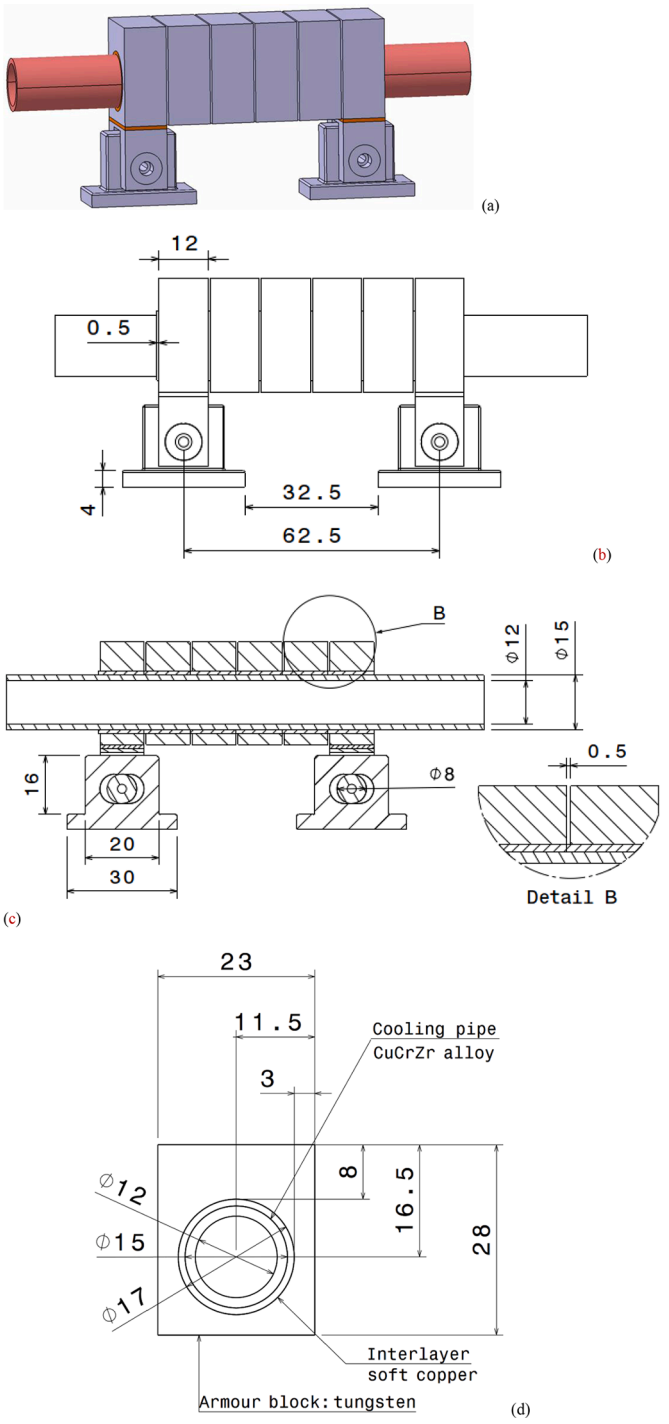

Fig. 11. A typical target element segment and technical drawings (a: CAD model, b: lateral view, c: longitudinal section, d: cross section).

tungsten blocks. The legs are fixed to the underlying plug by a pin and two pin locks at both ends. The targets are directly attached onto the CB via the fixation units. To ensure electric insulation of the target from the CB (except for one shunt position), the contact surfaces of all constituents within the attachment unit shall be coated with a thin ceramic film [37]. The insulation is required for a diagnostic purpose to detect reattachment events by measuring an abrupt change of thermo-currents. The materials specified for the target elements are listed in Table. 5.

The target attachment scheme is different from that of ITER: In ITER, targets are first attached to a so-called plasma-facing unit (steel), which is further attached to the cassette body. In the DEMO, the targets are

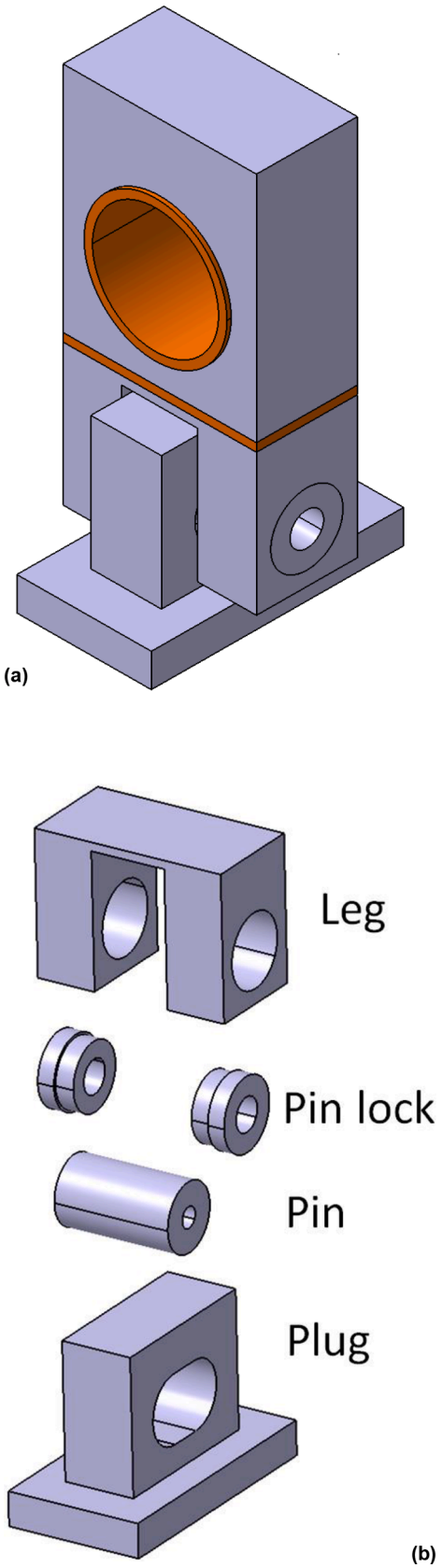

Fig. 12. A typical single monoblock unit (a) and the fixation unit (b).

Table 5
Materials specified for the target elements.

Armor block	pure tungsten (hot rolled and stress-relieved)
Interlayer	Soft OFHC copper (casted)
Cooling pipe	CuCrZr alloy (seamless drawn)
Attachment unit	EUROFER97 steel
Insulation coating	Ceramic coating (oxides, nitrides)

directly attached to the CB via the fixation units.

3.4. Shielding liner [14,15,33,34]

Fig. 13 shows the SL (a: CAD model, b: longitudinal cut section displaying the coolant flow path). The technical drawings of the SL and its internal cooling channel architecture is shown in Fig. 14. The heat sink hosts four stack layers of cooling channels for effective cooling and moderation. The channels are aligned in the radial direction. The cooling circuit inside of the SL is connected in series with a forward and return flow. The inflow coolant from the SL inlet is first fed into the uppermost front face channels which are subject to the maximum nuclear heating power density. The coolant is further routed to the underlying cooling channels towards the bottom and finally back to the CB via the SL outlet. The channel architecture and the dimensions are the outcome of an iterative thermo-hydraulic optimization.

The structural material is EUROFER97 steel. The front face of the steel heat sink plate is armored with a tungsten coating (2 mm) to ensure physical compatibility with the plasma (low sputtering yield) and to protect the steel structure from neutron flux, radiation and gas particles. The four multi-link supporting legs allow for differential thermal expansion of the SL relative to the CB. Each leg consists of two single hinges on the outboard side and two double hinges on the inboard side. The size of the passively cooled legs was minimized to avoid overheating by nuclear heating. Structure-mechanical analyses verified the structural integrity against coolant pressure and thermal stresses. The dimensioning of the SL was made considering four factors:

- Cooling capacity to cope with the nuclear heating and radiation power (from the separatrix X-point);
- Structural resilience against impact loads and thermal stresses;
- Nuclear shielding capacity for protecting the underlying supporting legs;
- Gas conductance for particle exhaust.

The relatively complex geometry poses a technological challenge for manufacturing. There are still two critical design concerns:

- Excessive irradiation damage of the heat sink leading to embrittlement (remaining unsolved);
- Intensive nuclear heating of the supporting legs leading to thermal softening (within the limit);

The SL is one of the most salient design features deviating from the ITER divertor. The SL replaces the so-called dome of the ITER divertor for shielding and gas compression. The primary motivation to adopt the SL instead of the dome was to reduce production costs by simplifying the design and manufacture technology.

3.5. Reflector plates [34]

Fig. 15 shows the CAD model of the RPs (a) and their configuration (b). The RPs cover the feeding pipes of the targets and manifolds. The structural material is EUROFER97 steel. The front face is armored with tungsten coating (currently, 3 mm).

Fig. 16 is the technical drawing of the cross section showing the internal cooling channel architecture. The cooling circuits of the inboard and outboard RPs are connected in series (mean heat flux density: ~0.2MW/m^2).

3.6. Cassette fixation supports [15,34,44]

The CB is attached and fixed to the VV by means of the inboard and outboard cassette fixation support (CFS). In addition, the inward-oriented magnetic force exerting on the fully magnetized ferromagnetic CB (EUROFER97 steel) strongly (300–400 kN) pulls the CB towards the inboard wall of the VV during operation [44]. The origin of this inward pulling force is the static magnetic attraction between each

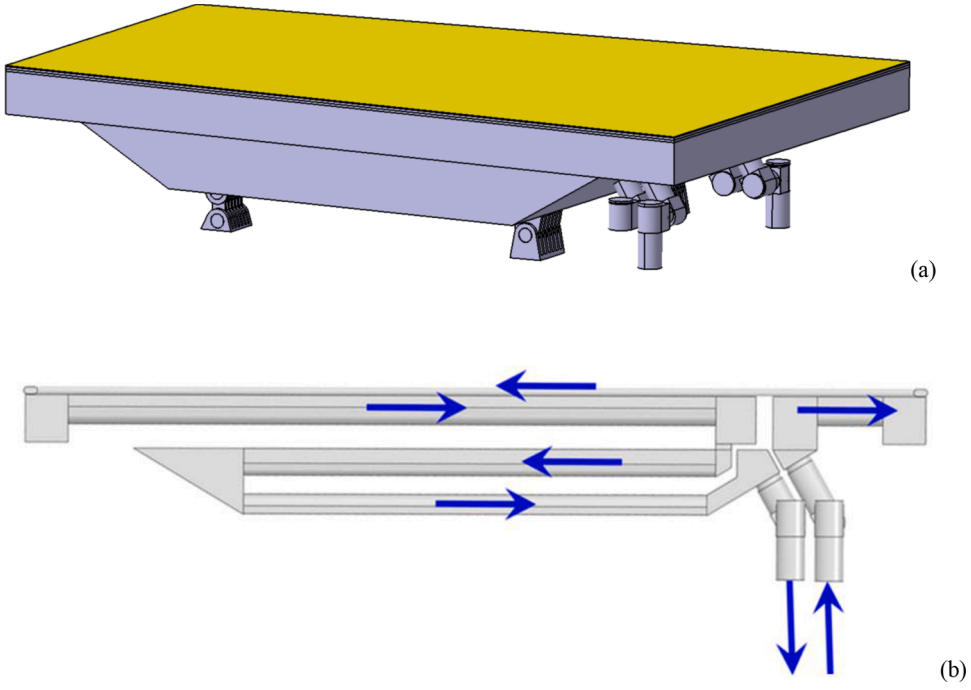

Fig. 13. Shielding liner (a: CAD model, b: longitudinal cut section displaying the coolant flow path).

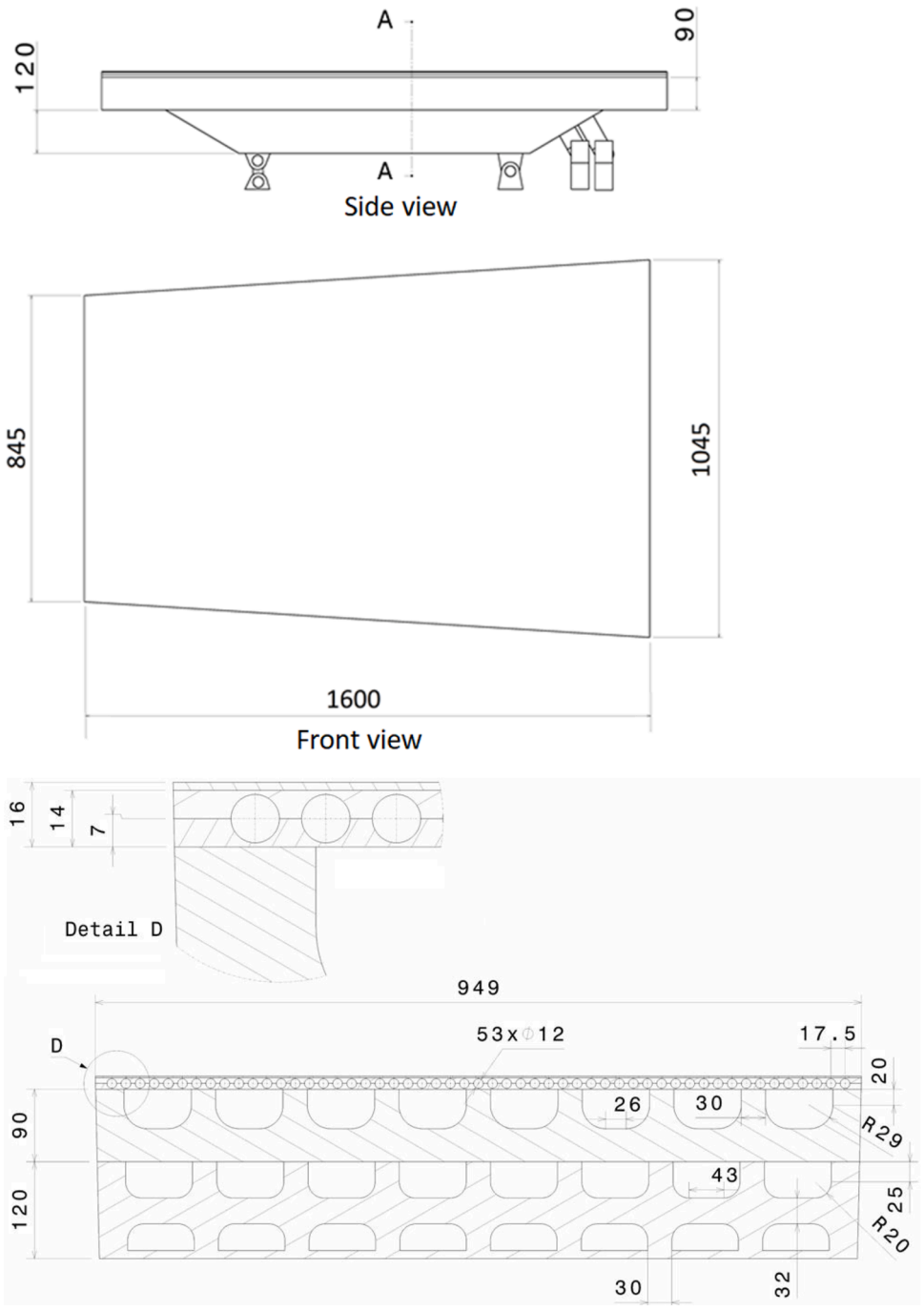

Fig. 14. Technical drawings of the SL cooling channel architecture in the shielding liner (middle section).

radial pair of CBs standing vis-à-vis, respectively. It is noted that all radial pairs of CBs are oppositely magnetized at the inboard wings by the toroidal magnetic field. This attractive inward magnetic force is beneficial for fixation and for ensuring electrical contact between CB and VV as it exerts additional radial compression. However, it is expected that the magnetic force will decrease (by 25%) when the material loses the intensity of saturate magnetization (via decrease of magnetic permeability) due to irradiation damage during long-term operations [45].

Fig. 17 shows the CAD model of the inboard CFS. This CFS consists of a nose-socket pair featured on the inboard edge face of the CB and on the inboard wall of the VV, respectively. Once engaged, the locking gives rise to full constraints against toroidal and poloidal displacement maintaining the specified gap between the blanket edge and the CB.

Fig. 18 shows the CAD model of the inboard toroidal transportation rail (ITTR). During transportation, the cassette moves being supported by the roller bearings. The rail serves for two-fold functions:

- to offer static support against the gravity load of a cassette during toroidal transportation,
- to accommodate the in-vessel magnet coils (shielded by the CB) for strike point sweeping.

Fig. 19 illustrates the outboard CFS including the wishbone (a: before engagement, b: after locking, c: alternative wishbone design). In addition to fixing function, the wishbone provides elastic compliance and static resilience to accommodate the mismatch in thermal strains between the CB and the VV. Noting that the temperatures assumed are still subjected to change during the design phase, the origins of this strain

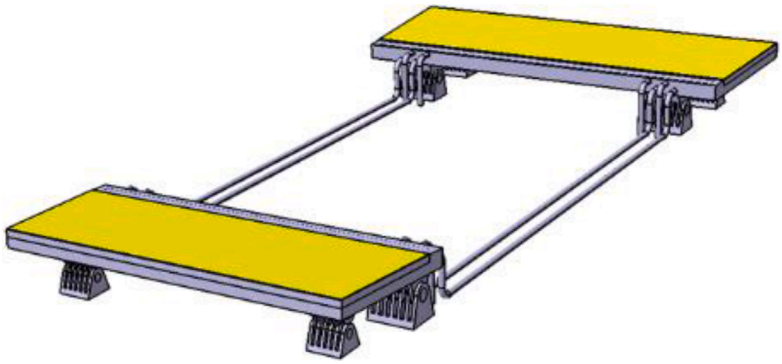

(a)

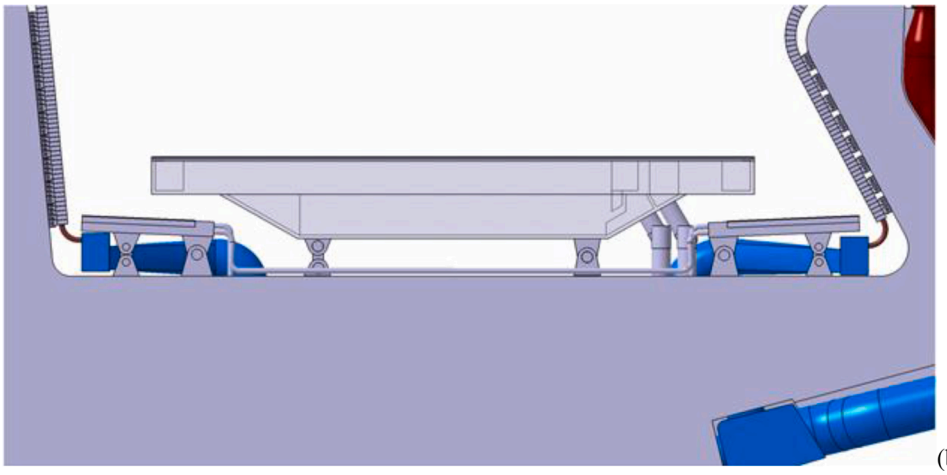

(b)

Fig. 15. CAD model of the reflector plates (a) and their configuration (b).

mismatch are:

- different coolant temperature during operation (CB: 180–210 °C, VV: 40 °C);
- different baking temperature (CB: 240 °C, VV: 180 °C);
- differential thermal expansion coefficients (CB: EUROFER97, VV: AISI 316L(N)-IG);
- different nuclear heating power density;

The relative difference in the radial displacement due to differential thermal strains between the CB and the VV amounts to 5.6 mm (compressive) during the normal operation and 1.5 mm (tensile) during the baking. The wishbone must have a sufficient strength under such displacement loads. Ti-6Al-4 V alloy was selected as material for the wishbone to exploit its high elasticity and strength. By means of a multi-step locking operation, the wishbone and the CB are put into elastic compression towards the inboard VV so that the CB is fixed, electrical contact is established and loads are transferred from the CB to the VV in the vertical and toroidal directions.

The elastic stiffness of the wishbone (Fig. 19a) amounts to 30MN/m (< 9% of the CB). Degradation of elasticity by neutron irradiation was taken into account (decrease by 40% after 1.5 fpy). The pins (alloy 660 steel) have the diameter of 60–100 mm to withstand the shear force (~400 kN) under impact loads. A sufficient clearance is needed for the locking and unlocking operation.

3.8. Remote installation sequence [34]

When deployed, each cassette is transported by a robot arm into the vessel through the allocated Lower port. Once reaching the correct radial position in the vessel, the cassette is lowered vertically by 20 mm until it touches the supporting rollers placed on the inboard and outboard toroidal rail (ITTR and CCOR), respectively (see Fig. 20). Then the cassette is transported along the toroidal rails towards its specified toroidal position. Subsequently, the cassette is pushed radially inwards against the inboard side supports until the radial displacement reaches roughly 30 mm. This operation leads to a vertical lift of the cassette by about 15 mm. Under the action of the radial push the noses of the inboard wing are engaged into the supporting sockets on the inboard VV wall. Simultaneously, the outboard support is slightly rotated in the poloidal orientation by this motion. Once the outboard support and the wishbone are located at the correct positions, the last pin is inserted into the hole of the wishbone/support joint for fixation. Finally, the rollers are removed leaving the cassette fixed at the inboard and outboard supports. The diameter of the pins must be thick enough (100 mm) to resist against electromagnetic impact loads upon disruptions.

The fixation system of the central cassette is inevitably different from that of the lateral cassettes due to the open space in front of the Lower ports. For the central cassette, the outboard support was designed in form of a cross beam (with an L-type section) that bridges the port opening and fixed to the both side walls of the port. This support should be easily removable during a maintenance operation in order to allow quick access to the lateral cassettes. The detailed geometry and the installation sequence are found in [34].

When retracted, each cassette is removed remotely as a whole and delivered first to the external hot cell of the plant. Currently, *ex-situ* refurbishment for reuse of the cassette is not envisaged. Recycling of the structural materials (after melting for removing transmuted gas) seems to be the only feasible option. A dedicated study is ongoing with regard to recyclability for reducing nuclear waste and costs. The feeding and

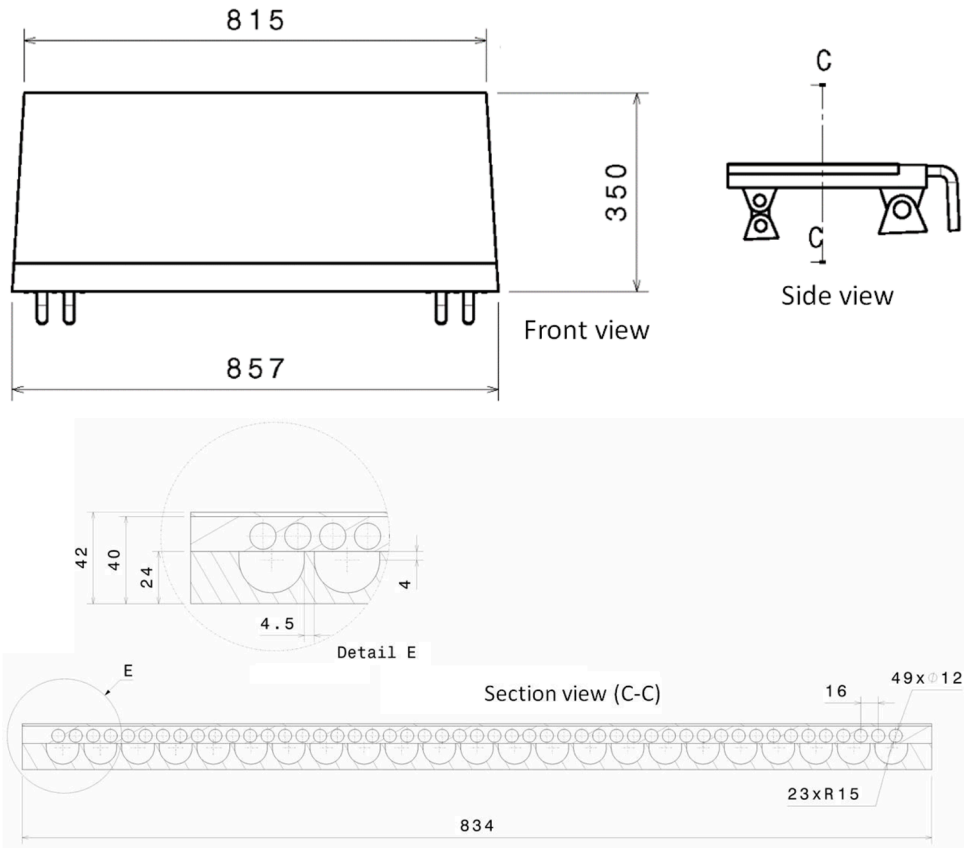

Fig. 16. Technical drawing of the reflector plate showing the cross section with the cooling channels.

exhaust cooling pipes are cut and rewelded at rear positions behind the CB where nuclear load is acceptably low for rewelding. Fig. 31 and 32 show that the irradiation damage dose rate and the helium production rate at those positions amount to 0.01dpa/fpy and 0.1appm/fpy, respectively. Although these values seem subcritical, a dedicated experimental verification is needed.

4. Divertor cooling scheme

4.1. Requirements and constraints

The thermal loads listed in Table 1 indicate a drastic difference in the power density between the targets ($\leq$20MW/m^2) and the rest parts of the cassette ($\leq$1MW/m^2, $\leq$8MW/m^3). On the other hand, the acceptable service temperature ranges of the respective structural materials (IVT/OVT: CuCrZr-IG, CB/SL: EUROFER97) do not fully overlap with each other. These distinct differences implicate the necessity of a separate cooling scheme with two cooling circuits each dedicated for the HHF components (targets) or medium heat flux components (CB, SL, RP). The paramount cooling requirement for the HHF components is to ensure a sufficient margin to the critical heat flux (CHF) at the strike point under all off-normal operation events so that local film boiling is avoided (initial nucleate boiling is accepted). A similar requirement applies to the other components as well, but the criticality of the off-normal events is far less relevant.

From the cooling point of view, the coolant temperature should be kept as low as possible to maximize the margin to the CHF. However, from the structural reliability point of view, it is desirable to operate the (irradiated) components above the ductile-to-brittle transition temperature (DBTT) of EUROFER97 and the thermal recovery temperature of CuCrZr to maintain ductility. Unfortunately, the two contradictory requirements can hardly be satisfied simultaneously even if a dual cooling scheme with separate cooling circuits is adopted. Therefore, a prudent engineering compromise is inevitable.

4.2. Heat flux distribution

The distribution of the nuclear heating power density generated in the cassette is plotted in Fig. 21. The highly non-uniform power density is attributed to the rapid attenuation of neutron flux through the depth. The solid body exhibits a similar heat flux distribution as the coolant. Fig. 21 reveals that the heat flux density near the plasma-facing front face (5–8MW/m^3) is at least an order of magnitude higher than that of the rear parts (0.1–1MW/m^3) suggesting that the colder inlet coolant should be fed first into the front side (IVT/OVT and SL). The total volumetric thermal power (339MW) amounts to 17% of the fusion power. The individual contributions are broken down as follows (for the entire divertor) [44,46,47]:

- Volumetric heat in the solid body of the cassettes: 85MW;
- Volumetric heat in the solid body of the supports: 17MW;
- Volumetric heat in the coolant fluid of the cassette: 37MW;
- Surface heat on the targets (by particles and radiation): 122MW;
- Surface heat on the SL and RPs (by radiation): 78MW;

4.2. Cooling circuits and cooling conditions

In the PCD phase, the dual cooling scheme was adopted as baseline. The two cooling circuits are shown in Fig. 22 (a: cooling circuit of the CB, SL and RPs, b: cooling circuit of the targets). The cooling circuit of the targets comprises the pipework of the IVT and OVT connected in parallel by a feeding and exhaust pipe (DN125 schedule 40) via the distributor manifolds. The other cooling circuit consists of the cooling channels of the CB, SL and RPs. The latter circuit is the combination of a

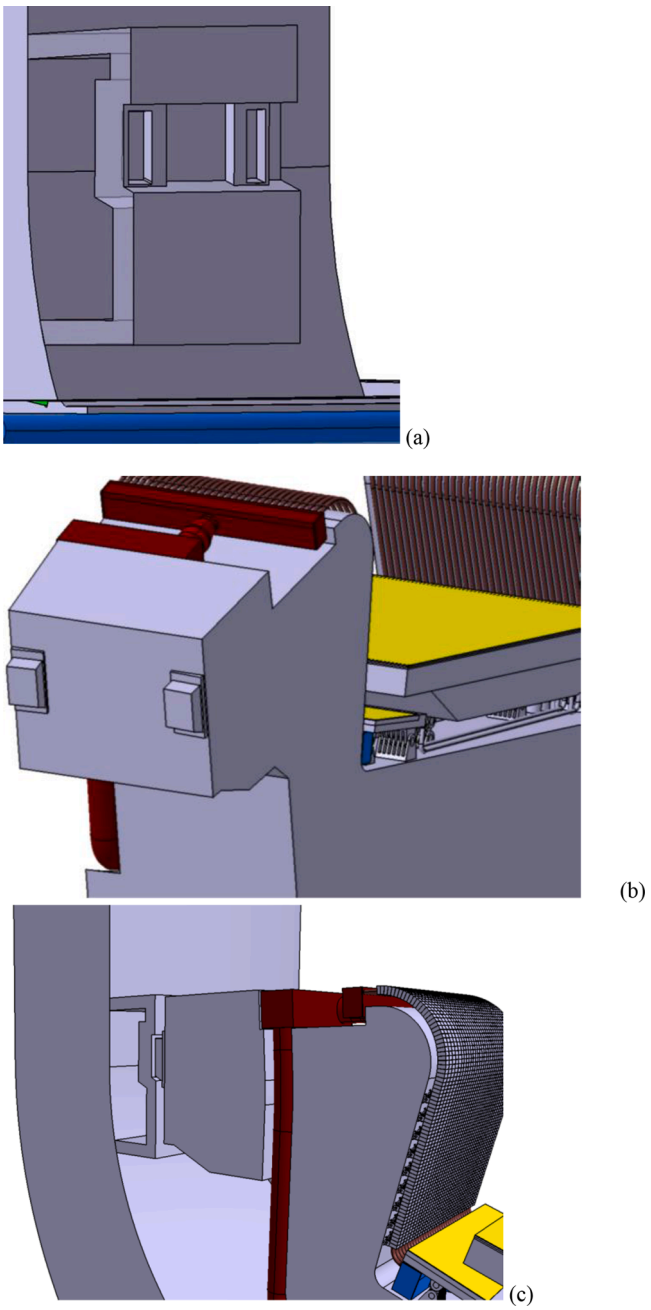

Fig. 17. Inboard cassette fixation support (a: socket, b: nose, c: view after locking).

series connection (CB-to-SL, CB-to-RPs) and a parallel connection (SL-to-RPs) of the channels with a common feeding and exhaust pipe (DN80 schedule 40). The configuration and dimension is the outcome of an iterative hydraulics design optimization [48–53].

Fig. 23 shows the schematic flowchart of the cooling circuits (a: cassette body, b: targets).

The hydraulic parameters of the coolant defined for the targets and the CB (incl. SL and RPs) are listed in Tables 6 and 7, respectively [47,54]. The predicted hydraulic behavior was verified by an experimental test using a full-scale prototype mock-up of the OVT at a water-loop equipped with a diverse diagnostic instrumentation system [55].

The cooling conditions for the targets were derived from the requirement to ensure a safety factor of 1.4 (i.e. 40% margin) to the CHF (45MW/m^2 at the cooling pipe inner wall) under the applied front face heat flux of 20MW/m^2 (defined as technology goal) in thermal

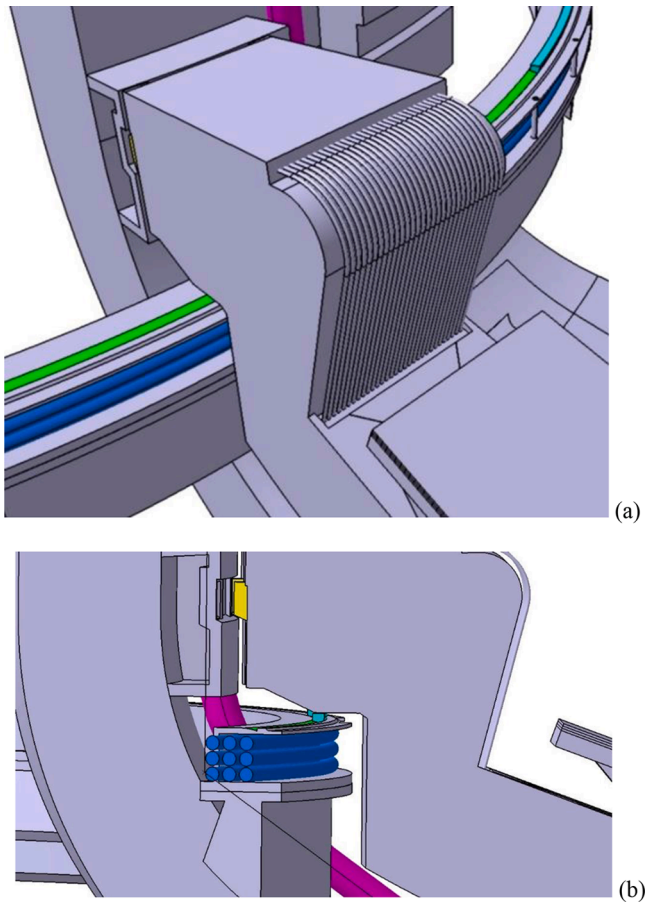

Fig. 18. Inboard toroidal transportation rail supporting a cassette during toroidal transportation (a, b).

equilibrium (pulse: ≥10 s) [56]. Assuming a swirled cooling pipe (inner diameter: 12 mm), the maximum possible local coolant temperature at the strike point is about 137 °C (see Fig. 24), which is definitely lower than the thermal recovery temperature (150–200 °C) of irradiated CuCrZr alloy [57,58]. This conflicting circumstance is illustrated in Fig. 25.

The use of such a low-temperature coolant for the (irradiated) targets can be justified when a fracture mechanics-based structural design is applied. The toughness of irradiated (thus embrittled) CuCrZr alloy increases with decreasing temperature below 200 °C [59]. The beneficial effect of this peculiar property was manifested in a theoretical study of the fracture behavior of a crack in the cooling pipe [60].

Furthermore, the inherent conservativism of the elastic design rules can be substantially relaxed if total ultimate tensile strain (≤6%) is adopted as failure criterion instead of uniform elongation limit (≤1%) for irradiated CuCrZr alloy [61,62].

The coolant of the CB was set to a temperature range from 180 °C (inlet) to 210 °C (outlet), which lies far below the desired temperature range (300–550 °C) of irradiated EUROFER97 steel. The reason for taking this low-temperature coolant is the same as the case of the targets, namely, to prevent bulk boiling crisis as well as sub-cooled film boiling. On the other hand, the local temperature in the highly stressed regions should be higher than the fracture toughness transition temperature (FTTT) of irradiated EUROFER97 steel (see Section 5.1). This rationale tacitly assumes that a fracture mechanics-based non-ductile design rule shall be applied. The detailed description of this issue is found elsewhere [63,64].

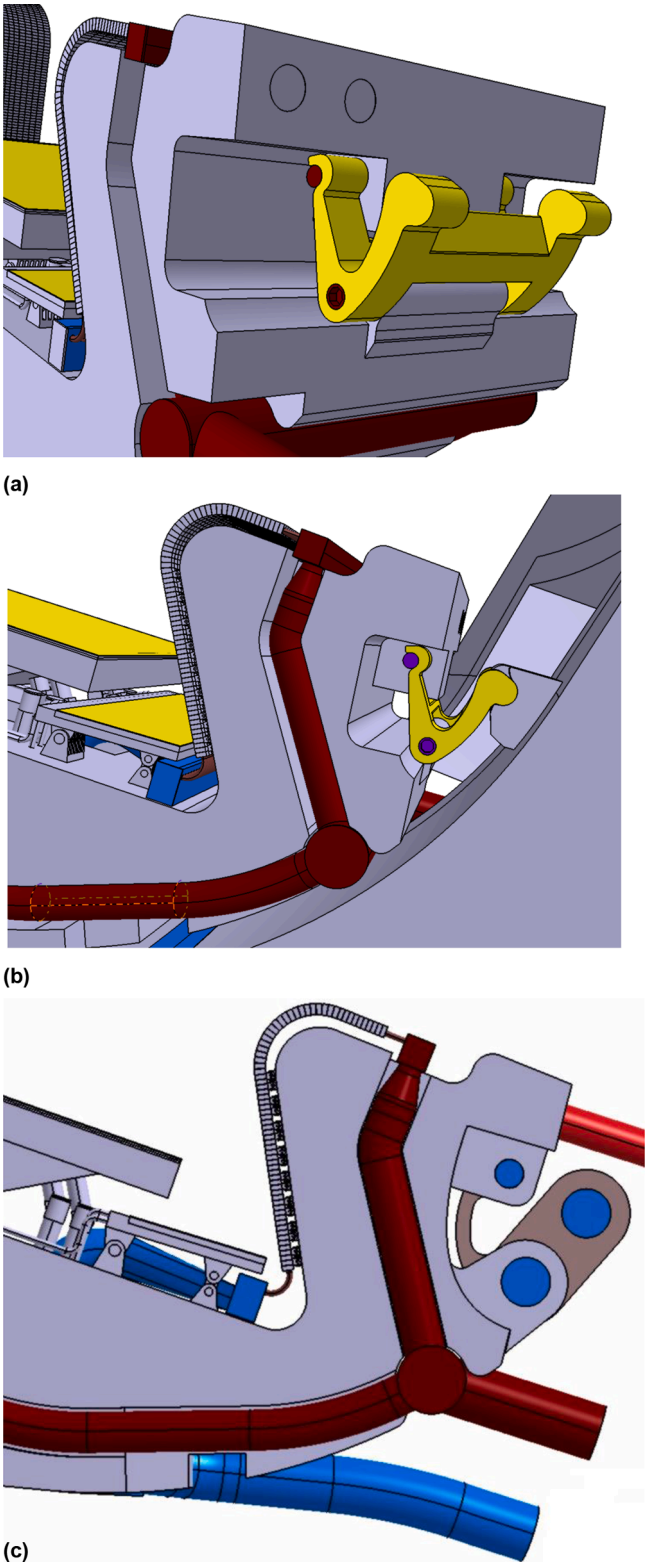

Fig. 19. Outboard cassette fixation system with the wishbone (a: before engagement, b: after locking, c: alternative wishbone design).

4.3. Cooling performance [47,54]

The cooling scheme was verified by computational fluid dynamics analyses to demonstrate a reasonable cooling performance. The overall thermohydraulic coolant behavior of the both circuits are presented in Figs. 26–31. Fig. 26 depicts the coolant stream lines and the axial velocity field in the OVT. A highly uniform velocity distribution across the pipes in the toroidal array is seen (average: 14.4 m/s, standard deviation: 0.3 m/s). Such a uniform distribution of streaming velocity among the pipes is realized by the distributor manifold. In the straight segment of the cooling pipes, the flow velocity increases reaching the maximum owing to the reduced effective cross-section area (in the presence of the inserted swirl tape). In the curved segment (baffle), velocity is reduced due to the curvature where the fluid experiences a stronger boundary layer friction due to higher vertical momentum component normal to the pipe wall.

Fig. 27 shows the coolant pressure field in the target cooling circuit. The total cumulative pressure drop is less than 1 MPa, which is fully acceptable. The pressure drop is caused mostly (84–93%) due to the turbulence loss in the diffuser manifolds and the friction by the swirl tapes The average margin to the CHF at the strike point reaches 43% (inboard) and 52% (outboard). Thanks to the hydraulic uniformity in the toroidal direction, all target elements exhibit a similar heat removal capacity (deviation: 1–2%).

Fig. 28 shows the pressure and the temperature field of the coolant in the CB, SL and the RPs. The total cumulative pressure drop (except for the targets) amounts to 0.6 MPa, which is fully acceptable. 64% of this pressure drop occurs in the SL whereas the CB gives a contribution of only 25%. The coolant temperature exhibits a uniform distribution except for the cold outboard inlet region. The total temperature rise amounts to 30 °C. The margin against the saturation temperature at the CB outlet amount to 22 °C. The SL exhibits a uniform distribution of axial flow velocity across the channels (4.9 ± 0.1 m/s) and large margin to the CHF (min.: > 6, 6.3 ± 0.1). The RPs show a rather non-uniform distribution of axial flow velocity across the channels (1.2 ± 0.8 m/s), but exhibit a very large margin to the CHF (min.: >10, 16.0 ± 4.9).

Concerning cooling efficiency and safety, the most important quantity is the margin between the local coolant temperature (T_c) and the local saturation temperature (T_s) of coolant vaporization at that position. Owing to the limited pressure drop (decrease by 17% in total) in the cassette, the decrease of T_s assessed between the inlet and the outlet of the CB is accordingly small (~10 °C). Fig. 29(a) shows the distribution of the margin ($\Delta T_{s\text{-}c} = T_s\text{-}T_c$) between T_c and T_s in the coolant domain (only the envelope of the fluid interface to the solid wall is displayed). Fig. 29(a) reveals that $\Delta T_{s\text{-}c}$ is mostly larger than 10 °C in the coolant bulk (note that the boundary layer near the wall interface is hotter than the underlying fluid bulk). However, there are regions of concern in the coolant near the front face wall of the upper inboard wing where $\Delta T_{s\text{-}c}$ is either quite small (red region) or even exhausted (gray region). The occurrence of these hot spots are attributed to the facts that the highest nuclear heating power density (~8MW/m^3) prevails in the front face wall while the coolant reaching the inboard wing has already been heated up in the SL and RPs undergoing a pressure drop. The reduced pressure decreases local saturation temperature. The layer thickness of the negative margin region is very thin (a few μm) and $\Delta T_{s\text{-}c}$ is small, thus only modest sub-cooled nucleate boiling at the fluid-wall interface is expected to occur rather than film boiling. Here, a further design improvement is needed (e.g. applying higher inlet pressure or modifying flow routes) in order to increase T_s or to enhance stream velocity (see Fig. 29(b)). The local values of T_c, T_s and $\Delta T_{s\text{-}c}$ at selected positions are given in Table 8. Table 8 confirms that there is no risk of extensive bulk boiling throughout the entire cassette where the minimum $\Delta T_{s\text{-}c}$ (at the outlet) is still larger than 22 °C.

It is noted that the $\Delta T_{s\text{-}c}$ values in Table 8 refers to the margin against bulk boiling assessed at the channel center whereas the margin depicted as color code in Fig. 29(a) indicates local $\Delta T_{s\text{-}c}$ distribution at the superheated fluid-wall interface. In the interfacial boundary layer, flow velocity is low and convective heat transfer is reduced leading to a vertical temperature profile from the T_c near the wall interface down to the T_c in the bulk. The boundary layer explains the difference in the $\Delta T_{s\text{-}c}$ values between Table 8 and Fig. 29(a). An outstanding example of this boundary layer effect is the SL back channels which appear as reddish

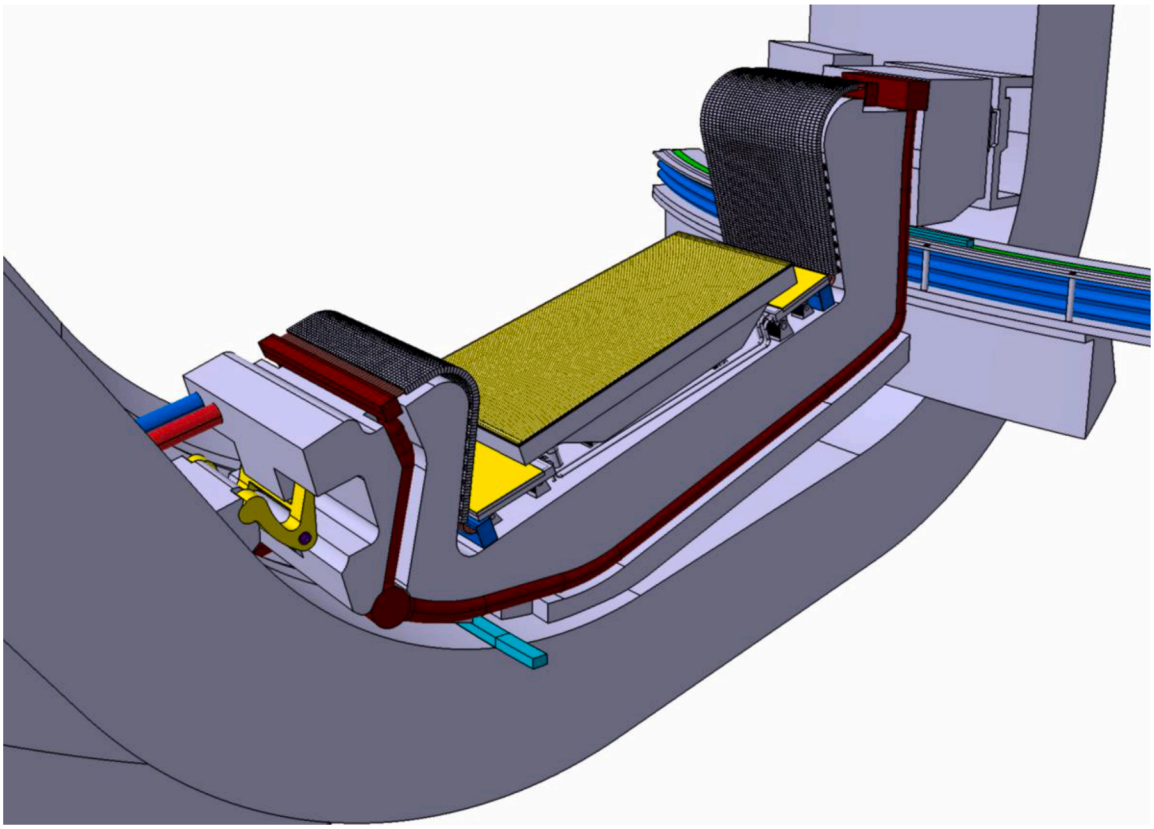

Fig. 20. Divertor cassette placed on the supporting rollers on the inboard and outboard toroidal transport rails.

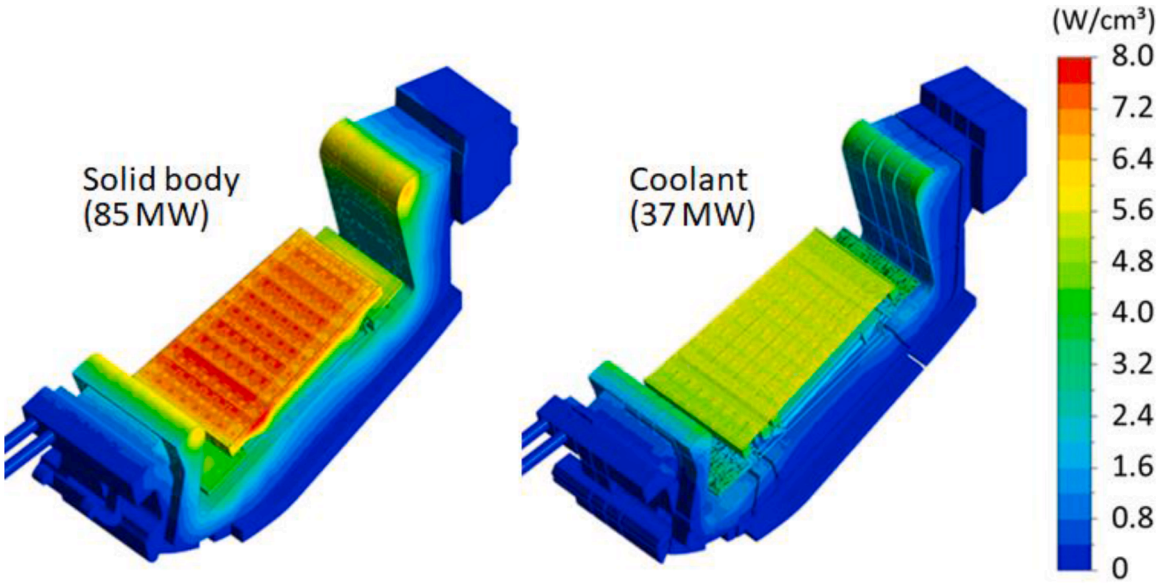

Fig. 21. Distribution of volumetric thermal power density generated by nuclear heating in the cassette (left: heat flux density in the solid body, right: heat flux density in the coolant fluid).

region in Fig. 29(a). Although the $\Delta T_{s\text{-}c}$ in the boundary layer at the wall is so small ($\leq$5 °C), the $\Delta T_{s\text{-}c}$ in the channel bulk is still large enough (>27 °C) even though the flow velocity is strongly reduced (down to 25%).

Fig. 30 shows the equilibrium temperature distribution building up in the solid body (steel) of the cassette. The total temperature range spans from 200 °C (the rear regions) to 555 °C (the SL legs), but for the most part of the CB, the temperature is below 250 °C. In this 'cold' region, the irradiation damage dose rate ranges from 0.1 to 2dpa/fpy. This means that the irradiated CB would remain mostly in a non-ductile state (if not fully embrittled) after a certain operation period.

For this embrittled region, the structural integrity must be verified based on proper failure criteria capturing fast fracture and fatigue crack growth [65]. In this practice, the dependence of toughness and fracture mode on multiple parameters (temperature, damage dose, stress tri-axiality and equivalent stress) must be considered. The lack of

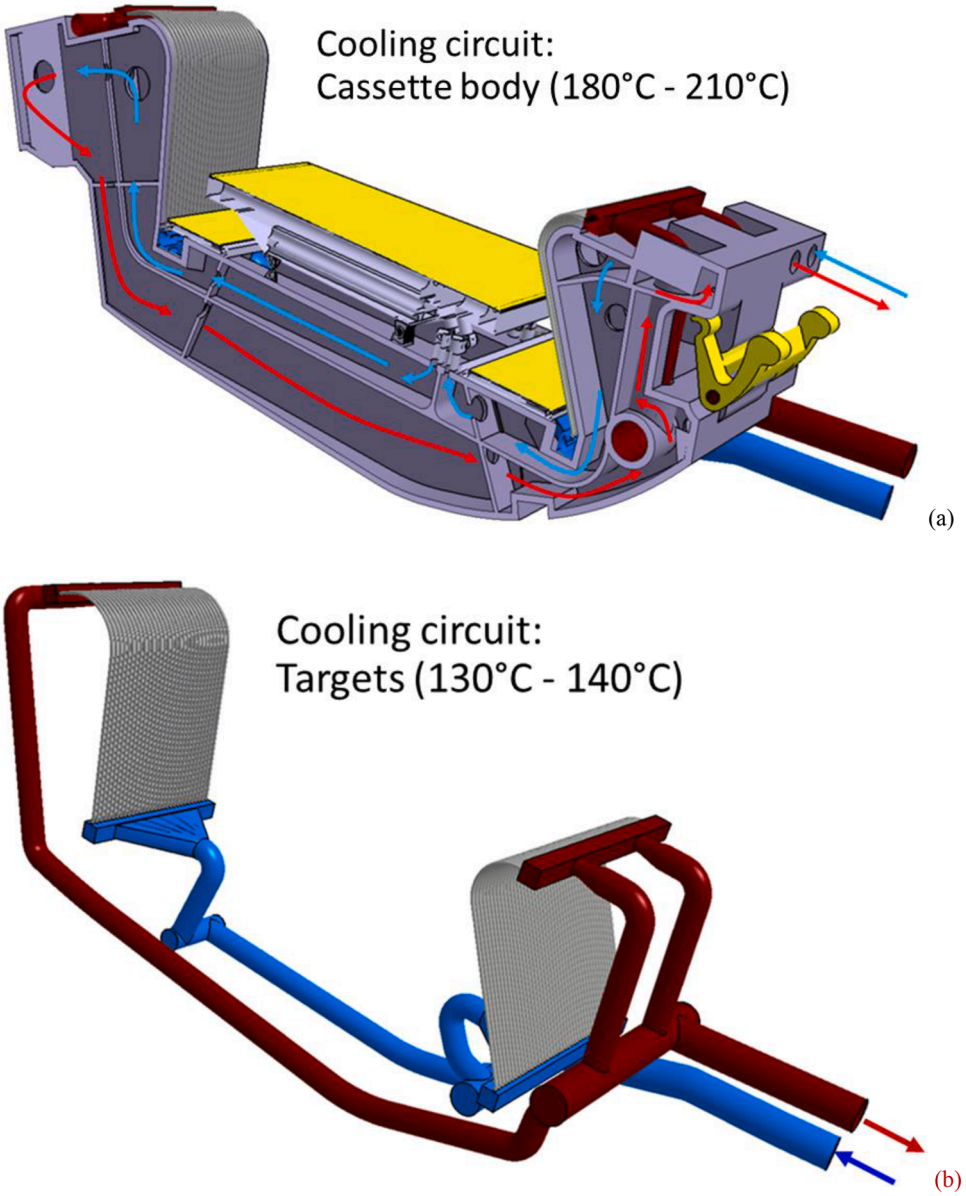

Fig. 22. Two cooling circuits of the baseline dual cooling scheme (a: cassette body, b: targets).

credible material data is a major issue.

The temperature hot spots (555 °C) appear in the supporting legs of the RPs. The SL and the baffle apex experience high temperature (450–500 °C) too. The maximum solid body temperature remains below the allowable upper limit temperature (~550 °C) preserving the long-term mechanical stability (≥ 2000 h) [66].

5. Nuclear loads and shielding performance

5.1. Irradiation damage [46]

The use of low-temperature coolant (180–210 °C) for the steel structures poses a strict constraint on the maximum permissible irradiation damage dose. Unfortunately, there is no test data of EUROFER97 steel irradiated at such low temperatures. Based on the toughness data of EUROFER97 irradiated at 300 °C, the maximum allowable damage dose was identified to be 6dpa [64]. The rationale was that the inlet coolant temperature (thus the lowest solid temperature) should be higher than the measured FTTT (~175 °C). As the DBTT of EUROFER97 does not appreciably change when irradiated at the temperature range of 250–350 °C [63], this specification is deemed a pragmatic approach to start with even though the irradiation-test temperature does not exactly match the operation temperatures. Currently, a dedicated irradiation test at 150–200 °C is under planning to ascertain the low-temperature irradiation effects.

Fig. 31 shows the distribution of irradiation damage from a neutronic analysis computed for the steel bodies of the cassette where the damage dose is plotted in the unit of dpa/fpy. The maximum damage (5dpa/fpy) occurs in the heat sink of the SL and the apex of the both baffles. This means that the SL will reach the 6dpa limit already after 1.2fpy, that is earlier than the targeted lifetime of 1.5fpy. The supporting legs of the targets experience high damage (4dpa/fpy) as well. Unfortunately, it seems very difficult to mitigate the irradiation damage in the plasma-facing front regions due to the direct exposure to the intensive neutron flux. A relaxed conservativism of a (fracture mechanics-based) design rule may be needed to justify the required lifetime.

Fig. 32 shows the predicted distribution of the helium concentration produced by nuclear transmutation. Helium tends to cluster forming stable gaseous bubbles segregating at the grain boundaries at elevated temperatures. High helium concentration has a critical impact on the

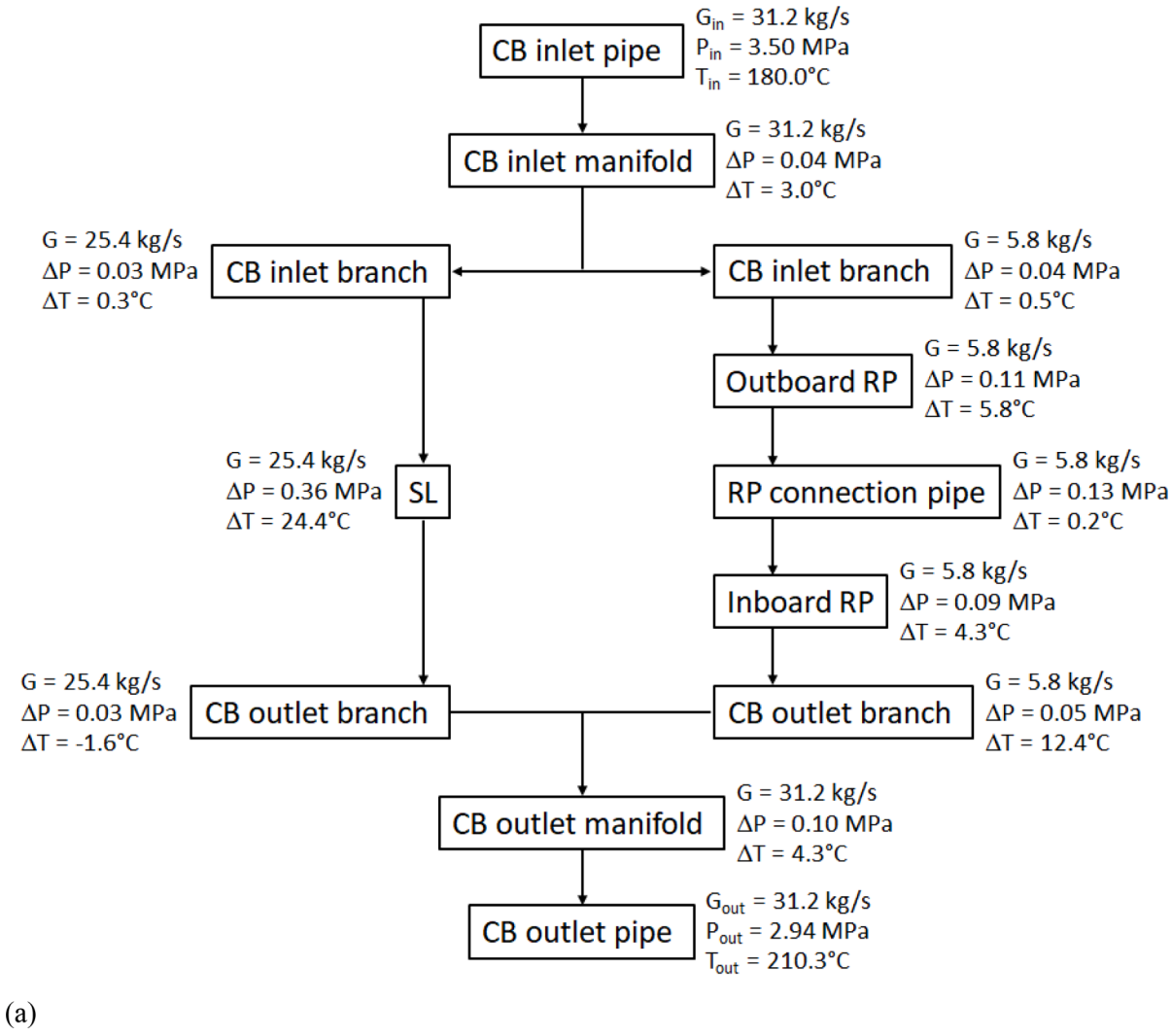

Fig. 23. Schematic flowchart of the cooling circuits (a: cassette body, b: targets).

weldability of steels, a critical issue for the cutting/rewelding of the feeding/exhaust pipes during a remote maintenance. For the irradiated feeding/exhaust pipes (AISI 316 L(N)-IG or EUROFER97), the 1appm (atomic parts per million)-limit was specified. The rear part of these pipes behind the CB (denoted in blue in Fig. 32) meets this criterion.

On the contrary, the red region where helium concentration reaches 100appm allows neither recycling nor cutting/rewelding. It is believed that the stable helium gas bubbles can be removed only by melting (annealing is not feasible).

The nuclear loads in the targets are of critical importance for the lifetime as well. Fig. 33 shows the distribution of the damage dose in the tungsten amour of the IVT, OVT and the SL in the unit of dpa/fpy. The damage dose of the tungsten armor reaches the maximum at the upper baffle regions (1.9dpa/fpy) and decreases gradually towards the strike point (1dpa/fpy). The armor of the SL experiences the same damage dose (1dpa/fpy). The helium concentration in the tungsten amour is modest (1.4appm/fpy) [67].

The damage dose in the copper alloy cooling pipe reaches up to 7dpa/fpy (end-of-life dose: 10.5dpa) [68]. This damage regime is currently not covered by the ITER materials properties handbook. However, considering the pronounced mechanical saturation behavior of CuCrZr alloy irradiated and tested at low temperature (150 °C) already after a low irradiation dose (≤ 0.6dpa) [69], it was tentatively assumed that the key mechanical behavior of irradiated CuCrZr alloy would not significantly change at least up to 10dpa. The helium production rate in the copper cooling pipe reaches up to 58appm/fpy, which is substantial. The high helium concentration could cause considerable embrittlement even at elevated temperatures (≥ 250 °C) due to segregation of helium bubbles at the grain boundaries. The same issue applies to the copper interlayer [60,70].

5.2. *Nuclear shielding performance [46]*

As nuclear shielding for the VV is one of the key functions of the divertor, the shielding performance must be carefully assessed. For the VV (AISI 316L(N)-IG steel), the maximum allowable nuclear load was specified in terms of the "negligible irradiation damage dose limit" as defined in RCC-MRx (A3.3S.33) [71]. According to this criterion, the irradiation damage dose should not exceed 2.75dpa at the end of the service life (6fpy). The negligible damage dose limit is based on the premise that the loss of ductility or toughness due to irradiation should be less than 30%. This means that the fracture energy (J_{Ic}) decreases from 500 kJ/m^2 to 350 kJ/m^2 for the irradiation temperature range of 20–375 °C at 2.75dpa.

Fig. 34 shows the distribution of the irradiation damage dose in the bottom region of the VV after 6fpy. The nuclear loads on the VV is due to neutron leaking through the gap between the SL and the CB. The damage hot spot is located directly below the CB pumping duct. The maximum

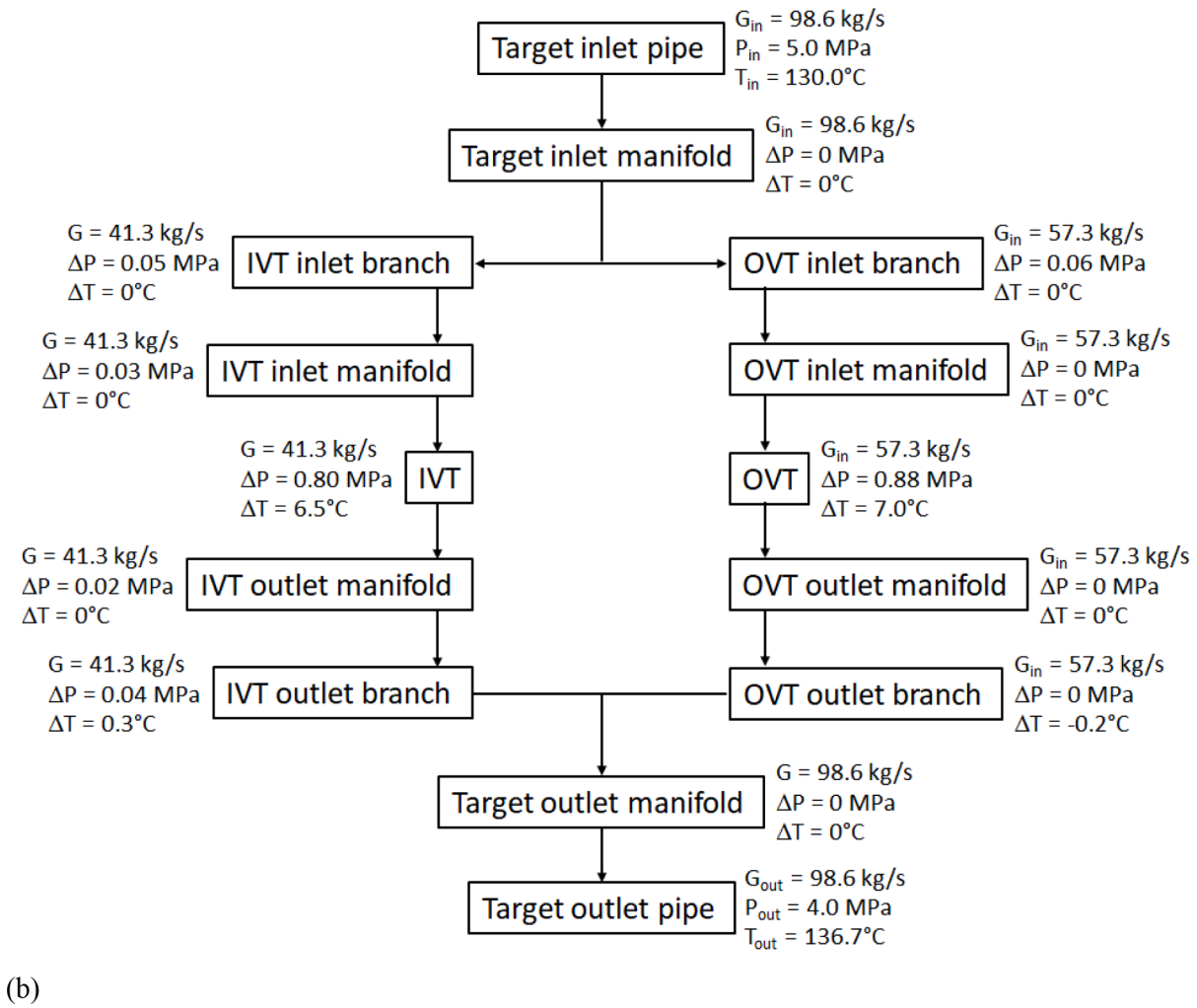

(b)

Fig. 23. (*continued*).

Table 6
Hydraulic parameters of the coolant defined for the targets.

Mass flow rate per cassette	~99 kg/s
Coolant temperature (inlet)	130 °C
Coolant pressure (inlet)	5MPa
Temperature rise (outlet)	+6 °C
Margin to the critical heat flux	>40%
Pressure drop (outlet)	<1MPa
Velocity (OVT)	13–15 m/s
Pumping power per cassette	~100 kW

Table 7
Hydraulic parameters of the coolant defined for the cassette body, shielding liner and reflectors.

Thermal power per cassette	4.2MW
Mass flow rate per cassette	31.2 kg/s
Coolant pressure (inlet)	3.5 MPa
Pressure drop (outlet)	<0.6 MPa
Coolant temperature (inlet)	180 °C
Temperature rise (outlet)	30 °C
Margin to the saturation temp. (outlet)	22 °C
Local max. temp. of coolant (bulk)	230 °C
Local max. temp. of solid (steel)	555 °C
Pumping power per cassette	20 kW

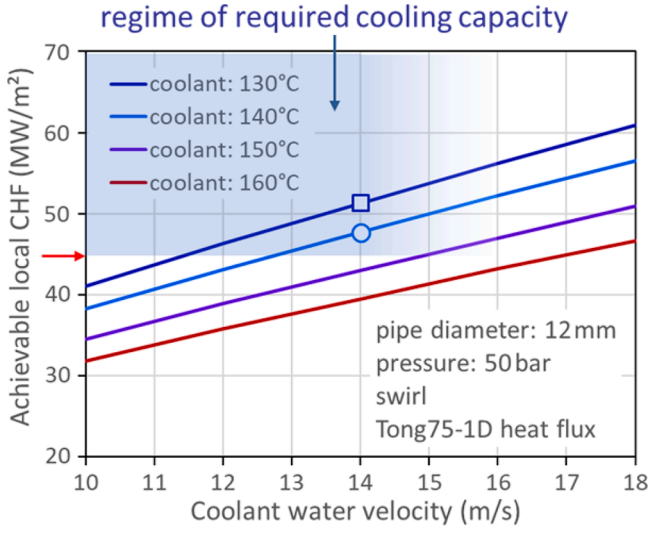

Fig. 24. Relationship between the local heat removal capacity at the inner wall of the (swirled) cooling pipe (inner diameter: 12 mm), coolant velocity and the coolant bulk temperature. [56].

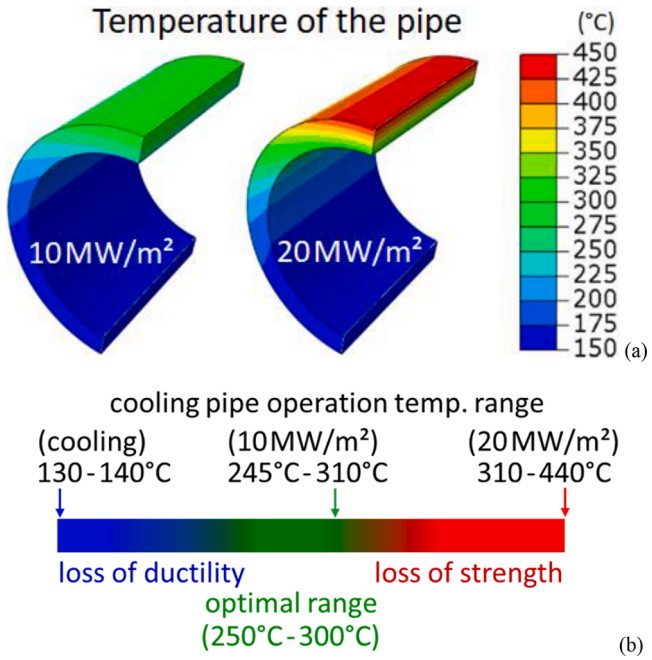

Fig. 25. Equilibrium temperature distribution in the cooling pipe of the target under two representative thermal load cases at the strike point (a), predicted operation temperature range of the cooling pipe under HHF loads up to 20MW/m^2 (b) [60].

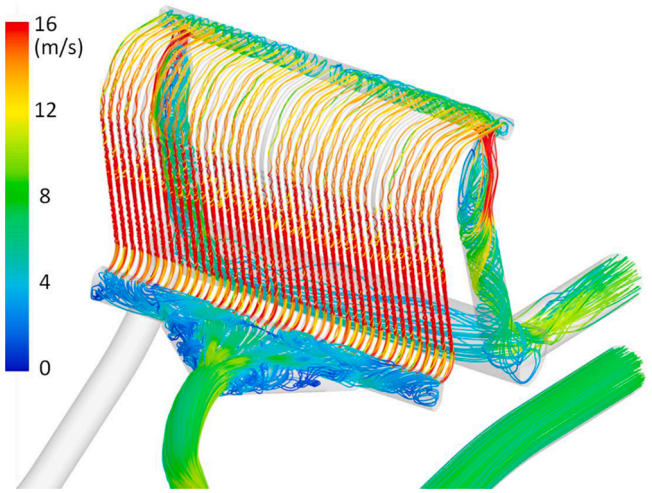

Fig. 26. Coolant stream lines and axial velocity field in the OVT.

value of the damage dose reaches 1dpa, which is significantly lower than the specified criterion. This damage dose can be further reduced if a few beam-like (water-cooled) shielding inserts are introduced in the pumping duct in order to block neutron streaming (see Fig. 35) [33]. With these inserts the VV lifetime can be extended up to 30fpy (≤2.5dpa/30fpy). The nuclear shielding for the magnets is primarily dictated by the geometrical configuration of the lower ports and the port shielding strategy while the divertor design per se only has a limited impact. Currently, the peak nuclear heating power at the hot spots in the TF coils amounts to 150 W/m^3 (allowed limit: ≤50 W/m^3) [23].

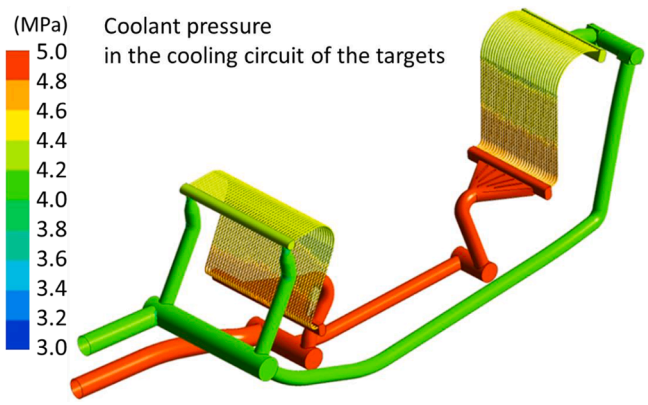

Fig. 27. Pressure field of the coolant in the target cooling circuit.

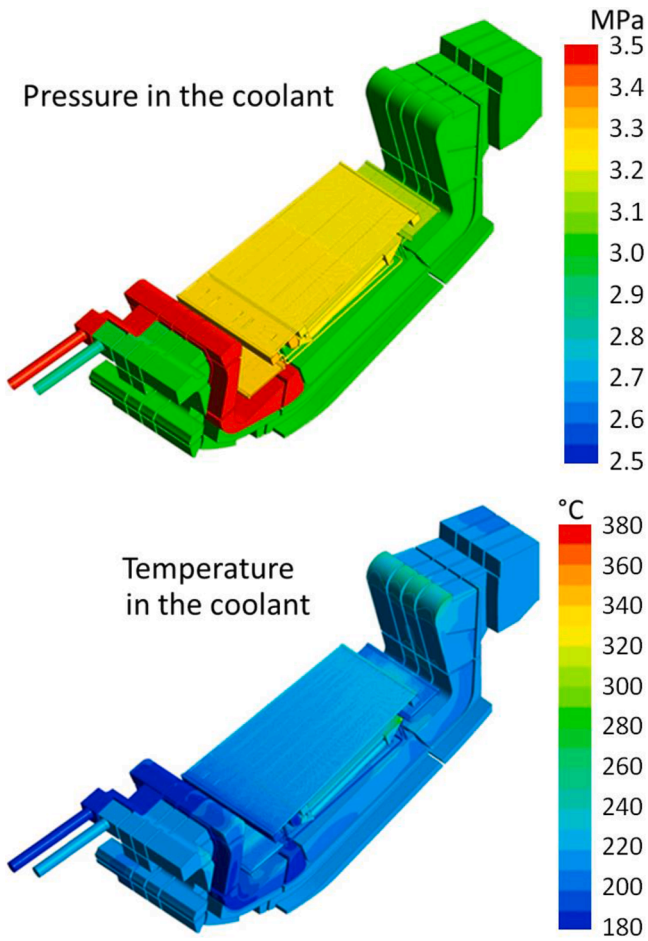

Fig. 28. Pressure and temperature field of the coolant in the cassette body, shielding liner and the reflector plates.

6. Structure-mechanical performance

6.1. Structural integrity assessment: challenges and approaches

The structure-mechanical performance of the divertor can be evaluated in terms of diverse failure criteria for various operational loading conditions. Comprehensive structural integrity assessment studies were carried out to support the design activities. In the absence of a DEMO Design equivalent of the ITER SDC-IC [72] (yet to be developed within the program), the structural design rules (elastic/elasto-plastic,

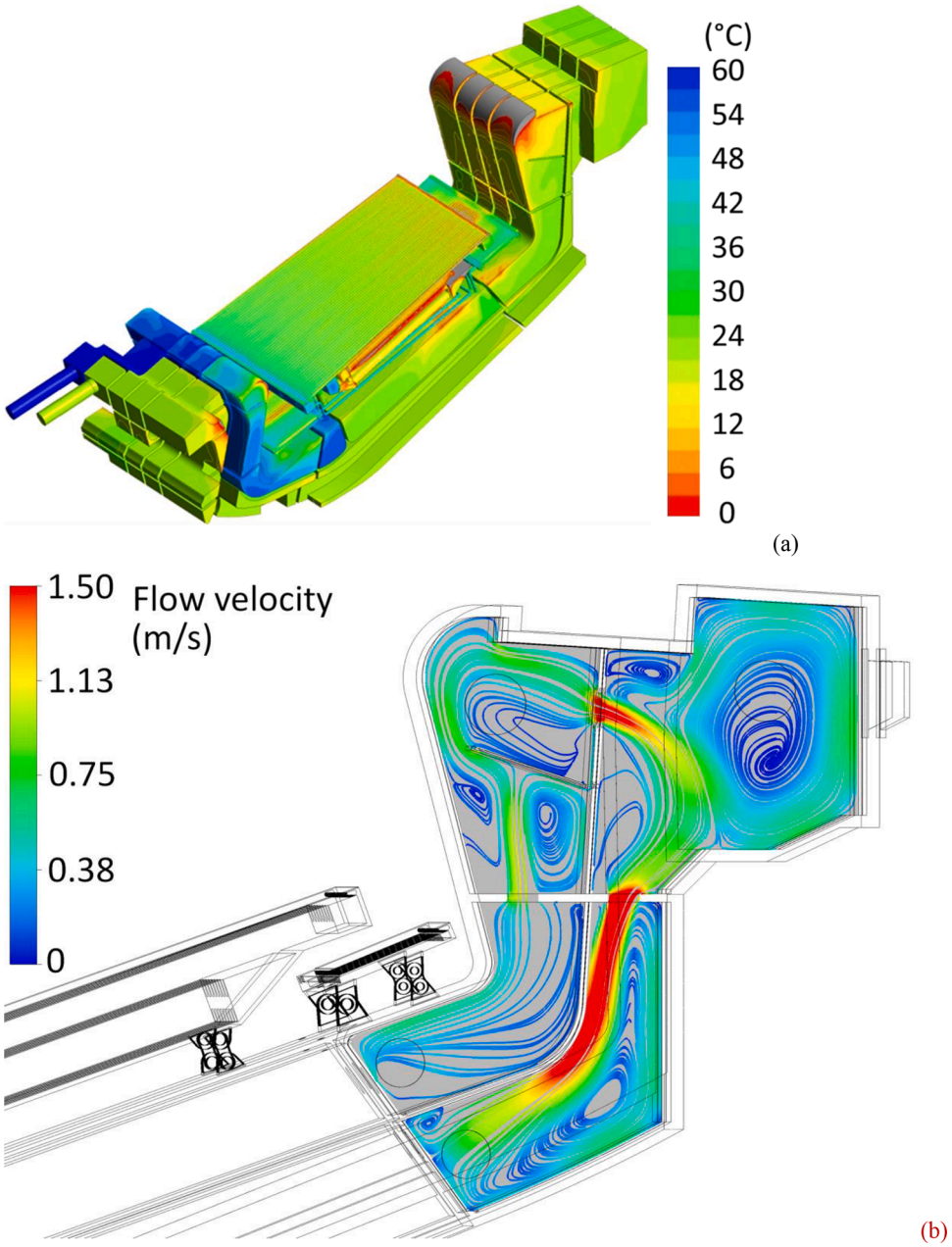

Fig. 29. (a) Distribution of the margin ($\Delta T_{s\text{-}c} = T_s\text{-}T_c$) between the local coolant temperature T_c and the local saturation temperature T_s in the coolant domain (the regions of negative $\Delta T_{s\text{-}c}$ are indicated in gray), (b) 2D cut section view of the CB inboard wing depicting the coolant streamlines and the velocity field.

monotonic/cyclic) of RCC-MRx code (AFCEN ed.) were applied for the steel structures (CB, SL) [73–76].

For the targets, however, there is no well-established design rule. The monoblock-type joined structure consisting of dissimilar materials each with a very different yield stress poses a particular difficulty for defining failure criteria. Moreover, combined loads, cyclic variation of loads, temperature fluctuation and sporadic transient overloads bring additional computational and theoretical complexity. The limited availability of (irradiated) materials data is another hurdle.

Although it was not within the scope of WPDIV to deal with all these non-trivial issues, a pragmatic working strategy had to be elaborated so that the design study could be commenced on a rational basis. Our approach was to implement a staged procedure which could enable a design-by-analysis practice as a complementary tool to support design-by-experiment. The procedure comprises following steps:

(1) Creation of standard guidelines for stress analysis [77].
(2) Simulation-based modeling of possible or observed failure features [78–80].
(3) Formulation of ad-hoc failure criteria and (interim) design rule tailored for the monoblock design [81–83].
(4) Rule-based structural integrity assessment for design verification [81–85].

In the structural integrity assessment, particular attention was paid to selected potential failure modes which can be caused by either material degradation during long-term operation or stress concentration resulting from geometrical features under loads. The topics of interest are listed below together with a brief summary of the respective study:

1 *Relative criticality of cyclic plasticity, fatigue and fast fracture (normal/off-normal operation)*

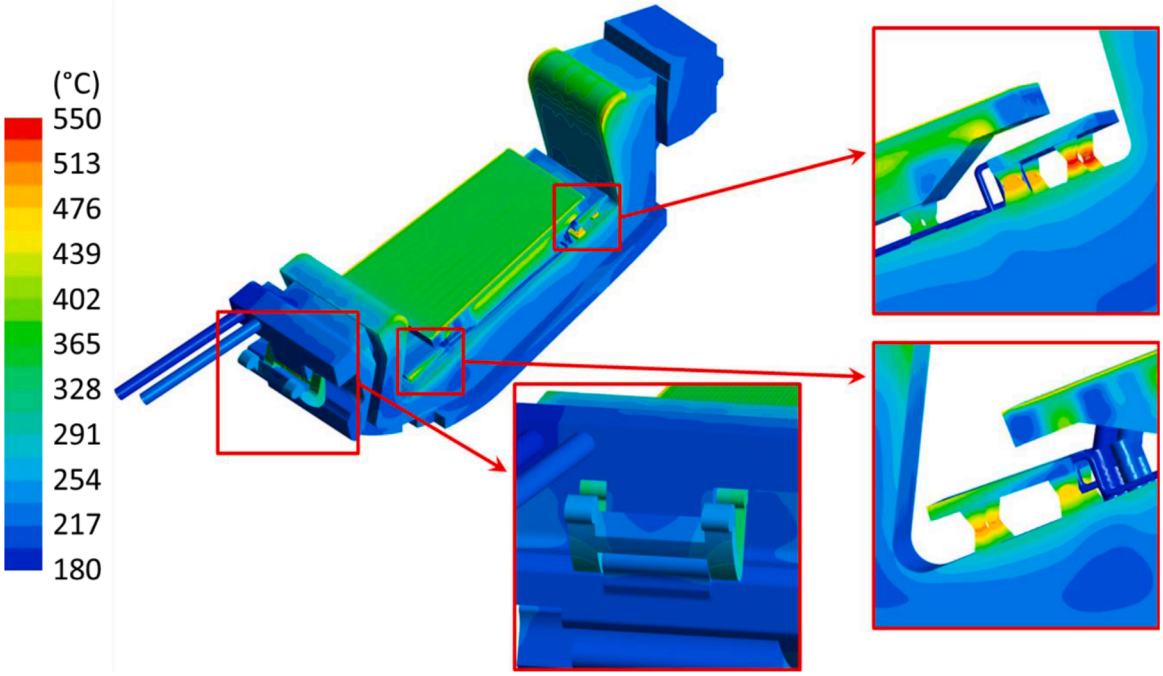

Fig. 30. Equilibrium temperature distribution building up in the solid body (steel) of the cassette.

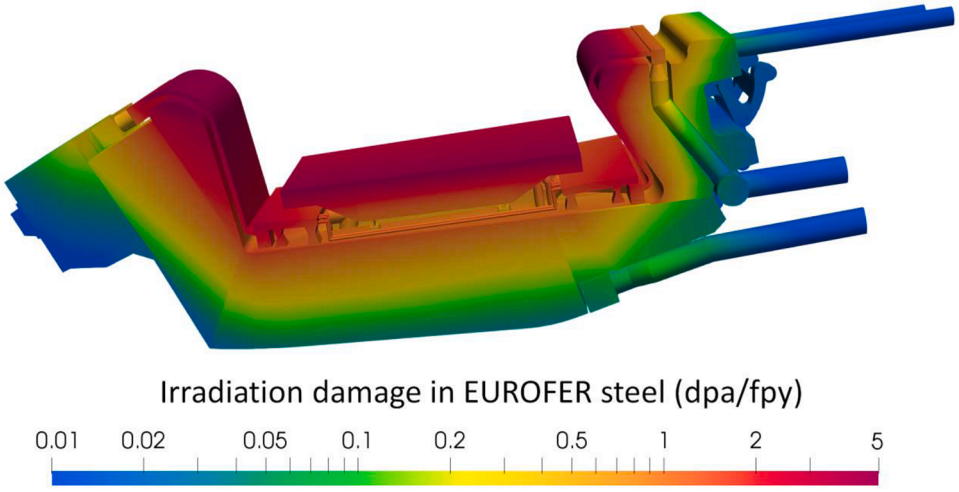

Fig. 31. Distribution of the irradiation damage in the steel components of the cassette (unit: dpa/fpy).

Table 8
Local coolant bulk temperature (T_c), local saturation temperature (T_s) and the margin ($\Delta T_{s\text{-}c}$) at selected positions.

	T_c (°C)	T_s (°C)	$\Delta T_{s\text{-}c}$ (°C)	Δp (MPa)
CB inlet	180.0	242.6	62.6	
Outboard wing outlet	183.0	241.9	58.9	0.04
SL inlet	183.3	241.4	58.1	0.03
SL outlet	207.7	235.2	27.5	0.36
RP inlet	183.4	241.2	57.7	0.04
RP outlet	193.6	235.5	41.9	0.09
Inboard wing inlet	206.1	234.6	28.6	0.05
CB outlet	210.3	232.8	22.5	0.1

Low cycle fatigue (LCF) is not an issue for the armor and the pipe. The armor remains mostly elastic except for the front face layer up to 20MW/m^2 where the softening due to recrystallization hardly leads to a crack initiation. The pipe remains elastic as well owing to elastic shakedown. The reason for shakedown is the presence of initial residual stress produced during the joining process. However, LCF can be a critical issue for the copper interlayer depending on the degree of embrittlement effect (due to helium).

1 *Impact of inelastic stress relaxation during fabrication and operation (Cu, CuCrZr, W)*

See Section 6.4.

1 *Impact of softening due to long-term thermal aging (CuCrZr)*

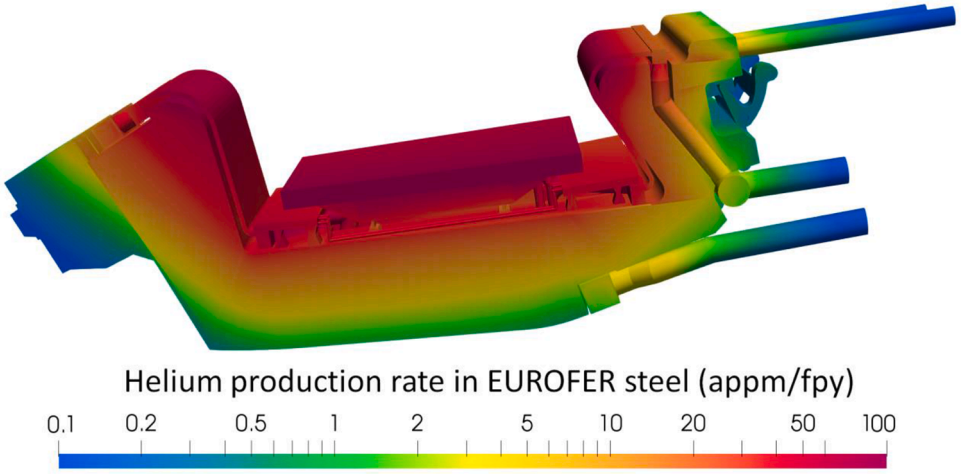

Fig. 32. Distribution of helium concentration produced by nuclear transmutation (unit: appm/fpy).

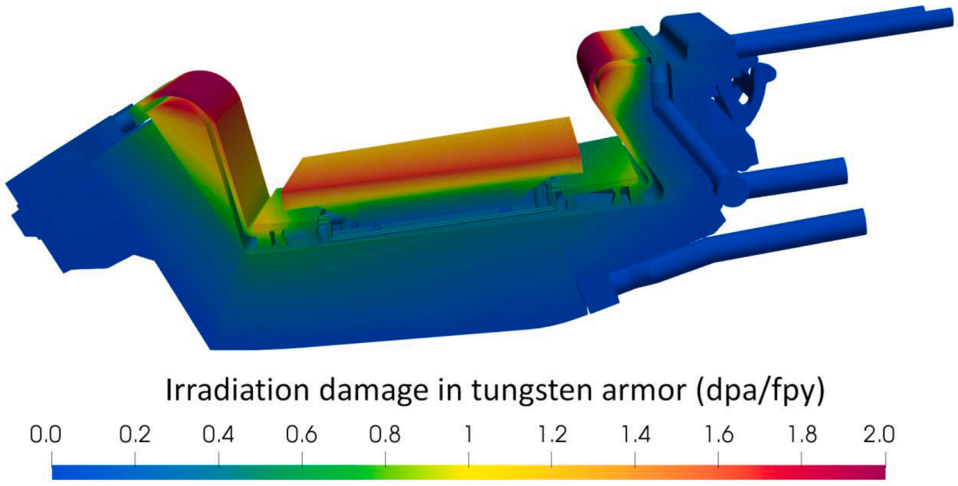

Fig. 33. Distribution of irradiation damage dose in the tungsten amour (unit: dpa/fpy).

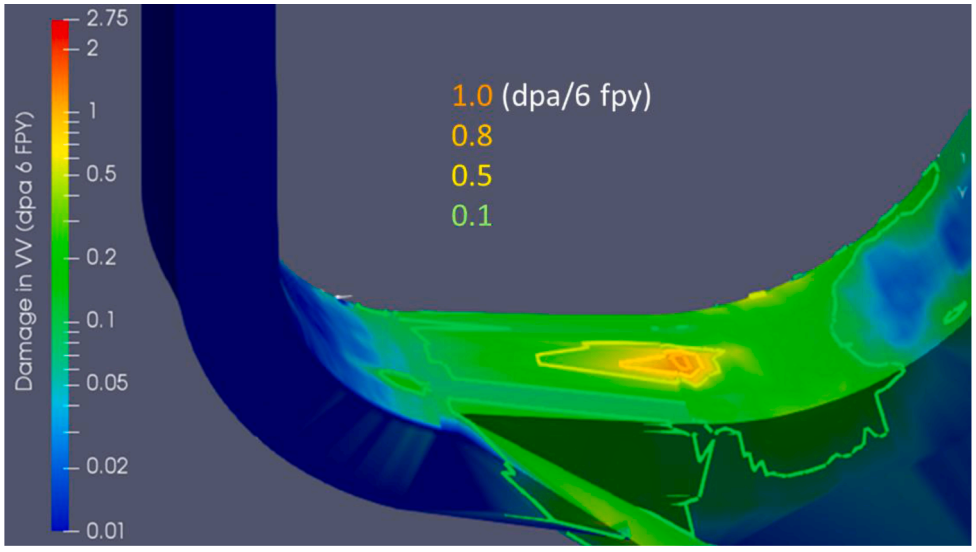

Fig. 34. Distribution of the irradiation damage dose in the bottom region of the VV after 6 fpy.

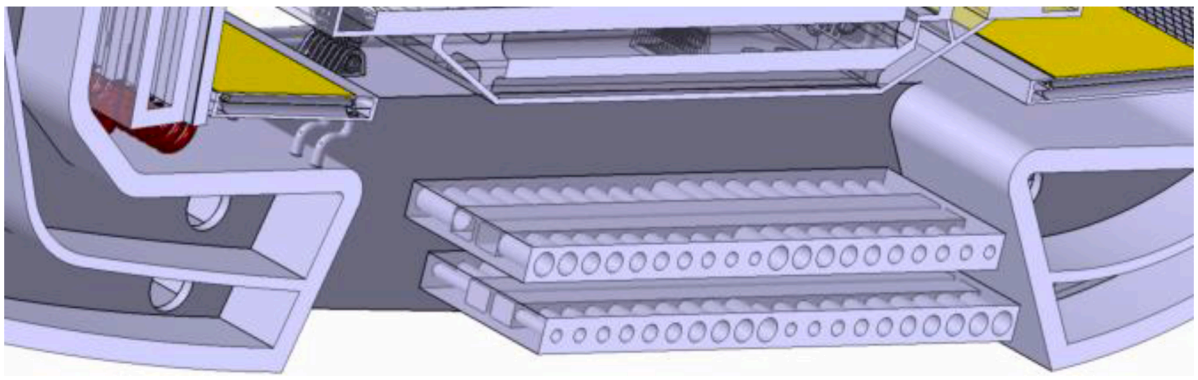

Fig. 35. Water-cooled shielding inserts for reducing nuclear loads on the VV.

Contrary to the intuitive expectation, the substantial softening of the pipe has only a limited impact on the local LCF near the free surface edge of the joining interface to the front face side. The LCF of the pipe bulk is hardly affected by softening.

1 *Impact of irradiation embrittlement and stress tri-axiality (Cu, CuCrZr, W)*

Irradiation embrittlement is not a critical issue for the armor because crack initiation is effectively suppressed by the drastic increase of tensile strength (irradiation hardening) up to 1200 MPa. Even if a crack is initiated, its growth is limited to a subcritical extent even for a very low toughness due to the strain-controlled nature of thermal stresses (stress is relaxed as the strain energy is released by incremental crack extension). On the contrary, the combination of embrittlement and the multi-axial stress state at the pipe edge results in an adverse effect of ductility exhaust posing a critical design concern (see Section 6.6).

1 *Role of the singular stress/strain concentration at the material/geometrical discontinuities*

See Section 6.5.

1 *Impact of local ratchetting on the global structural stability (Cu, CuCrZr)*

The soft interlayer undergoes substantial ratchetting locally at the gap positions due to plastic strain concentration. The cumulative plastic straining will become less pronounced if copper is embrittled by irradiation (due to helium). The local ratchetting in the interlayer gives little impact on the global stability since the armor and the pipe keep their original dimension.

1 *Effect of recrystallization on the fatigue and cracking of the armor (W)*

For the given monoblock dimension adopted for the DEMO divertor, recrystallization and abnormal grain growth in the tungsten armor does not represent any detrimental impact on the material integrity. This is an empirical finding with a high statistical significance supported by the numerous HHF tests.

6.2. *Mechanical response of the cassette [44]*

During normal operation, the cassette experiences a pressure load (by pressurized coolant) and thermal load (by nuclear heating and radiation), which produces primary and secondary stresses, respectively. If a disruption occurs, the resulting electromagnetic force produces additional stress in the supports. These stresses could impair the mechanical integrity or eventually cause a structural failure if their intensity exceeds the specified critical limit. For a quantitative judgement on the risk of a potential failure mode, a proper calculation of stress fields is mandatory.

Fig. 36 shows the distribution of the equivalent (von Mises) stress in the CB and SL calculated for the thermal load (left) and the combined loads (right) assuming elasto-plastic behavior. The combined loads comprise thermal load, static load (coolant pressure) and electromagnetic (EM) impact load induced by a plasma disruption such as vertical displacement event (VDE). It is seen that the resultant stress field under the combined loads is primarily due to the thermal stress field to a decisive degree while the static stress due to the coolant pressure has only a minor influence. The stress level (< 250 MPa) in the CB remains within the elastic regime whereas considerable stresses are produced in the SL. In a structural integrity assessment based on the elastic rules of RCC-MRx code, the fixing support of the SL was identified to be the most critical part due to relatively high temperature (~400 °C) and the resulting thermal softening of EUROFER97 [76].

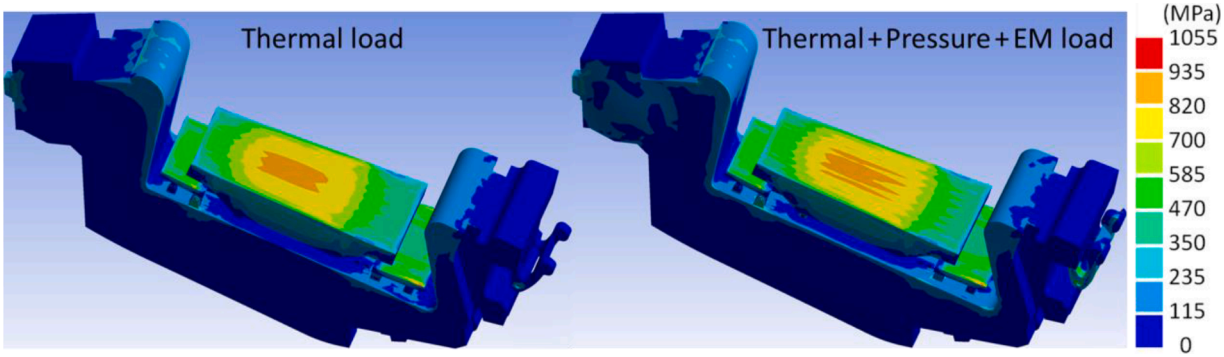

Fig. 36. Distribution of the equivalent (von Mises) stress in the CB and SL calculated for the thermal load and the combined loads (thermal, pressure and electromagnetic force) assuming the elasto-plastic material behavior.

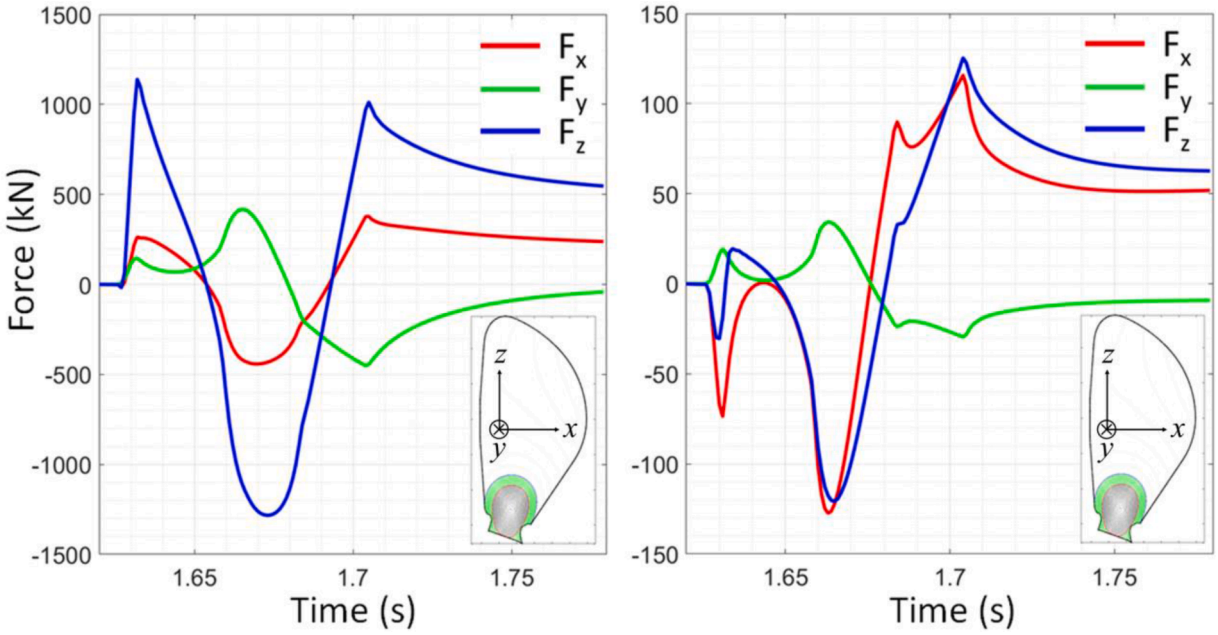

Fig. 37. Time-history of the Lorentz forces induced in the whole divertor (left) and in the whole target cooling circuit system (right) under a downward plasma vertical displacement event (1.67 s after the onset of the instability) [86].

A (linear-elastic) fracture mechanical assessment for the most critical position of a typical SL channel wall showed that even a relatively large crack (elliptical crack having a size of one-quarter depth of the ligament) remained fully subcritical under HHF load cycles at 20MW/m^2.

The radial displacement of the CB due to thermal expansion amounts to 8.4 mm at the engaged outboard wishbone support (cf.: 10.1 mm in an unconstrained state). The thermal stress produced in the wishbone by this thermal deformation amounts to locally up to 610 MPa. However, this maximum stress is still lower than the yield stress of the titanium alloy applied for the wishbone.

6.3. *Selected critical issues: electromagnetic impact loads [86]*

In what follows, a few selected critical issues are highlighted.

The first case is the severe dynamic impact loads acting on the supports and the cooling pipework during a global plasma instability, e.g. disruption or VDEs. This electromagnetic impact load is caused by the volumetric Lorentz force generated by the interaction between the total magnetic field (static plus excited) and the huge electric currents induced/injected in the conductive solid bodies as a consequence of the instability. The total eddy current (estimated to be 20MA) is the sum of the currents induced by the disruption in the entire conducting structures in the toroidal direction. Conversely, the halo current is injected in the poloidal direction assuming that the halo currents are distributed axi-symmetrically (i.e. no toroidal peaking factor). In accordance with the VDE evolution, the halo currents are injected into the upper components of the divertor (SL, IVT/OVT) and into the lower parts of the blanket and the VV.

Fig. 37 shows the transient time-history of the Lorentz force components resulting from a downward VDE. The forces were calculated assuming conducting supports of the targets and the CB to the VV. Owing to the fast transient process (current quench: 74 ms, initiation of the eddy/halo current: 1.63 s/1.66 s) and the tremendous currents induced (total eddy current: 20MA, total halo current: 28kA), very acute and strong forces (cassette: ≤1.3MN, pipework: ≤130 kN) and moments (cassette: ≤3.2MN·m, pipework: ≤ 315kN·m) are generated. The dynamic amplification of the initial loads by inertia effect must be taken into account. The impact loads can be drastically reduced if the supports between the cooling pipes and the VV are insulated (by 70%) or if the supports between the targets and the CB are insulated (by 96%). If the target fixation supports are insulated (using a ceramic barrier), the Lorentz forces are moderately reduced for the CB (e.g., F_z: from 1283 kN to 1201 kN) whereas a drastic decrease is predicted for the target cooling circuit system (e.g., F_z: from 125 kN to 6 kN).

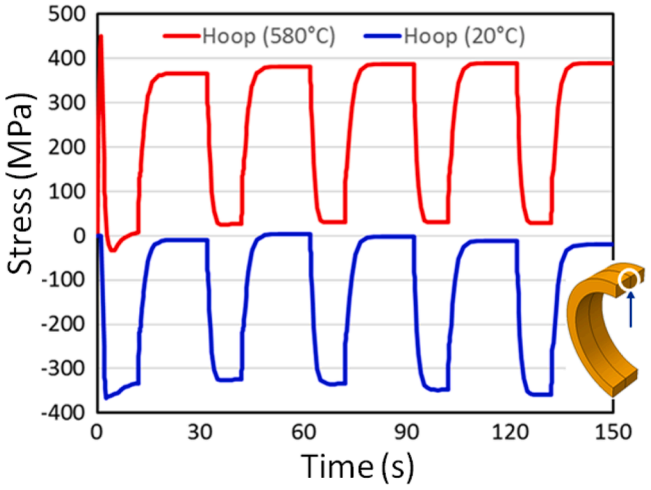

Fig. 38. Stress variation at the front side target cooling pipe (hoop stress in the cylindrical coordinate system) during the cyclic HHF loading (20MW/m^2) after fabrication where two different effective stress free temperatures are assumed (red: 580 °C, blue: 20 °C) [60].

6.4. *Selected critical issues: uncertainty of stress states [60]*

The initial stress state is coined as residual stress by the fabrication process. The extent of inelastic stress relaxation experienced thereby by the ductile constituents (copper interlayer and copper alloy cooling pipe) determines the actual residual stress. This process is difficult to simulate as the knowledge on the physical mechanism is limited and the required materials data (e.g. the parameters of primary creep) are often not available. As a consequence, it is very difficult to specify the effective

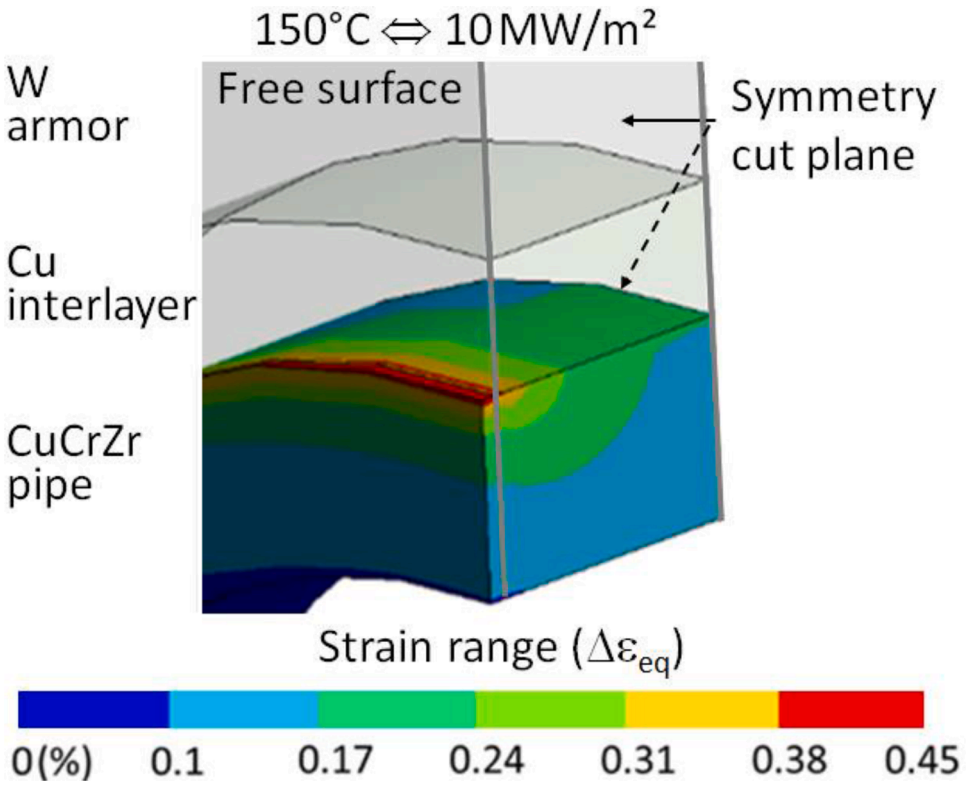

Fig. 39. Calculated strain range intensity in the upper part of the irradiated cooling pipe during a typical HHF loading cycle from cooling (150 °C) to heating at 10MW/m^2 [83].

stress free temperature needed for stress calculation as reference (null strain) temperature. The effective stress free temperature has a decisive impact on stress calculation and failure modeling as manifested in Fig. 38.

Fig. 38 shows the stress variation at the front side target cooling pipe (hoop component in the cylindrical coordinate system) during a typical cyclic HHF loading (20MW/m^2). The entire stress range moves from a compressive to tensile regime preserving the amplitude when the stress free temperature is shifted from 20 °C to 580 °C (joining temperature). Such a complete reversion of the stress sign will likely lead to a different failure behavior. Also the temporal offset between the cyclic phase of stress and temperature is dictated by the assumed stress free temperature. This response clearly indicates the direct impact of effective stress free temperature on the resulting residual stresses. To clarify this issue, a direct measurement of the residual stress was attempted by means of neutron diffractometry. This experimental tool enables calibration of the actual effective stress free temperature by fitting the computed stress profiles with measured ones. The diffraction data revealed that a substantial stress relaxation indeed occurred during fabrication [87]. A similar stress relaxation can also occur under the subsequent HHF loading as a consequence of creep or thermal aging.

6.5. *Selected critical issues: local damage concentration [60,82,83]*

The singular stress/strain concentration appearing at a material interface (particularly, at the free surface edge) is a characteristic feature of the monoblock-type targets and can be a critical issue. Fig. 39 shows the distribution of the strain range intensity (of the equivalent strain) in the upper part of the irradiated cooling pipe (~10dpa) during a typical HHF loading cycle (heating: 10MW/m^2, cooling: 150 °C) in a normal operation. It is seen that the intensity of strain range is locally concentrated at the gap root between two neighboring tungsten blocks. This singular strain concentration can facilitate premature initiation of a fatigue crack. The number of loading cycles up to a crack initiation was

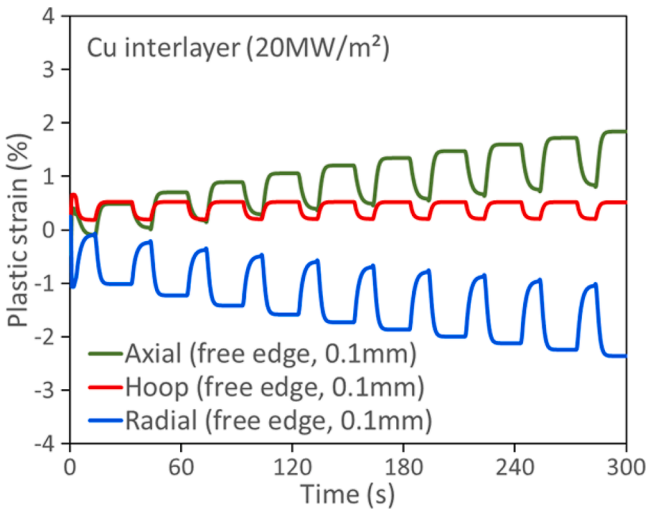

Fig. 40. Variation of the principal plastic strain components (cylindrical coordinate system) at the free edge of the copper interlayer at 0.1 mm below the armor over the first 10 HHF cycles at 20MW/m^2 [60].

assessed to be 1915. However, it is not clear whether this crack (if initiated at all) would really further grow beyond the localized strain concentration region. Given that the crack is under a strain-controlled load (thermal stress is produced by differential thermal strains which are necessarily bounded), crack tip stress will be readily relaxed upon incremental crack growth. Therefore, the term "number of cycles to fatigue failure" may need to be redefined more specifically, for instance, referring to either local (acceptable) or global (unacceptable) failure taking into account the load carrying capacity. Otherwise, a failure assessment dominated by the singular strain range will be burdened by

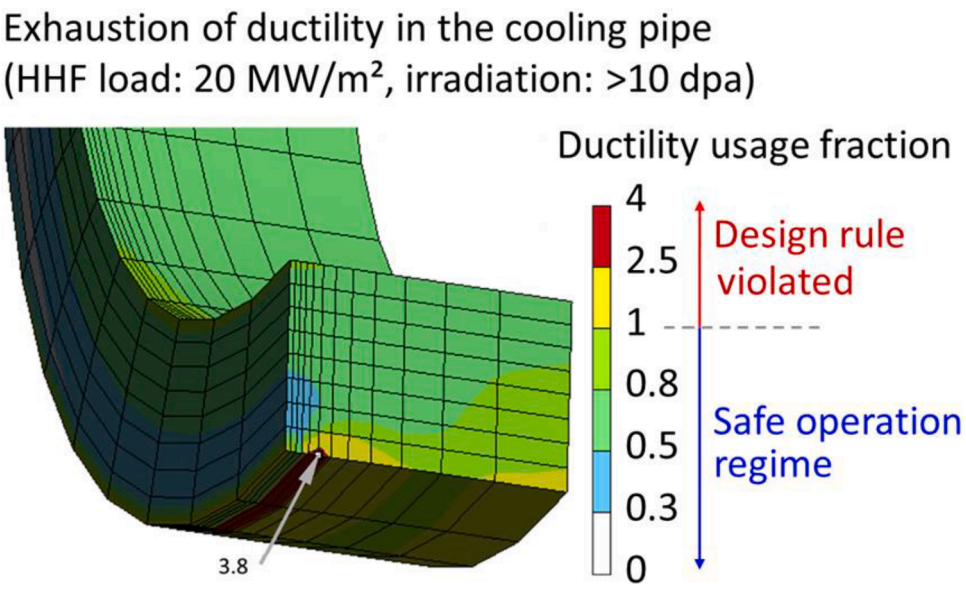

Fig. 41. Ductility usage fraction in the lower part of the cooling pipe calculated for the HHF loading cycle at 20MW/m^2 (cooling: 150 °C) [83].

an overly conservative criterion. It is noted that the maximum strain range of 0.45% is only a moderate increase from the unirradiated case (0.4%) [83].

An analogous issue applies to the copper interlayer. Fig. 40 illustrates the cyclic variation of the principal plastic strain components (cylindrical coordinate system) at the free edge of the copper interlayer at 0.1 mm below the armor over the first 10 loading pulses at 20MW/m^2 (no embrittlement was assumed). This interfacial free edge position represents a critical region of singular strain (and stress) concentration. It is seen that not only the magnitude but also the amplitude of strain variation increases with the number of HHF pulses. This response indicates a cumulative low cycle fatigue damage likely resulting in a crack initiation. However, similarly to the cooling pipe case discussed above, it is not clear whether this fatigue crack would continue to grow beyond the strain concentration region. Copper could be hardened and embrittled if transmutation gas bubbles (e.g. helium) are segregated at grain boundaries [70]. This effect will counteract the plastic straining impeding the accumulation of fatigue damage. Thus, prediction of a plastic fatigue lifetime is still subject to an uncertainty with regard to irradiation effects.

6.6. *Selected critical issues: exhaustion of ductility by irradiation [83]*

Fig. 41 shows the ductility usage fraction in the lower part of the cooling pipe calculated for a HHF loading cycle at 20MW/m^2. The ductility usage fraction is defined as the ratio of the incremental strain used per each loading cycle to the limit strain estimated at each position based on the ultimate rupture strain, temperature, stress tri-axiality, irradiation dose (10dpa) and safety factor (e.g. 2). The normalized usage fraction values higher than unity means that the criterion is violated. Fig. 41 reveals that the usage fraction exceeds unity in the extensive region of the bottom area (critical hot spots: > 3). This alarming result is attributed to the combined effect of embrittlement due to low-temperature irradiation (≤ 150 °C) and the pronounced stress tri-axiality near the free edge of the bond interface. This failure risk presents a serious design concern (the criticality depends on code rules used). A fracture mechanics-based brittle failure criteria could be applied for handling the affected region. The quite high toughness of irradiated CuCrZr alloy seems to justify the design against fast fracture but needs further scrutiny.

On the other hand, the pronounced irradiation hardening of the initially ductile cooling pipe can have a beneficial effect against either plastic fatigue by decreasing the plastic strain range or stress intensity-based failures (S_m or $3S_m$) by increasing yield stress. In this sense, irradiation effects are ambivalent [88].

Table 9
Selected characteristics of the European DEMO divertor contrasted with the ITER divertor [7, 8, 89-92].

	DEMO divertor	ITER divertor
Structural materials	CB: EUROFER97 steel IVT/OVT: CuCrZr-IG alloy SL: EUROFER97 steel	CB: SS 316 L(N)-IG/ XM-19 IVT/OVT: CuCrZr-IG alloy Dome: CuCrZr-IG alloy
Max. irradiation dose (dpa/ fpy)	CB: 1 (target supports: 4) SL (EUROFER97): 5 OVT: 2 (W), 7 (Cu)	CB: 0.1 Dome (Cu heat sink): 3.5 OVT: ≤0.5 (W), ≤2 (Cu)
Bulk nuclear heating (MW)	~134	~102
SOL conduction heat (MW)	~220 (incl. radiative dissipation)	~100 (D-T burning)
Inlet temperature (water)	CB: 180 °C OVT: 130 °C	CB: 70/100 °C VT: ≤140 °C (nominal)
He production (appm/fpy)	SL (EUROFER97): 94 CB (EUROFER97): 49 OVT (Cu heat sink): 57	Dome (Cu heat sink): 31 CB (316 L(N)): 2.5 OVT (Cu heat sink): 13
Peak heat flux (MW/m^2)	Steady state: 10 (2 h) Slow transient: 20 (10 s)	Steady state: 10 (400 s) Slow transient: 20 (10 s)
Transient events (assumed scenarios)	ELM: suppressed or mitigated Disruptions: tbd.	ELM: suppressed or mitigated Disruptions: 25 times
Lifetime (cycles/fpy)	6600 (+ overhead)/1.5	3000/0.1

7. Technology

7.1. *Technology issues and R&D topics*

It is relevant to raise the question as to whether and to what extent the up-to-date ITER technologies are applicable or can be extrapolated for the DEMO divertor. To assess this question, the materials and the loading conditions specific for the divertors of the DEMO and ITER need to be compared. In Table 9, selected characteristics of the DEMO divertor are contrasted with the ITER divertor [7,8,89–92].

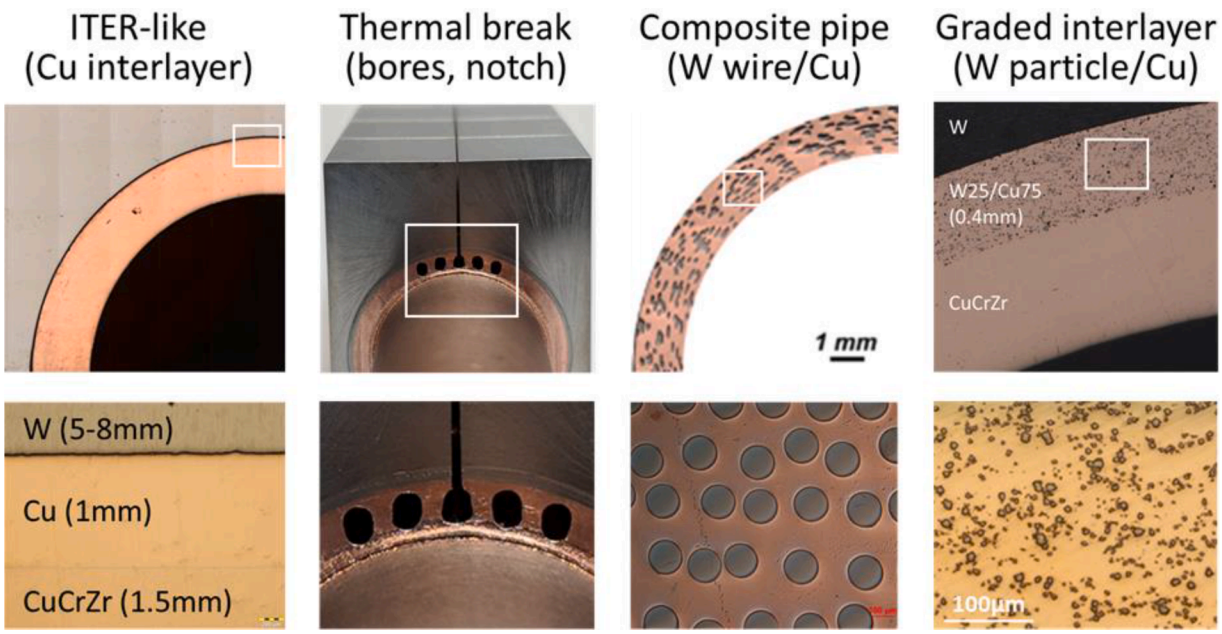

Fig. 42. Four selected monoblock-type design variants developed for the targets (fltr: ITER-like, thermal break, composite pipe, graded interlayer design concept).

Table 9 suggests that the technologies of the ITER divertor (except for the targets) will not be applicable to the DEMO divertor because the main structural materials are essentially different from each other (austenitic vs. ferritic-martensitic steel). Moreover, the DEMO divertor is subject to much higher nuclear loads. This difference poses serious challenges with regard to design as well as technology.

Currently, the following topics are identified as major R&D objectives:

- Joining technologies for steel components (HIP, welding) and pipes of dissimilar materials (brazing).
- Alternative manufacturing technologies for CB (additive manufacturing using selective laser melting).
- Manufacturing of medium-scale target mock-ups with the wire-reinforced composite pipe.
- Coating of thick tungsten armor on a large steel plate (for SL).
- Anti-corrosion coating and corrosion-erosion test of the cooling pipe [93,94].
- Coating for electrical insulation of the target supports.
- Full-scale fabrication and hydraulic verification of the whole target pipework.

In the PCD Phase, the R&D efforts were focused on the HHF technology whereas the R&D of the other subcomponents were shifted to the Concept Design (CD) Phase. This decision was mainly due to the facts that the design had not yet been fully detailed and very limited resources were available. As a consequence, in the baseline design, the aspect of overall technology feasibility was addressed only at a rudimentary level. In 2021, a comprehensive technology R&D program was launched for the entire cassette aiming at industrial manufacturability.

7.2. *HHF technology and performance [43,95]*

In the PCD, the approach was to take the HHF technology developed for ITER as working reference to take advantage of its maturity and availability, and to pursue evolutionary innovations for enhancing

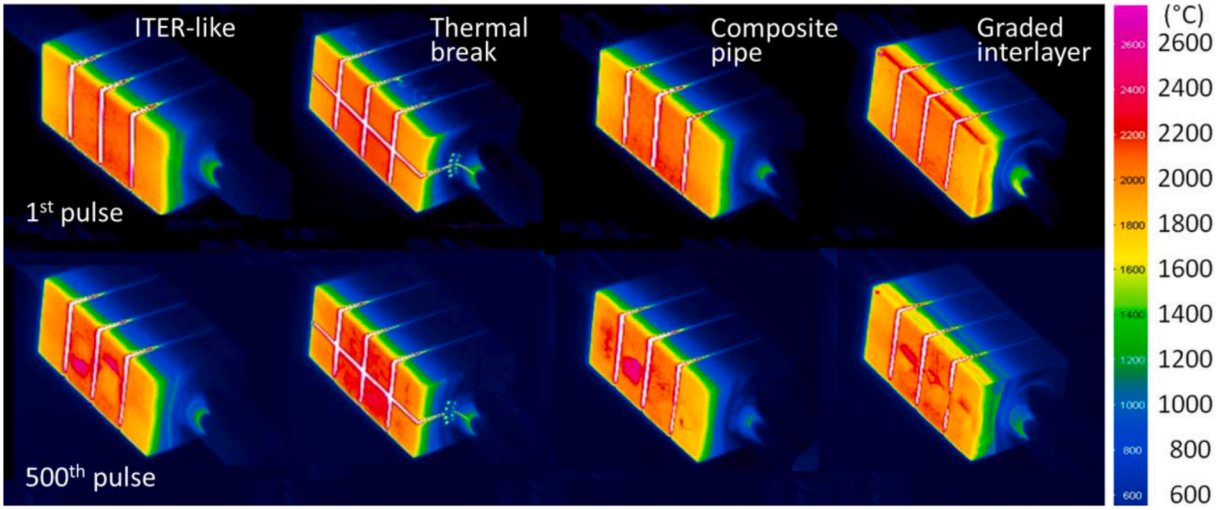

Fig. 43. *In-situ* infrared thermography (false color) images of the various monoblock-type target mock-ups (depicted in Fig. 42) under cyclic HHF loads at 20MW/m^2 up to 500 pulses (coolant: 130 °C) [43].

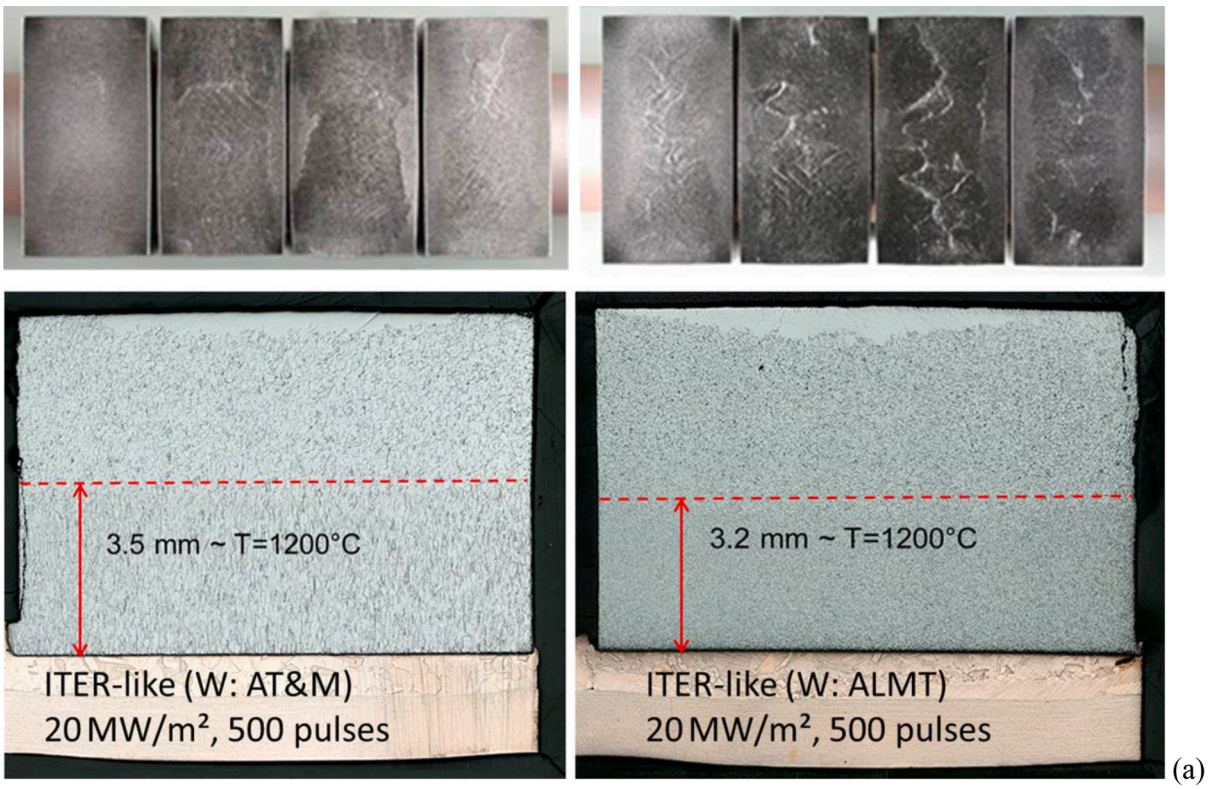

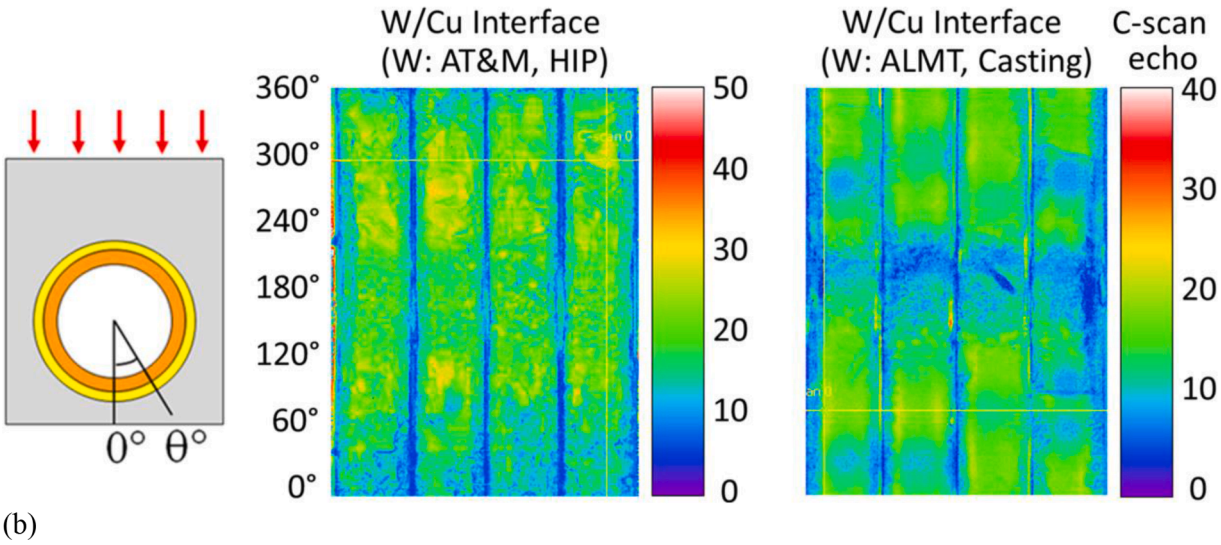

Fig. 44. (a) Metallographic sections (axial cut) of the HHF-tested (20MW/m^2, 500 pulses) ITER-like mock-ups with the tungsten blocks produced by AT&M (left) and ALMT (right), respectively, together with the photographs of the armor front faces, (b, c) ultrasonic inspection images of the same mock-ups.

performances. The R&D program comprised concept studies (monoblock with a thermal break, flat-tile), novel materials (composite pipe, composite block, graded interlayer) and joining (hot radial pressing, hot isostatic pressing, brazing) [84,85,96–109]. All design variants were realized in form of a small-scale mock-up with the standard geometry and evaluated in an extensive and systematic HHF testing campaign using hydrogen neutral beam (20–25MW/m^2, 500–1000 pulses, 20–130 °C coolant) and non-destructive test inspection tools [110–116]. Selected examples of the design concepts are presented in Fig. 42.

The four monoblock-type variants (ITER-like, thermal break, composite pipe, graded interlayer) passed the qualification tests without any discernable indication of failure or deteriorated hear removal capacity. Moreover, the ITER-like baseline technology (joined by hot radial pressing) and the monoblock design with the tungsten wire-reinforced copper composite pipe (joined by brazing) showed an excellent HHF performance without any structural failure (albeit with armor surface damages) or indication of affected heat removal capacity even at 25MW/m^2 at least up to 500 pulses (coolant: 20 °C). A stable heat removal performance without failure was demonstrated up to 32MW/m^2 (5 pulses) which was the physical limit nearly reaching the

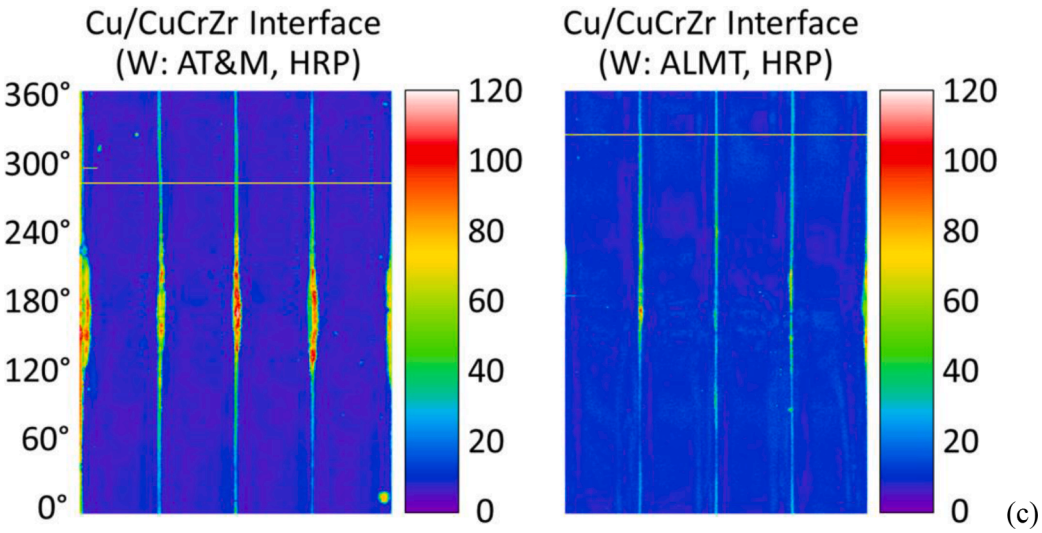

Fig. 44. (*continued*).

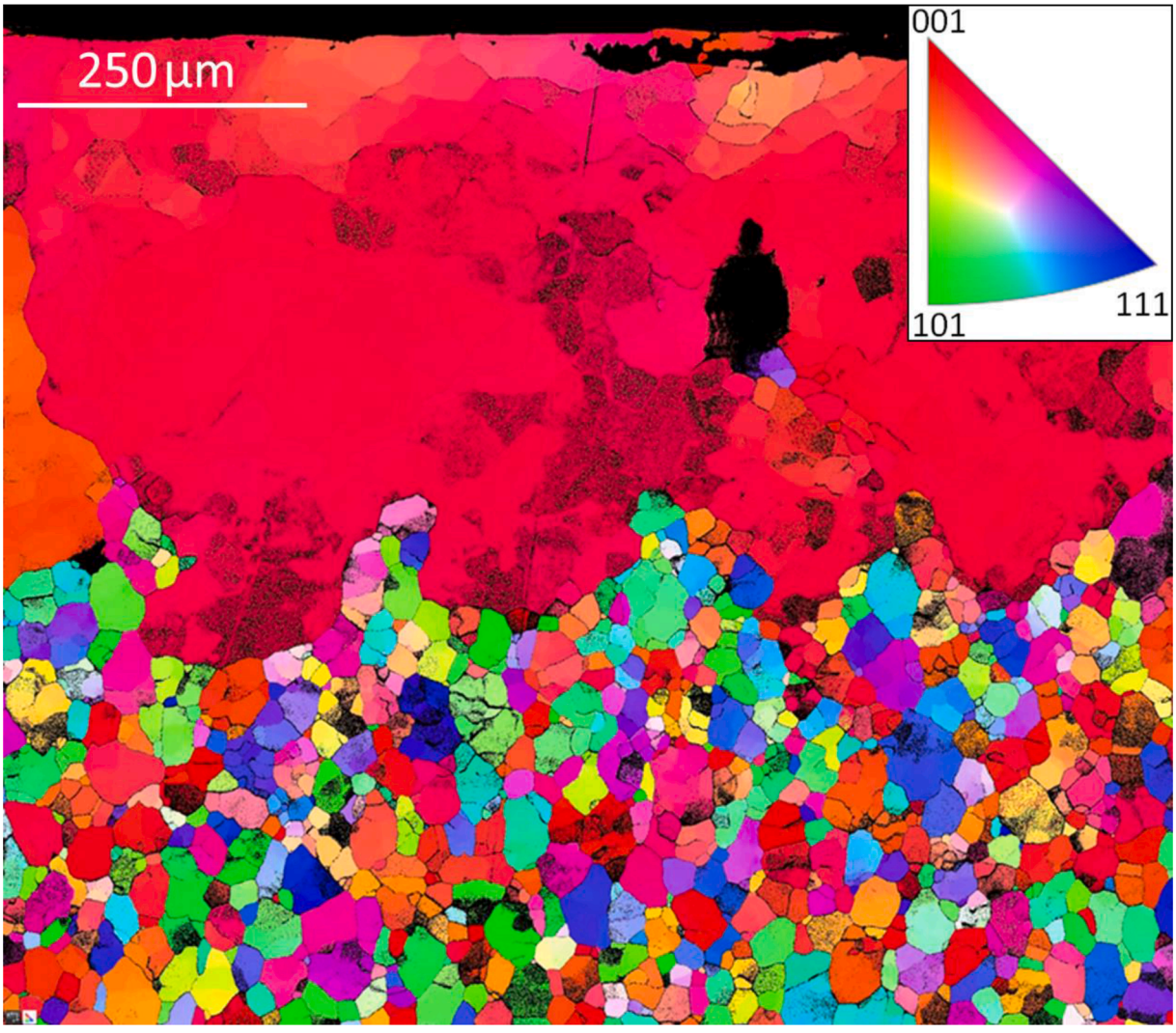

Fig. 45. EBSD crystal orientation map of the ALMT tungsten armor scanned for the front face region (axial cut section).

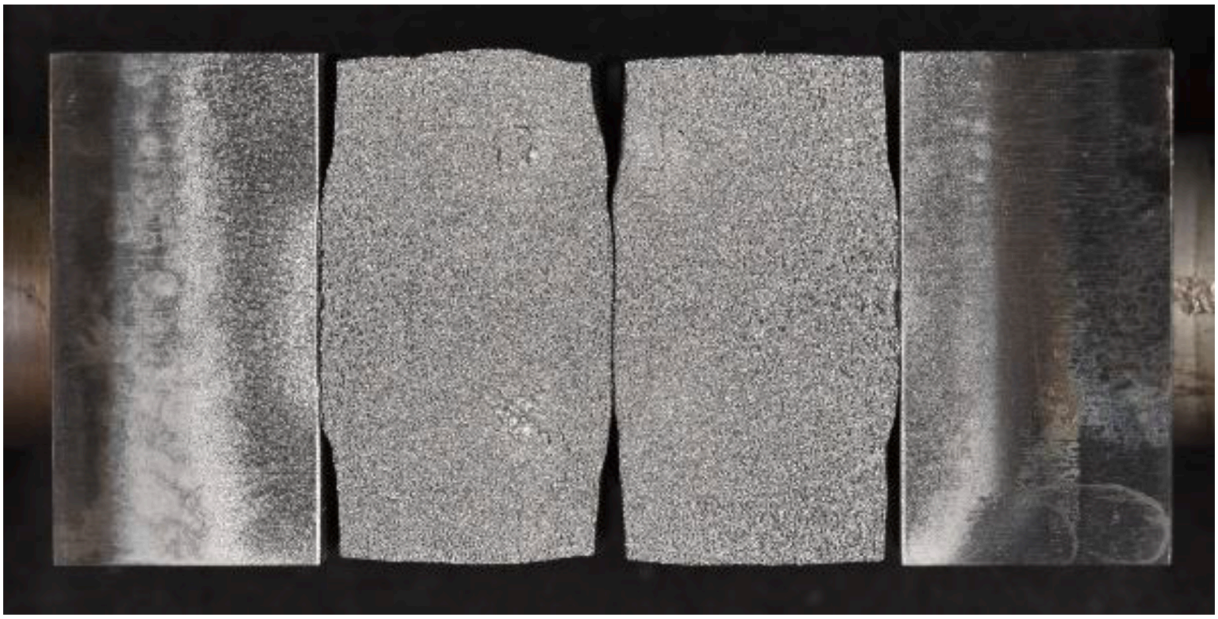

Fig. 46. Front face picture of an ITER-like W monoblock target mock-up after a HHF test at 20MW/m^2 after 2000 electron beam pulses (HADES facility).

melting temperature of tungsten at the front face. The findings of the HHF tests are statistically significant as supported by the large number of testing cases (290 monoblocks). Details of the technology R&D and the results of the HHF qualification tests are found elsewhere [43,95].

Fig. 43 shows the *in-situ* infrared (IR) thermography images captured for the four target mock-ups under cyclic HHF loads at 20MW/m^2 up to 500 pulses (coolant: 130 °C). The surface temperature distributions are compared between the first and the last pulse. The compared images display no significant change of temperature over the entire loading cycles indicating a sound structural integrity (note that the modest changes in color shading are due to the changing surface emissivity).

Fig. 44(a) shows the metallographic sections (axial cut) of two HHF-tested (20MW/m^2, 500 pulses) ITER-like target mock-ups each with the tungsten blocks produced by AT&M (left) or ALMT (right) [43]. The photographs of the armor front faces loaded are also shown. Both micrographs reveal abnormal growth of recrystallized grains near the front face, but no single crack is seen on the cut sections as well as on the front faces. The ultrasonic inspection images (360 °C-scan of reflected echo) presented in Fig. 44(b) also confirm intact joining (except for the minor edge cracks in the AT&M blocks). The ITER-like and composite pipe monoblock mock-ups remained fully intact up to 1000 pulses at 20MW/m^2.

In Fig. 44(a), a microstructural change near the front face is seen in both tungsten materials. Fig. 45 shows the EBSD crystal orientation map of the ALMT tungsten armor scanned for the front face region (axial cut section). The EBSD image clearly reveals fully recrystallized grains and abnormal grain growth in the front face layer. An extensive EBSD scanning confirmed that the whole front face layer (~1 mm depth) fully underwent abnormal grain growth leaving only a few big grains. The upper half of the armor (~4 mm depth) was completely recrystallized. This picture indicates that recrystallization or grain growth per se is not necessarily a cause of crack initiation.

The HHF fatigue testing at 20MW/m^2 was extended up to 1000 pulses (neutral H beam) and up to 2000 pulses (electron beam), respectively, to explore the performance limit of the ITER-like target mock-ups. In both loading cases, the mock-ups withstood the tests remaining intact without any indication of detrimental damage or failure (see Fig. 46).

Fig. 47(a) shows the front face photograph of the armor blocks (ITER-like target mock-up with AT&M tungsten) after 500 pulses at 25MW/m^2 and the laser profilometry image of a selected block revealing the topography of surface roughness. The picture exhibits severe surface damage overall on the front face. It looks as if the neighboring armor blocks were nearly fused together. However, the front surface has never been molten because the maximum temperature reached only 2600 °C at the edges, which was far lower than the melting point of tungsten (see Fig. 47(b). The front face damage was produced by cumulative cyclic visco-plastic strains resulting in a swelling deformation. The maximum height of the surface roughening was 600 μm. Such a severe roughening may possibly cause a leading edge loading effect. This mock-up sustained the damage without any structural failure and withstood the HHF pulses fully maintaining the heat removal capacity as evidenced by the IR thermography images in Fig. 47(b). The microscopic images of the metallographic cut sections in Fig. 47(c) confirm the intact structural integrity of the component up to a single thin crack (6 mm) in the armor, which remained fully innocuous. The joining interfaces and the heat sink were not deteriorated at all.

8. Summary and conclusions

In late 2020, the PCD for the European DEMO divertor has been concluded, delivering the baseline design after seven years of joint undertaking in the EUROfusion Consortium. To support the baseline design, comprehensive computational and experimental justifications were also delivered. The essential characteristics of the baseline design are as follows:

- Single-null magnetic configuration.
- Modular cassette design to allow remote maintenance via the lower ports.
- Shielding liner plate in lieu of a dome.
- Minimized baffle area (in favor of increased breeding blanket area).
- Low-temperature water-cooling (OVT: 130 °C, CB: 180 °C) with two separate cooling circuits.
- Reduced-activation (ferritic-martensitic) steel as major structural material.
- Full tungsten targets based on the ITER-like high-heat-flux technology (monoblock-type armor).
- Direct integration of the targets onto the cassette body (no detachable plasma-facing unit).

The major achievements of the PCD are as follows:

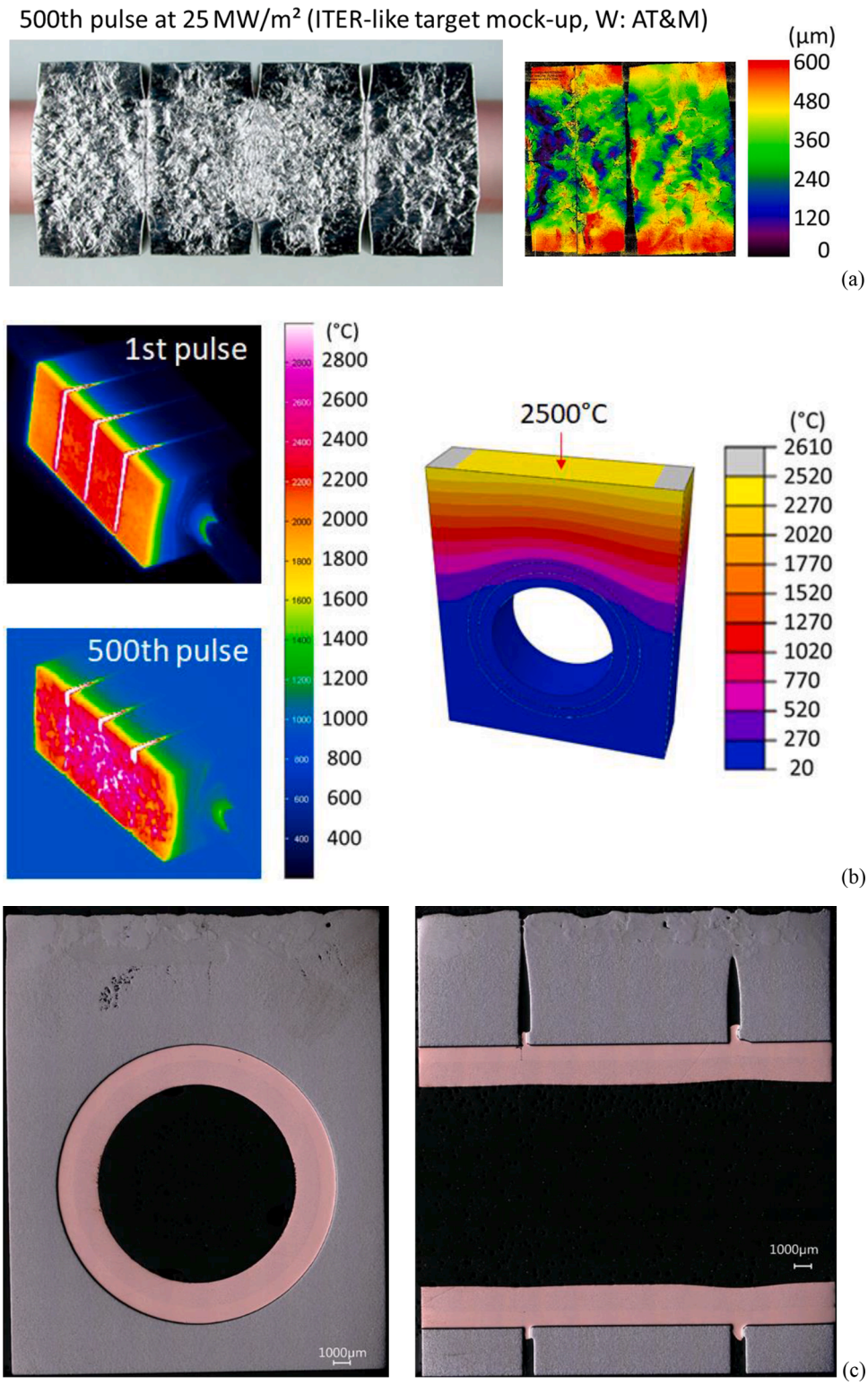

Fig. 47. (a) Photograph of the armor blocks (front face) of the ITER-like target mock-up after 500 HHF pulses at 25MW/m^2 and a laser profilometry image revealing surface roughness, (b) IR thermography images under the HHF test at 25MW/m^2 (cold coolant) and the calculated temperature field (FEM), (c) optical micrographs of the metallographic sections (left: cross cut, right: axial cut).

- Delivery of the feasible (baseline) design concept with a pre-conceptual maturity.
- Verification of the baseline design in terms of cooling, nuclear shielding and structural integrity.
- Formulation of the inelastic structural integrity assessment procedure where guidelines for structural analysis, failure criteria (tailored for the ITER-like target) and case studies are presented.
- Full-scale experimental verification of the hydraulics performance of the target cooling circuit.

- Demonstration of high-quality fabrication and excellent HHF performance of the target technologies.
- Comparative assessment of the reliability and detection limit of nondestructive inspection methods.
- Demonstration of the fit-for-purpose for the neutron diffractometry and tomography imaging of the small-scale target mock-ups for measuring residual stress and for detecting internal defects.
- Qualitative demonstration of the anti-corrosion performance of a protective coating on the pipe wall tested in a water-loop with controlled water chemistry and flow condition.

The key findings and open issues from the PCD are:

- The lifetime of the divertor (1.5fpy) is primarily limited by the irradiation damage of the steel at the nuclear hot spots rather than the armor erosion rate (if ELM is fully suppressed).
- Nuclear transmutation produces a high concentration of helium in the CB and SL, particularly, near the front face ($\leq$140appm after 1.5fpy). The considerable He concentration raises the potential issue of reduced lifetime and limited recyclability of the steel components (stable He bubbles can be removed only by melting).
- Even with the low coolant temperature of the cassette body approaching the acceptable lower limit specified for irradiated EUROFER97 steel, the margin to the critical heat flux is still tight or even locally exhausted (higher pressure is required).
- The state-of-the-art HHF technology based on the tungsten monoblock-type design has demonstrated an excellent heat removal capacity and highly reliable fatigue resistance under the DEMO-relevant HHF loads up to 25MW/m^2 in thermal equilibrium.
- The HHF performance of the monoblock-type target designs seems to fulfill the design requirements from both the thermo-hydraulic and structure-mechanical point of view.
- The front face layer of the plasma-facing components (targets, shielding liner) are directly exposed to intense neutron fluxes experiencing excessive nuclear loads (lattice damage and transmutation).
- The divertor design comprises many complex geometrical entities featuring numerous discontinuities and joints. These discontinuities and joining interfaces (e.g. weld seam, brazes, diffusion bonds) tend to act as stress concentrators susceptible to irradiation embrittlement and prone to cracking.
- The structural reliability of the steel structures could not be fully assessed because required materials data from relevant irradiation tests ($T_{irr}\leq$150–200 °C) are missing (will be available in the early Engineering Design Phase).
- Further critical issues are: rationalized design of supports for straightforward on-site remote handling, precision production for keeping fabrication allowance, resilience for contingency (e.g. disruption).

9. Outlook

In the CD Phase (2021–2027), the main focus of the project efforts shall be placed on:

1 An alternative design concept for the cassette which allows easier remote handling (particularly, to enable on-site replacement of the PFCs) and reduced maintenance downtime (via a reduced number of the feeding pipes). To this end, a fully revised design with a single cooling circuit and a simplified target attachment design will be elaborated.
2 Rigorous structure-mechanical assessment to ensure the structural integrity and reliability of the steel structures to be irradiated below the DBTT. For supporting this, a dedicated modeling methodology and proper failure criteria with a balanced conservativism shall be formulated.
3 Launching of the preliminary technology R&D program to explore industrial manufacturability of the major steel structures and ancillary components (pipework, supports, armor, etc.).
4 Further maturation of HHF technology with innovative technical approaches (e.g. joining, composite cooling pipe, anti-corrosion coating, etc.) including medium-scale prototype fabrication and HHF verification.

CRediT authorship contribution statement

J.H. You: Conceptualization, Methodology, Supervision, Writing – original draft, Writing – review & editing, Project administration, Funding acquisition. **G. Mazzone:** Conceptualization, Methodology, Supervision. **E. Visca:** Methodology, Supervision. **H. Greuner:** Methodology, Investigation. **M. Fursdon:** Methodology, Investigation. **Y. Addab:** Methodology, Investigation. **C. Bachmann:** Conceptualization. **T. Barrett:** Conceptualization, Methodology, Investigation. **U. Bonavolontà:** Methodology, Investigation. **B. Böswirth:** Investigation. **F.M. Castrovinci:** Investigation. **C. Carelli:** Methodology, Investigation. **D. Coccorese:** Investigation. **R. Coppola:** Methodology, Investigation. **F. Crescenzi:** Investigation. **G. Di Gironimo:** Methodology. **P.A. Di Maio:** Conceptualization, Methodology, Investigation. **G. Di Mambro:** Investigation. **F. Domptail:** Methodology, Investigation. **D. Dongiovanni:** Methodology, Investigation. **G. Dose:** Methodology, Investigation. **D. Flammini:** Methodology, Investigation. **L. Forest:** Methodology, Investigation. **P. Frosi:** Methodology, Investigation. **F. Gallay:** Methodology, Investigation. **B.E. Ghidersa:** Conceptualization, Methodology, Investigation. **C. Harrington:** Methodology, Investigation. **K. Hunger:** Investigation. **V. Imbriani:** Methodology, Investigation. **M. Li:** Methodology, Investigation. **A. Lukenskas:** Methodology, Investigation. **A. Maffucci:** Methodology, Investigation. **N. Mantel:** Methodology, Investigation. **D. Marzullo:** Conceptualization, Investigation. **T. Minniti:** Methodology, Investigation. **A.V. Müller:** Methodology, Investigation. **S. Noce:** Methodology, Investigation. **M.T. Porfiri:** Methodology, Investigation. **A. Quartararo:** Methodology, Investigation. **M. Richou:** Conceptualization, Methodology, Investigation. **S. Roccella:** Methodology, Investigation. **D. Terentyev:** Methodology, Investigation. **A. Tincani:** Methodology, Investigation. **E. Vallone:** Investigation. **S. Ventre:** Investigation. **R. Villari:** Methodology, Investigation. **F. Villone:** Investigation. **C. Vorpahl:** Investigation. **K. Zhang:** Methodology, Investigation.

Declaration of Competing Interest

The authors declare that they have no known competing financial interests or personal relationships that could have appeared to influence the work reported in this paper.

Acknowledgement

This work has been carried out within the framework of the EUROfusion Consortium and has received funding from the Euratom research and training program 2014–2018 and 2019–2020 under grant agreement No 633053. The views and opinions expressed herein do not necessarily reflect those of the European Commission.

The authors (particularly, JHY as the Project leader) are very grateful to the WPDIV Design Review Panel (chair: D. Stork, members: A. Cardella, C. Ibbott, R. Tivey) for their valuable recommendations and constructive (and fair) criticisms from their rich experiences. In addition, JHY wants to thank the PPPT department head (G. Federici) and his team for their supports and guidance. Finally, the authors appreciate all the contributions from the previous members of the WPDIV.

References

[1] G. Federici, et al., Overview of the design approach and prioritization of R&D activities towards an EU DEMO, Fusion Eng. Des. 109-111 (2016) 1464–1474.
[2] G. Federici, et al., DEMO design activity in Europe: progress and updates, Fusion Eng. Des. 136 (2018) 729–741.
[3] J.H. You, et al., Conceptual design studies for the European DEMO divertor: rationale and first results, Fusion Eng. Des. 109-111 (2016) 1598–1603.
[4] J.H. You, et al., Progress in the initial design activities for the European DEMO divertor: subproject Cassette, Fusion Eng. Des. 124 (2017) 364–370.
[5] D. Marzullo, et al., Systems engineering approach for pre-conceptual design of DEMO divertor cassette, Fusion Eng. Des. 124 (2017) 649–654.
[6] F. Crescenzi, et al., ITER-like divertor target for DEMO: design study and fabrication test, Fusion Eng. Des. 124 (2017) 432–436.
[7] R. Tivey, et al., ITER divertor, design issues and research and development, Fusion Eng. Des. 46 (1999) 207–220.
[8] A.S. Kukushkin, et al., Divertor issues on ITER and extrapolation to reactors, Fusion Eng. Des. 65 (2003) 355–366.
[9] M. Turnyanskiy, et al., A roadmap to the realization of fusion energy: mission for solution on heat-exhaust systems, Fusion Eng. Des. 96-97 (2015) 361–364.
[10] C. Bachmann, et al., Issues and strategies for DEMO in-vessel component integration, Fusion Eng. Des. 112 (2016) 527–534 (small divertor, no PFU).
[11] G. Federici, et al., European DEMO design strategy and consequences for materials, Nucl. Fusion 57 (2017), 092002.
[12] H. Reimerdes, et al., Assessment of alternative divertor configurations as an exhaust solution for DEMO, Nucl. Fusion 60 (2020), 066030.
[13] G. Federici, et al., Magnetic Confinement Fusion-Technology-Fusion Core, Encyclopedia of Nuclear Energy, Elsevier, 2021, pp. 554–575, https://doi.org/10.1016/B978-0-12-819725-7.00050-7.
[14] U. Bonavolontà, et al., EU-DEMO divertor: cassette design and PFCs integration at pre-conceptual stage, Fusion Eng. Des. 159 (2020), 111784.
[15] G. Mazzone, et al., Eurofusion-DEMO divertor - cassette design and integration, Fusion Eng. Des. 157 (2020), 111656.
[16] J. Wesson, Tokamaks (Oxford Engineering Science Series, 48), 2 Ed., Oxford University Press, 1997. ISBN-10: 0198562934.
[17] N. Asakura, et al., Plasma exhaust and divertor studies in Japan and Europe broader approach, DEMO design activity, Fusion Eng. Des. 136 (2018) 1214–1220.
[18] F. Maviglia, et al., Impact of plasma-wall interaction and exhaust on the EU-DEMO design, Nucl. Mater. Ener. 26 (2021) 100897.
[19] N. Asakura, et al., Power exhaust studies and divertor Designs for Japanese and European DEMO fusion reactors, Nucl. Fusion 61 (2021) 126057.
[20] A. Loarte, et al., Power exhaust in tokamaks and scenario integration issues, Fusion Eng. Des. 122 (2017) 256–273.
[21] J.H. You, et al., Nuclear loads and nuclear shielding performance of EU DEMO divertor: a preliminary neutronics evaluation of two interim design options, Nucl. Mater. Energy 23 (2020), 100745.
[22] C. Day et al., DEMO Tritium fueling and vacuum systems, Fusion Eng. Des., this issue.
[23] C. Gliss, Integrated design of the DEMO lower ports, Eurofusion report 2MSRLH (2020).
[24] I.E. Garkusha, et al., Performance of deformed tungsten under ELM-like plasma exposures in QSPA Kh-50, J. Nucl. Mater. 415 (2011) S65–S69.
[25] G. Federici, et al., Overview of the DEMO staged design approach in Europe, Nucl. Fusion 59 (2019), 066013.
[26] F. Militello, et al., Preliminary analysis of alternative divertors for DEMO, Nucl. Mater. Ener. 26 (2021), 100908.
[27] P. Rindt, et al., Conceptual design of a liquid-metal divertor for the European DEMO, Fusion Eng. Des. 173 (2021) 112812.
[28] M. Zhao, et al., CFD evaluation and optimization of the HEMJ divertor cooling design, Fusion Eng. Des. 158 (2020), 111669.
[29] W. Wen, et al., Heat pipe technology based divertor plasma facing component concept for European DEMO, Fusion Eng. Des. 164 (2021), 112184.
[30] C. Bachmann, Plant Description Document (v. 1.9), Eurofusion report (2021) 2KVWQZ.
[31] F. Cismondi, et al., Progress in EU-DEMO In-Vessel Components integration, Fusion Eng. Des. 124 (2017) 562–566.
[32] T. Pinna, et al., Safety important classification of EU DEMO components, Fusion Eng. Des. 146 (2019) 631–636.
[33] D. Marzullo, et al., Progress in the pre-conceptual CAD engineering of European DEMO divertor cassette, Fusion Eng. Des. 146 (2019) 942–945.
[34] D. Marzullo, EUROfusion Report 2NSLJP: divertor system detailed design description (2020).
[35] M. Rieth et al., EUROFER 97 Tensile, Charpy, Creep and Structural Tests, Forschungszentrum Karlsruhe Wissenschaftliche Berichte FZKA 6911 (2003).
[36] G. Mazzone, et al., Structural verification and manufacturing procedures of the cooling system for DEMO divertor target (OVT), Fusion Eng. Des. 146 (2019) 1610–1614.
[37] V. Imbriani, et al., Insulated fixation system of plasma facing components to the divertor cassette in Eurofusion-DEMO, Fusion Eng. Des. 158 (2020), 111710.
[38] T. Hirai, et al., ITER tungsten divertor design development and qualification program, Fusion Eng. Des. 88 (2013) 1798–1801.
[39] M. Li, et al., Interpretation of the deep cracking phenomenon of tungsten monoblock targets observed in high-heat-flux fatigue tests at 20 MW/m^2, Fusion Eng. Des. 101 (2015) 1–8.
[40] M. Li, et al., Design options to mitigate deep cracking of tungsten armor, Fusion Eng. Des. 124 (2017) 468–472.
[41] M. Li, et al., Structural impact of armor monoblock dimensions on the failure behavior of ITER-type divertor target components: size matters, Fusion Eng. Des. 113 (2016) 162–170.
[42] M. Li, et al., Fracture mechanical analysis of a tungsten monoblock-type plasma-facing component without macroscopic interlayer for high-heat-flux divertor target, Fusion Eng. Des. 122 (2017) 124–130.
[43] J.H. You, et al., High-heat-flux technologies for the European demo divertor targets: state-of-the-art and a review of the latest testing campaign, J. Nucl. Mater. 544 (2021), 152670.
[44] P. Frosi, Loads specification and structural analysis, Eurofusion report 2P8PER (2020).
[45] R.A. Kempf, et al., Correlation between radiation damage and magnetic properties in reactor vessel steels, J. Nucl. Mater. 445 (2014) 57–62.
[46] R. Villari et al., Annex to Loads Specification (LS) for divertor cassette and PFCs: neutronic analysis of DEMO divertor 2019, Eurofusion report 2NL3S8 (2020).
[47] P.A. Di Maio, et al., Thermal-hydraulic study of the DEMO divertor cassette body cooling circuit equipped with a liner and two reflector plates, Fusion Eng. Des. 167 (2021), 112227.
[48] P.A. Di Maio, et al., Computational thermofluid-dynamic analysis of DEMO divertor cassette body cooling circuit, Fusion Eng. Des. 136 (2018) 1588–1592.
[49] P.A. Di Maio, et al., On the thermal-hydraulic optimization of DEMO divertor plasma facing components cooling circuit, Fusion Eng. Des. 136 (2018) 1438–1443.
[50] P.A. Di Maio, et al., Thermal-hydraulic optimisation of the DEMO divertor cassette body cooling circuit equipped with a liner, Fusion Eng. Des. 146 (2019) 220–223.
[51] P.A. Di Maio, et al., Hydraulic analysis of EU-DEMO divertor plasma facing components cooling circuit under nominal operating scenarios, Fusion Eng. Des. 146 (2019) 1764–1768.
[52] P.A. Di Maio, et al., On the thermal-hydraulic performances of the DEMO divertor cassette body cooling circuit equipped with a liner, Fusion Eng. Des. 156 (2020), 111613.
[53] P.A. Di Maio, et al., On the numerical assessment of the thermal-hydraulic operating map of the DEMO divertor plasma facing components cooling circuit, Fusion Eng. Des. 161 (2020), 111919.
[54] P.A. Di Maio, et al., Hydraulic assessment of an upgraded pipework arrangement for the DEMO divertor plasma facing components cooling circuit, Fusion Eng. Des. 168 (2021), 112368.
[55] A. Tincani, et al., Hydraulic characterization of the full scale mock-up of the DEMO divertor outer vertical target, Energy 14 (2021) 8086.
[56] J.H. You, et al., European DEMO divertor target: operational requirements and material-design interface, Nucl. Mater. Energy 9 (2016) 171–176.
[57] S.A. Fabritsiev, et al., Low-temperature radiation embrittlement of copper alloys, J. Nucl. Mater. 233-237 (1996) 513–518.
[58] G.M. Kalinin, et al., The effect of irradiation on tensile properties and fracture toughness of CuCrZr and CuCrNiSi alloys, J. Nucl. Mater. 417 (2011) 908–911.
[59] S. Tähtinen, et al., Effect of neutron irradiation on fracture toughness behavior of copper alloys, J. Nucl. Mater. 258-263 (1998) 1010–1014.
[60] J.H. You, et al., Structural lifetime assessment for the DEMO divertor targets: design-by-analysis approach and outstanding issues, Fusion Eng. Des. 164 (2021), 112203.
[61] J.H. You, Copper matrix composites as heat sink materials for water-cooled divertor target, Nucl. Mater. Ener. 5 (2015) 7–18.
[62] J.H. You, A review on two previous divertor target concepts for DEMO: mutual impact between structural design requirements and materials performance, Nucl. Fusion 55 (2015), 113026.
[63] E. Gaganidze, et al., Assessment of neutron irradiation effects on RAFM steels, Fusion Eng. Des. 88 (2013) 118–128.
[64] G. Mazzone, et al., Choice of a low operating temperature for the DEMO EUROFER97 divertor cassette, Fusion Eng. Des. 124 (2017) 655–658.
[65] DEMO design criteria for in-vessel components (DDC-IC) Part-B: design criteria and analysis procedures, first draft (2020).
[66] B. van der Schaaf, et al., The development of EUROFER reduced activation steel, Fusion Eng. Des. 69 (2003) 197–203.
[67] S. Noce, et al., Neutronics analysis and activation calculation for Tungsten used in the DEMO divertor targets: a comparative study between the effects of WCLL and HCPB blanket, different W compositions and Chromium, Fusion Eng. Des. 169 (2021), 112428.
[68] S. Noce, et al., Nuclear analyses for the design of the ITER-like plasma facing components vertical targets of the DEMO divertor, Fusion Eng. Des. 155 (2020), 111730.
[69] S.A. Fabritsiev, et al., Effect of high doses of neutron irradiation on physico-mechanical properties of copper alloys for ITER applications, Fusion Eng. Des. 73 (2005) 19–34.
[70] S.A. Fabritsiev, et al., Neutron irradiation induced high temperature embrittlement of pure copper, Plasma Devices Oper. 5 (1997) 133–141.
[71] RCC-MRx 2018 AFCEN edition, Design and construction rules for mechanical components of nuclear installation.
[72] ITER structural design criteria for in-vessel components, G 74 MA 8 01-05-28 W0.2.
[73] P. Frosi, et al., Structural design of DEMO Divertor Cassette Body: FEM analysis and introductive application of RCC-MRx design rules, Fusion Eng. Des. 109-111 (2016) 47–51.

[74] P. Frosi, et al., Structural analysis of DEMO divertor cassette body and design study based on RCC-MRx, Fusion Eng. Des. 124 (2017) 628–632.
[75] P. Frosi, et al., Further improvements in the structural analysis of DEMO Divertor Cassette body and design assessment according to RCC-MRx, Fusion Eng. Des. 138 (2019) 119–124.
[76] P. Frosi et al., DEMO Divertor shielding components assessment according to RCC-MRx, Fusion Eng. Des., submitted.
[77] M. Fursdon, et al., An elastic analysis procedure for assessing divertor monoblock designs, Fusion Eng. Des. 135 (2018) 154–164.
[78] M. Li, et al., Fracture mechanical analysis of tungsten armor failure of a water-cooled divertor target, Fusion Eng. Des. 89 (2014) 2716–2725.
[79] M. Li, et al., Low cycle fatigue behavior of ITER-like divertor target under DEMO-relevant operation conditions, Fusion Eng. Des. 90 (2015) 88–96.
[80] M. Li, et al., Structural impact of creep in tungsten monoblock divertor target at 20 MW/m^2, Nucl. Mater. Ener. 14 (2018) 1–7.
[81] M. Fursdon, et al., Enhancements in the structural integrity assessment of plasma facing components, Fusion Eng. Des. 146 B (2019) 1591–1595.
[82] M. Fursdon, et al., Towards reliable design-by-analysis for divertor plasma facing components - guidelines for inelastic assessment (part I: unirradiated), Fusion Eng. Des. 147 (2019), 111234.
[83] M. Fursdon, et al., Towards reliable design-by-analysis for divertor plasma facing components - Guidelines for inelastic assessment (part II: irradiated), Fusion Eng. Des. 160 (2020), 111831.
[84] F. Crescenzi, et al., FEM and thermal fatigue testing comparison of ITER-like divertor PFUs mock-ups for DEMO, Fusion Eng. Des. 136 (2018) 558–562.
[85] F. Domptail, et al., The design and optimization of a monoblock divertor target for DEMO using thermal break interlayer, Fusion Eng. Des. 154 (2020), 111497.
[86] G. Di Mambro et al., Mechanical impact of electromagnetic transients on the European DEMO divertor. Part 1: vertical Displacement Event, Fusion Eng. Des., accepted.
[87] R. Coppola, et al., Neutron diffraction measurement of residual stresses in an ITER like tungsten-monoblock type plasma-facing component, Fusion Eng. Des. 146 (2019) 701–704.
[88] V. Barabash, et al., Specification of CuCrZr alloy properties after various thermo-mechanical treatments and design allowables including neutron irradiation effects, J. Nucl. Mater. 417 (2011) 904–907.
[89] M. Merola, et al., Engineering challenges and development of the ITER blanket system and divertor, Fusion Eng. Des. 96–97 (2015) 34–41.
[90] R.A. Pitts, et al., A full tungsten divertor for ITER: physics issues and design status, J. Nucl. Mater. 438 (2013) S48–S56.
[91] A.R. Raffray, et al., Critical heat flux analysis and R&D for the design of the ITER divertor, Fusion Eng. Des. 45 (1999) 377–407.
[92] A.R. Raffray, et al., High heat flux components - Readiness to proceed from near term fusion systems to power plants, Fusion Eng. Des. 85 (2010) 93–108.
[93] J. Öijerholm, et al., Assessment of flow-accelerated corrosion rate of copper alloy cooling tube for application in fusion reactors, in: Proceedings of the International Conference Water Chemistry in Nuclear Reactor Systems, 2021.
[94] C. Harrington et al., Target cooling pipe corrosion-erosion protection technology, Eurofusion report 2NECDY (2020).
[95] J.H. You, et al., European divertor target concepts for DEMO: design rationales and high heat flux performance, Nucl. Mater. Energy 16 (2018) 1–11.
[96] F. Crescenzi, et al., Design optimization of the DEMO ITER-like water-cooled divertor, Fusion Eng. Des. 98-99 (2015) 1263–1266.
[97] E. Visca, et al., Manufacturing and testing of ITER-like divertor plasma facing mock-ups for DEMO, Fusion Eng. Des. 136 (2018) 1593–1596.
[98] T. Barrett, et al., Progress in the engineering design and assessment of the European DEMO first wall and divertor plasma facing components, Fusion Eng. Des. 109-111 (2016) 917–924.
[99] M. Fursdon, et al., The development and testing of the thermal-break divertor monoblock target design delivering 20MW/m2 heat load capability, Phys. Scr. T170 (2017), 014042 (7pp).
[100] A. Lukenskas, et al., High heat flux test results for a thermal break DEMO divertor target and subsequent design and manufacture development, Fusion Eng. Des. 146 (2019) 1657–1660.
[101] A.v. Müller, et al., Melt infiltrated W-Cu composites as advanced heat sink materials for plasma facing components of future nuclear fusion devices, Fusion Eng. Des. 124 (2017) 455–459.
[102] A.v. Müller, et al., Application of tungsten-copper composite heat sink materials to plasma-facing component mock-ups, Phys. Scr. T171 (2020), 014015 (8pp).
[103] E. Tejado, et al., Evolution of mechanical performance with temperature of W/Cu and W/CuCrZr composites for fusion heat sink applications, Mater. Sci. Eng. A 712 (2018) 738–746.
[104] E. Tejado, et al., The thermo-mechanical behaviour of W-Cu metal matrix composites for fusion heat sink applications: the influence of the Cu content, J. Nucl. Mater. 498 (2018) 468–475.
[105] J.H. You, et al., Thermal and mechanical properties of infiltrated W/CuCrZr composite materials for functionally graded heat sink application, J. Nucl. Mater. 438 (2013) 1–6.
[106] M. Richou, et al., Realization of high heat flux tungsten monoblock type target with graded interlayer for application to DEMO divertor, Phys. Scr. T170 (2017), 014022 (7pp).
[107] M. Richou, et al., Status on the W monoblock type high heat flux target with graded interlayer for application to DEMO divertor, Fusion Eng. Des. 124 (2017) 338–343.
[108] M. Richou, et al., Performance assessment of high heat flux W monoblock type target using thin graded and copper interlayers for application to DEMO divertor, Fusion Eng. Des. 146 (2019) 858–861.
[109] M. Richou, et al., Performance assessment of thick W/Cu graded interlayer for DEMO divertor target, Fusion Eng. Des. 157 (2020), 111610.
[110] F. Gallay, et al., Quantitative thermal imperfection definition using non-destructive infrared thermography on an advanced DEMO divertor concept, Phys. Scr. T170 (2017), 014015 (5pp).
[111] G. Dose, et al., Ultrasonic analysis of tungsten monoblock divertor mock-ups after high heat flux test, Fusion Eng. Des. 146 (2019) 870–873.
[112] S. Roccella, et al., Ultrasonic test results before and after high heat flux testing on W-monoblock mock-ups of EU-DEMO vertical target, Fusion Eng. Des. 160 (2020), 111886.
[113] Y. Addab, et al., Typology of defects in DEMO divertor target mockups, Phys. Scr. 96 (2021), 124065.
[114] T. Minniti, et al., Structural integrity of DEMO divertor target assessed by neutron tomography, Fusion Eng. Des. 169 (2021), 112661.
[115] H. Greuner, et al., Progress in high heat flux testing of European DEMO divertor mock-ups, Fusion Eng. Des. 146 (2019) 216–219.
[116] H. Greuner, et al., Assessment of the high heat flux performance of European DEMO divertor mock-ups, Phys. Scr. T171 (2020), 014003 (7pp).